

# Lawrence Berkeley National Laboratory

## Lawrence Berkeley National Laboratory

### **Title**

PHOTOELECTRON PHOTOION MOLECULAR BEAM SPECTROSCOPY

### **Permalink**

<https://escholarship.org/uc/item/8m17b541>

### **Author**

Trevor, Dennis J.

### **Publication Date**

1980-12-01

Peer reviewed

This book was prepared as an account of work sponsored by an agency of the United States Government. Neither the United States Government nor any agency thereof, nor any of their employees, makes any warranty, express or implied, or assumes any legal liability or responsibility for the accuracy, completeness, or usefulness of any information, apparatus, product, or process disclosed, or represents that its use would not infringe privately owned rights. References herein to any specific commercial product, process, or service by trade name, trademark, manufacturer, or otherwise, does not necessarily constitute or imply its endorsement, recommendation, or favoring by the United States Government or any agency thereof. The views and opinions of authors expressed herein do not necessarily state or reflect those of the United States Government or any agency thereof.

## Table of Contents

	<u>Page</u>
Abstract . . . . .	vii
I. Introduction . . . . .	1
References . . . . .	6
II. Photoionization Mass Spectroscopy of Rare Gas Dimers . . . . .	7
A. Introduction . . . . .	7
B. Experimental . . . . .	9
C. Results. . . . .	12
D. Discussion . . . . .	15
1. Rare Gas Dimer Ionic States. . . . .	15
2. Excited States of Rare Gas van der Waals Dimers. . . . .	19
3. The Ionization Process . . . . .	25
4. Rare Gas van der Waals Dimer Ionization. . . . .	30
5. (He) <sub>n</sub> Discussion . . . . .	37
E. Conclusions and Summary. . . . .	39
References . . . . .	40
Tables . . . . .	44
Figure Captions. . . . .	50
Figures. . . . .	53
III. Photoionization Mass Spectra of a Few Molecules and Clusters. . . . .	67
A. Introduction . . . . .	67
B. Photoionization Mass Spectroscopy of NH <sub>3</sub> and O <sub>3</sub> . . . . .	68
C. Proton Affinity of H <sub>2</sub> O . . . . .	70.
1. Proton Affinity of H <sub>2</sub> O . . . . .	70
2. Results and Discussion . . . . .	72
D. Photoion Yield of N <sup>+</sup> from N <sub>2</sub> , C <sup>+</sup> from CO and H <sup>+</sup> from H <sub>2</sub> . . . . .	76
1. Introduction . . . . .	76
2. Experimental . . . . .	78
3. Results and Discussion . . . . .	78

*EB*

Table of Contents (continued)

	<u>Page</u>
E. Photoion Yield of $N_3^+$ from $(N_2)_2$ and $C_2O^+$ from $(CO)_2$ . . .	84
References . . . . .	87
Tables . . . . .	92
Figure Captions. . . . .	95
Figures. . . . .	97
IV. Photoelectron Spectroscopy and Feasibility of Photoelectron-Photoion Coincidence Measurements . . . . .	108
A. Introduction . . . . .	108
B. Ultraviolet Photoelectron Spectrometers. . . . .	110
1. State-of-the-Art Instrumentation . . . . .	110
2. New Very High Resolution Photoelectron Spectrometer. . . . .	113
C. Coincidence Measurements . . . . .	113
References . . . . .	116
Figure Captions. . . . .	117
Figures. . . . .	118
V. Proposed Design for a VUV Gas Phase Experimental Station at SSRL . . . . .	120
A. Introduction . . . . .	120
B. Design Objectives. . . . .	120
C. Design Approach and Background . . . . .	121
D. Design Description . . . . .	131
1. Optical System . . . . .	133
2. Differential Pumping System. . . . .	135
3. Installation . . . . .	138
4. The Future . . . . .	139

Table of Contents (continued)

	<u>Page</u>
References . . . . .	140
Tables . . . . .	141
Figure Captions. . . . .	145
Figures. . . . .	146
Acknowledgments. . . . .	149

PHOTOELECTRON PHOTOION MOLECULAR BEAM SPECTROSCOPY

Dennis J. Trevor

Materials and Molecular Research Division  
Lawrence Berkeley Laboratory

and

Department of Chemistry  
University of California  
Berkeley, California 94720

ABSTRACT

The use of supersonic molecular beams in photoionization mass spectroscopy and photoelectron spectroscopy to assist in the understanding of photoexcitation in the vacuum ultraviolet is described. Rotational relaxation and condensation due to supersonic expansion were shown to offer new possibilities for molecular photoionization studies. Molecular beam photoionization mass spectroscopy has been extended above 21 eV photon energy by the use of Stanford Synchrotron Radiation Laboratory (SSRL) facilities. Design considerations are discussed that have advanced the state-of-the-art in high resolution VUV photoelectron spectroscopy. To extend gas-phase studies to 160 eV photon energy, a windowless VUV-XUV beam line design is proposed.

Detailed considerations of the autoionization mechanisms and symmetry of the excited states of  $\text{Ne}_2$  have lead to the assignment of structure observed in its photoionization efficiency, and demonstrated the importance of Rydberg states with  $B^2\Pi_u$  core. The lower bound to the dissociation energy of  $\text{Ne}_2^+$  was determined to be  $1.36 \pm 0.05$  eV ( $31.3 \pm 1.2$  kcal/mole) and comparisons made with the heavier rare-gas systems indicated the importance of spin-orbit interactions. A search for the possible existence of  $\text{He}_2$  was carried out which lead to inconclusive results. However, the  $\text{He}_2^+$  photoion yield of cluster(s) present in the beam was measured.

Rotational relaxation in supersonic molecular beams enhanced the direct ionization structure in the photoionization efficiencies of  $\text{NH}_3$ ,  $\text{O}_3$ , and  $\text{H}_2\text{O}$ . The measured adiabatic ionization potentials and ionic vibrational frequencies are:  $\text{NH}_3$ , IP =  $10.176 \pm 0.008$  eV,  $\nu_2 = 950 \pm 32$   $\text{cm}^{-1}$ ;  $\text{O}_3$ , IP =  $12.523 \pm 0.008$  eV,  $\nu_2 = 650 \pm 40$   $\text{cm}^{-1}$ ;  $\text{H}_2\text{O}$ , IP =  $12.601 \pm 0.016$  eV,  $\nu_1 = 3300 \pm 260$   $\text{cm}^{-1}$ ,  $\nu_2 = 1520 \pm 260$   $\text{cm}^{-1}$ . In addition, enhancements in the autoionization structure near threshold was observed in  $\text{NH}_3$  and  $\text{H}_2\text{O}$  experiments. This elimination of rotational broadening was also demonstrated to improve the obtainable resolution in molecular ultraviolet photoelectron spectroscopy. The HeI photoelectron spectra of the  $\text{O}_2^+ X^2\Pi_g$  state is presented. Excess condensation in a supersonic molecular beam of  $\text{H}_2\text{O}$  enabled the measurements of the threshold for  $(\text{H}_2\text{O})_2^+$  production, yielding  $11.21 \pm 0.09$  eV. The appearance potential of  $\text{H}_3\text{O}^+$ ,  $11.73 \pm 0.03$  eV, gave a proton affinity for  $\text{H}_2\text{O}$  of  $7.18 \pm 0.08$  eV ( $165.8 \pm 1.8$  kcal/mole).

The interesting results of photoionization mass spectroscopy at photon energies between 18 eV and 35 eV on  $N_2$ , CO,  $H_2$ ,  $(CO)_2$ , and  $(N_2)_2$  are reported. Autoionization structure resolved in the  $N^+$  photoion yield from  $N_2$  was shown to support a homogeneous mechanism for the dissociation of the  $C^2\Sigma_u^+$  state of  $N_2^+$ . An enhancement in the  $H^+$  photoion yield from  $H_2$  was observed at 30 eV.

CHAPTER I  
INTRODUCTION

Spectroscopy is the primary source of information leading to our current understanding of the quantized energy levels of atoms and molecules. The easy tunability of a photon source and the photon's quantized energy and angular momentum add significantly to its versatility as a probe. A variety of experimental methods have been developed to measure the cross-sections for transitions between the initial and final states, throughout the accessible electromagnetic spectrum. Spectroscopy in the visible and ultraviolet range has led to our present understanding of electronic interactions (chemical bonding) in molecular systems. At higher photon energies (i.e., the vacuum ultraviolet (VUV)), the final states which are attainable lie in a continuum with respect to ionization. Spectroscopy in this region reveals the structure of the ionic atomic and molecular states.

In absorption of a photon of energy,  $(h\nu)$ , the initial state of energy  $E''$  is driven to a final state of energy  $E_f$ , according to

$$h\nu = E_f - E'' .$$

If ionization occurs, the final state energy is partitioned between the kinetic energy of the electron,  $KE$ , and potential energy of the ionic state,  $E'$ , as follows:

$$E_f = KE + E' .$$



The absorption is therefore continuous above the threshold ( $KE = 0$ ) for this process, called the adiabatic ionization potential (AIP), given by

$$h\nu = E' - E'' = \text{AIP} .$$

With even higher photon energies, higher lying ionic states can be populated. Each of these states will also have an adiabatic ionization potential. Generalizing, the energy balance equation, where  $E_j'$  and  $KE_j$  are the energies of a particular ionic state and the resulting electron, respectively, we have:

$$h\nu = (E_j' - E'') + KE_j .$$

The quantity  $E_j' - E''$  is referred to as the binding energy.

Embedded in the ionization continuum are "quasi-bound" neutral states. These states can have pronounced effects on the ionization cross-section, depending upon their coupling with the neighboring continuum.<sup>1</sup>

Absorption spectroscopy measures the total absorption cross-section as a function of photon energy. This technique has provided the most accurate ionization potentials and structural information on atoms and molecules.<sup>2</sup> These ionization potentials are obtained by determination of a Rydberg series converging to the ionization energy. The actual onset of the ionization continuum absorption is disguised by the increasing density of Rydberg states.<sup>3</sup> In addition, in many systems the Rydberg states themselves are severely broadened or not assignable.

High resolution photoionization mass spectroscopy measures the ion production as a function of photon energy. This first order differential technique yields the partial cross-section (with respect to ion mass). It is sensitive to the onset of ionization and applicable to all systems. However, the observed thresholds are usually broadened by unresolved rotational structure and collisional ionization.<sup>4,5</sup> If an intense, well collimated supersonic molecular beam is employed as the source in a photoionization mass spectrometer, these problems are eliminated,<sup>6</sup> due to the extensive cooling of the translational and rotational degrees of freedom that occur in such an expansion.<sup>7</sup> In addition, these molecular beams are excellent sources of "exotic" species such as van der Waals clusters.<sup>8,9</sup> Experiments of this type are reported in Chapters II and III. Even with these improvements, the ionization potentials are not as accurate as those obtainable by absorption spectroscopy. The reason is photon resolution. High resolution absorption spectra can be recorded photographically using spectrographs with resolution far exceeding that available from monochromators in the VUV wavelength region.<sup>10</sup> In addition, existing photoionization mass spectrometers are only single channel (one photon energy recorded at a time) devices. With the advent of synchrotron radiation laboratories, more intense sources of well collimated photons are available, which will certainly lead to the development of higher resolution monochromators.

Photoionization mass spectroscopy is not sensitive to higher ionization potentials, for the same reason, that absorption spectroscopy is not sensitive to the first and higher ionization potentials.<sup>3</sup>

However, the kinetic energy of the electron produced in photoionization is characteristic of the final state of the ion. Therefore, techniques that measure the kinetic energy of the electron are sensitive to higher ionization potentials. The most popular of these methods is called photoelectron (PE) spectroscopy.<sup>11</sup> In these experiments the photon energy is fixed and the photoelectron intensity is measured as a function of kinetic energy. Photoelectron spectra obtained in this fashion display the relative cross-sections of the different quantum states of the ion produced by photoionization. Typical PE spectra yield the energies of the electronic states of the ion; and, for many small molecular systems the resolution has been sufficient to obtain vibrational frequencies. The resolution of PE spectroscopy of molecular systems is limited by the rotational state population and Doppler broadening due to the thermal motion of the sample.<sup>11</sup> As in PI spectroscopy, employing supersonic molecular beam technology eliminates these difficulties.<sup>12</sup> In Chapter IV work in this area will be discussed.

Both PI and PE spectroscopy, are single parameter differential cross-section measurement techniques. In PI spectroscopy a question frequently asked is: "What fraction of the energy is left as internal excitation (electronic, vibrational) in the ion?" Similarly asked in PE spectroscopy: "What happens to the internal energy of the ion? Does the ion fragment or radiate?" To answer these questions at least two parameters must be measured in coincidence. Several coincidence methods have appeared in the past decade.<sup>13</sup> One technique, that of detecting the energy resolved photoelectron in coincidence with the kinetic energy and mass resolved photoion, was pursued as part of this

work. Although we have as yet been unsuccessful, the design problems that need to be solved are discussed in Chapter IV.

Major developments in VUV research on gas phase systems, have been assisted by the availability of intense sources of synchrotron radiation. One of these sources, the Stanford Positron Electron Accelerator Ring (SPEAR), has been used to carry out a substantial amount of the research I have reported here, even though the SPEAR facilities were not designed for gas-phase studies.<sup>14</sup> In order to increase the usefulness of this intense source of VUV radiation for gas-phase research, a new experimental station has been proposed. I have used the last chapter to describe what I believe to be the best design, as well as to give some background information on the challenging field of VUV and XUV optics.

References: Chapter I

1. V. Fano and J. W. Cooper, Rev. of Modern Phys. 40, 441 (1968).
2. G. Herzberg, "Molecular Spectra and Molecular Structure," vol. I, II and III. Van Nostrand Reinhold Co. (1950).
3. J. Berkowitz, "Photoabsorption, Photoionization, and Photoelectron Spectroscopy," Academic Press (1979).
4. P. M. Guyon and J. Berkowitz, J. Chem. Phys. 54, 1814 (1971).
5. W. A. Chupka, J. Chem. Phys. 54, 1936 (1971).
6. C. Y. Ng, B. H. Mahan and Y. T. Lee, J. Chem. Phys. 65, 1965 (1976).
7. H. Pauly and J. P. Toennies, "Neutral-Neutral Interactions; Beam Experiments at Thermal Energies" in Methods of Experimental Physics Vol. 7A, Academic Press (1968).
8. C. Y. Ng, D. J. Trevor, B. H. Mahan and Y. T. Lee, J. Chem. Phys. 65, 1965 (1976).
9. C. Y. Ng, D. J. Trevor, P. W. Tiedemann, S. T. Ceyer, P. L. Kronebusch, B. H. Mahan, and Y. T. Lee, J. Chem. Phys. 67, 4235 (1977).
10. J. A. R. Samson, "Techniques of Vacuum Ultraviolet Spectroscopy," John Wiley and Sons, Inc. (1967).
11. J. W. Rabalais, "Principles of Ultraviolet Photoelectron Spectroscopy," John Wiley and Sons, Inc. (1977).
12. P. M. Dehmer and J. L. Dehmer, J. Chem. Phys. 70, 4574 (1979).
13. J. H. D. Eland, Int. J. Mass Spectrum. Ion Phys. 8, 143 (1972).
14. "Synchrotron Radiation Research and the Stanford Synchrotron Radiation Project" ed. K. O. Hodgson, H. Winick and G. Chu, SRRP 76/100, Stanford University (1976).

## CHAPTER II

## PHOTOIONIZATION MASS SPECTROSCOPY OF RARE GAS DIMERS

A. Introduction

The electronic structure of the rare-gas dimer ground, Rydberg, and ionic states have been the subject of numerous theoretical and experimental studies in recent years, owing their popularity to the key role they play in the kinetics of rare gas helide and excimer laser systems. Lower bounds to the dissociation energies of the rare gas molecular ions ( $Rg_2^+$ ) have been measured by electron impact,<sup>1</sup> photon-induced associative ionization,<sup>2</sup> electron recombination fluorescence line-width measurements<sup>3</sup> and by photoionization mass spectrometry.<sup>4,5</sup> Semi-empirical<sup>6</sup> and ab initio<sup>7</sup> electronic structure calculations have been performed with a variety of basic sets and formalisms on the ionic states, ground states, and excited Rydberg states. The study reported here is based on previous work in this laboratory on  $Ar_2$ ,  $Kr_2$ <sup>5</sup> and  $Xe_2$ ,<sup>4</sup> using a supersonic expansion as a source of excess van der Waals clusters in a photoionization mass spectrometer.

The previous work demonstrated the usefulness of applying molecular beam technology to photoionization mass spectroscopy. Lower bounds were obtained for the bond strengths of the rare-gas molecular ions  $Ar_2^+$ ,  $Kr_2^+$  and  $Xe_2^+$ . In order to study  $Ne_2$  and the possible existence of  $He$  dimer, whose ionization potentials exceed the energy range of intense laboratory ultraviolet sources, a higher-energy continuum light source is needed. Synchrotron radiation fulfills these needs.

Previous results on the rare gas systems showed a degree of simplification in their spectra in going from  $\text{Xe}_2$  to  $\text{Ar}_2$ .<sup>5</sup> An attempt to assign the intense features in the simplest system studied,  $\text{Ar}_2$ , left several possibilities for each. These features were obviously groups of states located near the atomic resonance lines. With the laboratory apparatus used the resolution was not sufficient to separate the overlapping or closely-spaced states. The extension to  $\text{Ne}_2$  was thought to have the following helpful advantages: with its larger  $D_0$  and smaller mass the density of states near threshold would be smaller, and its smaller spin-orbit splitting might sufficiently reduce the  $\Omega = +1$  excitations, simplifying the analysis.

By far the most valuable experimental works used in the analysis of these rare-gas spectra were the high resolution absorption spectra by Y. Tanaka and K. Yoshino<sup>8-11</sup> and others.<sup>12-14</sup> The most valuable theoretical treatment was the estimates made by Mulliken in 1970 of the first few Rydberg states in  $\text{Xe}_2$ .<sup>6</sup>

The existence of the simplest van der Waals dimer,  $\text{He}_2$ , has been the subject of much investigation. The potential derived from elastic scattering measurements is so shallow ( $10.6 \text{ K}$ )<sup>15</sup> that no bound states are predicted for this molecule. Theoretical calculations have supported this prediction; however, a 1.4% decrease in well depth is sufficient for the stability of a bound state of zero angular momentum.<sup>16,17</sup> Conventional electron bombardment ionization mass spectroscopy of supersonic molecular beams of He has yet to yield unambiguous results, since the larger clusters dissociatively ionize to  $\text{He}_2^+$ .<sup>18,19</sup> In addition high resolution VUV absorption studies in a cooled gas cell failed to find

evidence of a bound state.<sup>20</sup> The investigation of the photoionization yield from He beams was pursued, in hope that, the mild photoionization process would reduce the dissociative ionization which disturbed the earlier reported searches for He<sub>2</sub>, based on conventional electron impact mass spectrometry.<sup>18,19</sup> However, these attempts were unsuccessful in establishing definitely whether or not He<sub>2</sub> is stable.

## B. Experimental

The apparatus developed for these experiments consisted of a supersonic differentially pumped molecular beam source, a quadrupole mass spectrometer, an ultrathin (1500 Å) Aluminum/Silicon window, and a photon intensity monitor. A schematic of the apparatus is shown in Fig. 1.

The experiments were performed at Stanford Synchrotron Radiation Laboratory (SSRL) on Beam line I-2 (8°). This branch line has been described in detail elsewhere.<sup>21</sup> Briefly it consists of a system of 3 mirrors arranged to focus the radiation from the stored electron beam onto the entrance slit of a 1 m Seya-Namioka monochromator with a 1200 lines/mm grating blazed at 540 Å and an additional mirror to refocus the monochromator output beam into the experimental chamber. The photon intensity available for these experiments was approximately  $4 \times 10^7$  photons (sec)<sup>-1</sup> (mA)<sup>-1</sup> (Å)<sup>-1</sup> at 584 Å as measured with a calibrated NBS photodiode, with a photon wavelength resolution of 2.5 Å FWHM, and a stored electron beam current of 42 mA under dedicated operation. The measured photon intensity as a function of wavelength after passing through a 1500 Å thick Al/Si window is shown in Fig. 2. This Aluminum window was needed to protect the ultrahigh vacuum of the beam line from



possible contamination by the background gas in the ionization chamber. This window isolation system was also equipped with an interlocked fast-closing gate valve to protect against vacuum failure, and has previously been described in detail.<sup>22</sup> The monochromatic photon beam was focused to a image approximately 1 mm x 3 mm in the interaction region.

The supersonic molecular beam was produced by expanding gas through a 20  $\mu\text{m}$ -diameter nozzle. The nozzle assembly was incorporated into the inner dewar of a modified liquid He cryopump. The sample gas passed through two cryotrap before reaching the nozzle. When Helium beams were used the first trap was kept at liquid nitrogen temperature and the second at liquid helium temperature. When neon gas was used both traps were kept at liquid nitrogen. The temperature of the nozzle was monitored by a thermocouple and/or a carbon resistance thermometer. The expanded gas was collimated by a 660  $\mu\text{m}$ -diameter skimmer located 8 mm downstream from the nozzle, separating the beam source chamber from the interaction region. The beam source chamber was pumped by a 500 l/sec turbomolecular pump.

The collimated molecular beam intersected the focused monochromatic photon beam 27 mm from the nozzle in the center of the extraction lenses for the quadrupole mass spectrometer. The interaction region was pumped by a second 500 l/sec turbomolecular pump. After passing through the interaction region most of the beam molecules are pumped away by a 270 l/sec turbomolecular pump connected to the beam catcher. The interaction chamber ion gauge reading (uncorrected), with a 2000 torr Ne beam at 77 K was  $1.5 \times 10^{-6}$  torr. This low background pressure was necessary

in order to avoid interfering chemi-ionization and collisional ionization processes. The estimated number density of the beam in the interaction region was  $10^{11} - 10^{12} \text{ cm}^{-3}$ .

The ions created in the center of the interaction region were extracted by a  $200 \text{ V cm}^{-1}$  field. A pair of cylinder lenses were used to focus the ions at the entrance of the quadrupole mass filter (Extranuclear Laboratories) located in a separate chamber differentially pumped by a 220 l/sec noble ion pump. In addition to the conventional resolution control, the ion kinetic energy along the quadrupole field was adjusted in order to obtain the maximum transmission for the desired resolution. The mass selected ions were accelerated to 3.5 keV and detected by a Spiraltron electron multiplier and pulse counting electronics.

After intersecting the molecular beam the photon beam impinged upon either a calibrated NBS  $\text{Al}_2\text{O}_3$  photodiode or a sodium salicylate coated quartz disc whose fluorescence was monitored by an RCA 8850 Photo multiplier Tube. The fluorescence efficiency of sodium salicylate has been shown to be a constant over the wavelength regions of interest,<sup>23</sup> in contrast to the photoyield of the the  $\text{Al}_2\text{O}_3$  diode. Thus, the sodium salicylate monitor was chosen for the majority of these measurements. The output current of the RCA 8850 Photomultiplier tube was amplified by a Keithly 417 picoammeter and processed by a 10 kHz voltage to frequency converter. This frequency was then registered concurrently with the ion signal.

The monochromator wavelength stepping motor, ion scaler and photon scaler were microprocessor controlled. A photoionization efficiency spectrum was measured by recording simultaneously the ion and photon signals as a function of decreasing wavelength. The photon signal, after a constant correction for scattered light and photomultiplier dark current, was used to calculate the photoionization efficiency. As shown in Fig. 2 the photon intensity peaked at 550 Å and then decreased to only a few percent of the peak intensity by 350 Å. This was due to a near normal incidence reflection on one of the focusing mirrors in the 8° beam line. Because of it, second-order light interference was a serious problem only for wavelengths above 650 Å. The wavelength scales for these spectra were obtained by measuring the ionization thresholds for Ne and He. Due both to the beam-line optics and to variations in the electron beam position the accuracy of the wavelength scale could only be determined to within the half width at half maximum band pass of the monochromator (0.4 Å). However, the relative wavelength scale was found to be reproducible to better than 0.1 Å.

### C. Results

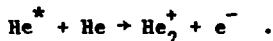
The photoionization yield of  $\text{Ne}_2^+$  recorded at a resolution of 2.5Å (FWHM) is shown in Fig. 3.  $\text{Ne}_2$  was prepared by expanding Ne gas at 77 K and 2000 torr through a 20 μm-diameter nozzle. The threshold for production of  $\text{Ne}_2^+$  was taken to be the point at which the signal rose above the background. The sensitivity of these signal measurements at threshold was 1% of the signal at 570 Å. Due to the cooling of internal modes in the supersonic expansion no corrections to the measured

threshold were deemed necessary. The observed ionization potential of  $\text{Ne}_2$  was found to be  $20.21 \pm 0.05$  eV ( $613.6 \pm 1.5$  Å). This threshold energy is an upper bound to the adiabatic ionization potential of  $\text{Ne}_2$ . Combining this number with the ionization potential of Ne ( $21.565$  eV)<sup>24</sup> and the  $\text{Ne}_2$  bond strength ( $0.004$  eV)<sup>25</sup> we obtain an lower bound to the dissociation energy of  $\text{Ne}_2^+$  of  $1.36 \pm 0.05$  eV. This value is in excellent agreement with previous spectral line shape studies of Connor and Biondi.<sup>3</sup> The reported electron impact appearance potential measurement<sup>28</sup> is  $0.69 \pm 0.2$  eV. This technique suffers from poor energy resolution and poor threshold sensitivity. The dissociation energy derived from interpretation of ion molecule scattering data ranges anywhere from  $0.33$  eV to  $0.71$  eV.<sup>27</sup> This method is limited by low energy ion source technology and difficulty in data interpretation due to the complication and possible interference of more than one potential energy surface.

The photoion yield signal rises slowly from threshold due to the very small (Franck-Condon) overlap between the weakly bound long-range potential of the ground state and the more strongly bound ground ionic state. Several broad, unresolved peaks are present in this spectrum, as was the case for the heavier rare gas systems previously studied.<sup>4,5</sup> A higher resolution scan ( $0.8$  Å FWHM) over this same wavelength region is shown in Fig. 4. This scan shows the majority of the above peaks, with widths near instrumental resolution.

The photoionization yield of  $\text{Ne}_2^+$  from  $545$  Å to  $490$  Å at a photon band pass of  $0.8$  Å FWHM is shown in Fig. 5. This spectrum was obtained from an expansion of Ne gas at  $4.2$  K and  $700$  torr through a  $20$   $\mu\text{m}$  nozzle. The spectrum is dominated by a series of sharp autoionization resonances.

In fact, the direct ionization below the atomic ionization potential was less than 1% of the peak intensity. This very small direct ionization cross section made it impossible to prove whether the  $\text{He}_2^+$  originated from the supposed molecule  $\text{He}_2$  or from dissociative ionization of larger clusters. A careful search for  $\text{He}_3^+$  ion at the peak of the autoionization resonances and above the atomic ionization potential resulted in no signal above the background of 0.1 counts/sec. By comparison, the  $\text{He}_2^+$  signal was 4 counts  $\text{sec}^{-1}$  at the peak of the autoionization resonances, and the  $\text{He}^+$  signal was typically 3000 counts  $\text{sec}^{-1}$  beyond the threshold. The background pressure in the ionization region was estimated to be  $6 \times 10^{-7}$  torr (corrected for the ionization efficiency of He). This low background pressure in the interaction region excludes the possibility of the observed  $\text{He}_2^+$  being produced solely by chemi-ionization, that is



Measurements made with similar beam intensities and with higher main-chamber background pressures but at 77 K (where helium clusters are not expected to be present) showed that at most only 5% of the observed signal could be due to this type of process. Therefore the majority of the observed  $\text{He}_2^+$  signal must come from clusters formed in the He expansion at 4.2 K.

## D. Discussion

### 1. Rare Gas Dimer Ionic States

The rare gas van der Waals molecules ( $\text{Ne}_2$  and larger) can be described by a linear combination of atomic orbitals-molecular orbital (LCAO) single-determinant configuration of

$$\dots (\sigma_g ns)^2 (\sigma_u ns)^2 (\sigma_g np)^2 (\pi_u np)^4 (\pi_g np)^4 (\sigma_u np)^2$$

where  $n = 2, 3, 4$  and  $5$  for  $\text{Ne}$ ,  $\text{Ar}$ ,  $\text{Kr}$  and  $\text{Xe}$ , respectively.

The ground states of the rare-gas dimers have  ${}^1\Sigma_g^+$  ( $O_g^+$ ) symmetry and are overall repulsive with only long range van der Waals minima of 4 meV, 12 meV, 17 meV, and 24 meV at 3.1 Å, 3.76 Å, 4.00 Å, and 4.36 Å for  $\text{Ne}_2$ ,  $\text{Ar}_2$ ,  $\text{Kr}_2$  and  $\text{Xe}_2$ , respectively.<sup>25,28</sup> The four lowest ionic states LCAO configurations, neglecting spin-orbit effects are:

$$\dots (\sigma_g np)^2 (\pi_u np)^4 (\pi_g np)^4 (\sigma_u np)^1; A^2\Sigma_u^+$$

$$\dots (\sigma_g np)^2 (\pi_u np)^4 (\pi_g np)^3 (\sigma_u np)^2; B^2\Pi_g$$

$$\dots (\sigma_g np)^2 (\pi_u np)^3 (\pi_g np)^4 (\sigma_u np)^2; C^2\Pi_u$$

$$\dots (\sigma_g np)^1 (\pi_u np)^4 (\pi_g np)^4 (\sigma_u np)^2; D^2\Sigma_g^+ .$$

The  $A^2\Sigma_u^+$  and  $B^2\Pi_g$  states result from removing an antibonding electron, producing attractive wells, while the  $C^2\Pi_u$  and  $D^2\Sigma_g^+$  states are repulsive. The large  $p\sigma - p\sigma$  overlap makes the  $A^2\Sigma_u^+$  considerably more attractive than the  $B^2\Pi_g$  state.

Inclusion of spin orbit effects will split the  $B^2\Pi_g$  and  $C^2\Pi_u$  states into their  $\Omega = 1/2$  and  $3/2$  components. At large internuclear distances, where spin-orbit interactions are comparable to chemical forces, these systems are best described in Hund's case (c) notation,<sup>29</sup> shown in Table 1. The  $\Omega = 1/2$  component of the  $C^2\Pi_u$  configuration is mixed with the  $A^2\Sigma_u^+$  configuration by spin-orbit interactions, as is the  $\Omega = 1/2$  component of the  $B^2\Pi_g$  configuration with the  $D^2\Sigma_g^+$  configuration. The six case (c) states are designated  $1/2u$  I,  $1/2u$  II,  $1/2g$  I,  $1/2g$  II,  $3/2u$  and  $3/2g$ , where I signifies the lowest lying state of  $1/2u$  or  $1/2g$  symmetry. The ground ionic state is the  $1/2u$  I state. Recalling that the  $A^2\Sigma_u^+$  configuration is attractive, and the  $C^2\Pi_u$  repulsive, the resulting  $1/2u$  I state will become less attractive (dissociative energy will decrease) and the  $1/2u$  II state will become less repulsive (more like a bound state) as the mixing increases.

The experimental dissociation energies of  $Rg_2^+$  decrease monotonically from  $Ne_2^+$  to  $Xe_2^+$ . The spin-orbit splitting of the atomic ionic states increases monotonically. Recent theoretical calculations on the ionic states of the rare-gas systems, without spin-orbit interactions, have given nearly identical potential energy curves for Ne through Xe.<sup>30</sup> To examine the extent to which spin-orbit interactions are responsible for the trend in these dissociation energies, a reduced potential energy (i.e., omitting spin-orbit interactions) is fit to the measured dissociation energies.

The spin-orbit interaction matrices for these states are<sup>31</sup>

$$\Omega = 3/2, \quad \left[ E(^2\Pi) + \frac{1}{2} \zeta \right]$$

$$\Omega = 1/2, \quad \begin{bmatrix} E(^2\Pi) - \frac{1}{2} \zeta & 2^{-1/2} \zeta \\ 2^{-1/2} \zeta & E(^2\Sigma) \end{bmatrix}$$

where  $\zeta$  is the spin-orbit splitting parameter. Using the atomic value of

$$\zeta = \frac{2}{3} \left( E(^2P_{3/2}) - E(^2P_{1/2}) \right)$$

deduced from the ionic  $^2P_{3/2}$  and  $^2P_{1/2}$  states, and treating this Hamiltonian as a perturbation the energies of the two interacting states  $E(^2\Sigma)$  and  $E(^2\Pi)$  can be estimated. This fit is shown in Fig. 6(a), where  $D_e^0 = E(^2P) - E(^2\Sigma)$  and  $T^0 = E(^2\Pi) - E(^2P)$ . In order to fit the  $Ne_2^+$  and  $Ar_2^+$  data  $D_e^0$  must be between 1.37 and 1.41 eV. Using 1.39 eV for  $D_e^0$ ,  $T^0$  is adjusted to fit the  $Xe_2^+$  well depth. This fit, however, overestimates the  $Kr_2^+$  data point by 40 meV.<sup>32</sup> The sensitivity of this procedure to  $T^0$  is very poor as indicated by the lines of  $T^0 = 0$  and  $T^0 = \infty$ , in Fig. 6(a). The best value,  $T^0 = 3.0$  eV, is larger than any of the theoretical calculations of the  $^2\Pi$  state energy at  $R_e$  of the ground ionic state ( $^2\Sigma$ ). However the upper state potential energy curve is steep at this internuclear distance and a small decrease in  $R_e$  makes a large increase in  $T^0$ .



The solutions of the secular equations yield eigenstates given by

$$\frac{1}{2}u \text{ I} = C_1(C^2\Pi_u) + C_2(A^2\Sigma_u^+)$$

$$\frac{1}{2}u \text{ II} = C_2(C^2\Pi_u) - C_1(A^2\Sigma_u^+)$$

with coefficients of the following form

$$C_1 = \left(1 + \frac{\zeta^2/2}{(D_e - \zeta/2 - D_e^0)^2}\right)^{1/2} \quad \text{and} \quad C_2 = (1 - C_1^2)^{1/2} .$$

Numerical values of these coefficients, evaluated at  $R_e$  using the reduced potential, are shown in Table 2. At large internuclear distance, ( $R$ ), these coefficients approach  $C_1 = (1/3)^{1/2} = 0.577$  and  $C_2 = (2/3)^{1/2} = 0.817$ .

The long range form of these ionic states is therefore a strong mixture of the  $\Lambda - \Sigma$  states appropriate near the equilibrium internuclear distance. In addition, at very large internuclear distances the potential is usually better described by dispersion forces. The dominant interaction is an ion-induced dipole,<sup>33</sup> for which the potential is  $-\alpha/2R^4$ , where  $\alpha$  is the polarizability of the rare gas atom. This potential is evaluated in Table 3 at the internuclear separation of the neutral rare gas dimer. The vertical ionization potentials from the photoelectron spectroscopy studies of Dehmer and Dehmer<sup>34</sup> are also shown Table 3 for comparison. In this region of  $R$  the ion-induced dipole interactions account for less than half of the total potential energy. Therefore, chemical forces are still very important even at these large internuclear distances.

In addition, Dehmer and Dehmer<sup>34</sup> estimated from their photoelectron spectra adiabatic ionization potentials of the  $1/2u$  II states, also listed in Table 3. From the shape of the photoelectron band these states have a shallow minima located at only slightly smaller internuclear separation than the van der Waals well. Again a reduced potential energy for these states is derived using the  $Ar_2^+$  and  $Xe_2^+$  data to determine  $D^0$  and  $T_e^0$  respectively. This fit is shown in Fig. 6(b) for  $T_e^0 = -0.05$  eV and  $D^0 = 0.6$  eV. Again, the Kr data point does not fit well and the  $D^0$  is larger than ab initio potential at this interatomic separation. This model fails to yield a reasonable reduced potential at this large internuclear distance. The most likely cause is an additional configuration interaction effect besides spin-orbit interactions.

The first excited ionic state,  $B^2\Pi_{3/2g}(3/2g)$ , is expected to be attractive but not nearly as much as the ground ionic state, because of the weaker  $p\pi - p\pi$  bonding. The minimum of the potential is also expected to lie at larger  $R$  than for the  $1/2u$  I state, because as  $R$  decreases the  $p\sigma_g - p\sigma_g$  antibonding begins to dominate. The photoelectron spectra of  $Ar_2$ ,  $Kr_2$ , and  $Xe_2$  confirm these expectations.<sup>34</sup>

The remaining ionic states,  $C^2\Pi_{3/2u}(3/2u)$ ,  $1/2g$  I ( $B^2\Pi_{1/2g}$ ) and  $1/2g$  II ( $D^2\Sigma_g^+$ ), are expected to be repulsive for long range dispersion minima. A schematic representation of these potentials is shown for Neon in Fig. 7.

## 2. Excited States of Rare Gas van der Waals Dimers

All the excited states of the rare gas molecules are expected to be of the Rydberg type. That is, their energies and the general shapes of the highest occupied orbitals resemble those of hydrogenic systems.

The term value of a diatomic molecular Rydberg states at a given internuclear separation is given by

$$E_n = IP - \frac{RZ_c^2}{(n-\delta(l))^2}$$

where IP is the ionization potential or series limit, R is the Rydberg constant,  $Z_c$  is the charge of the core, n is the principal quantum number and  $\delta(l)$  is the quantum defect. The average radius of a Rydberg electron is given by

$$\bar{r}_n = \frac{(n-\delta(l))^2 a_0}{Z_c}$$

where  $a_0$  is the Bohr radius. The quantum defect,  $\delta(l)$ , is a weak function of n, but it converges more or less rapidly to a constant for large n.

At small R, as n increases, the potential energies of the molecular Rydberg states approach those of the ionic core states due to the high-lying Rydberg electron having less and less probability density in the region of the internuclear axis. In fact, the energy of the first molecular Rydberg state is approximately three-fourths of the ionization potential--much closer in energy to the ionic state than to the ground state. In the rare gas dimers the low-lying ionic states, at small R, are very good approximations to the molecular Rydberg states. Ab initio calculations by Cohen and Schreider<sup>7</sup> on one of the lowest Rydberg states for  $Ne_2$  gave  $D_e + V_{max}^{35}$  of 0.601 eV with  $R_e = 1.79 \text{ \AA}$  while their  $Ne_2^+$   $1/2u$  I values were  $D_e = 1.20 \text{ eV}$  and  $R_e = 1.75 \text{ \AA}$ . Because of this similarity, molecular Rydberg states are, at small R, identified by the

state of its ionic core and the  $n$  and  $l$  values of the Rydberg electron in the united atom (UA). At larger  $R$  these states are better described by LCAO configurations. At very large  $R$  the single configuration LCAO treatment fails by predicting the wrong dissociation products. Either a valence bond approach or a multiconfiguration wavefunction must be used to obtain reasonable descriptions at large internuclear distances. Mulliken<sup>36</sup> has shown that for a molecular Rydberg state with an unpromoted<sup>37</sup> Rydberg molecular orbital, its potential energy curve follows the ionic core at all  $R$ , while in the case of a promoted Rydberg molecular orbital the potential energy curve acquires an obligatory hump at intermediate  $R$ . In both the  $\text{Ne}_2$  absorption spectra and theoretical calculations<sup>7,8</sup> these humps have been found to be usually less than  $600 \text{ cm}^{-1}$ . This is in contrast to the  $\text{He}_2$  Rydberg states with some humps larger than  $4000 \text{ cm}^{-1}$ .<sup>36,38</sup>

At small  $R$  the possible states that arise from coupling the ionic cores with the different possible UA Rydberg electrons are listed in Table 4. Only the lowest lying molecular ionic cores and united Rydberg orbitals of  $s\sigma_g$ ,  $p\sigma_u$ ,  $p\pi_u$ ,  $d\sigma_g$ ,  $d\pi_g$  and  $d\delta_g$  are considered. The higher lying ionic core states will be above the energy region of concern, that is below the  $^2P_{3/2,1/2}$  atomic ionization potentials. Larger  $\lambda$  valued ( $\lambda > 3$ ) UA Rydberg orbitals can be of importance but will produce states similar to the ones shown here.

Mulliken has shown that Rydberg states with  $C^2\Pi_u$  and  $D^2\Sigma_g^+$  core configurations dissociate to  $\text{Rg}^+ + \text{Rg}^-$ , or since  $\text{Rg}^-$  is unstable, to  $\text{Rg}^+ + \text{Rg} + e^-$ .<sup>6</sup> Therefore, although some of these states are possibly attractive they lie much closer in energy to the atomic ionization

potential than those of the  $A^2\Sigma_u^+$  and  $B^2\Pi_g$  cores. This eliminates half of the states listed in Table 4. Of the remaining states only the following satisfy dipole selection rules for excitation from the  $Rg_2$  ground state:

$A^2\Sigma_u^+ m\sigma_g$	$Ou^+, 1u$
$B^2\Pi_g m\rho\sigma_u$	$Ou^+, (2)1u$
$B^2\Pi_g m\rho\pi_u$	$(2)Ou^+, (3)1u$
$A^2\Sigma_u^+ m\delta_g$	$Ou^+, 1u$
$A^2\Sigma_u^+ m\delta_g$	$Ou^+, (2)1u$
$A^2\Sigma_u^+ m\delta_g$	$1u$

As the internuclear distance increases the Rydberg electron will spend more time in the internuclear region. The Rydberg state described by the ionic core is perturbed by the electron and becomes better characterized by LCAO or VB wavefunctions. Although the Rydberg electron loses its united atom quantum numbers  $m$  and  $\ell$ , it retains its projection upon the internuclear axis,  $\lambda$ . At still larger  $R$  the Rydberg electron will become more localized on one or other rare gas atoms, regaining principal ( $n'$ ) and orbital angular momenta quantum numbers. For unpromoted Rydberg MO's  $n'$  and  $m$  are equal. The resulting dissociation limits are either an excited Rydberg atom and ground state atom or the ion, a ground state atom and a free electron. The symmetries of the Rydberg states derived from the former dissociation products are given in Table 5. The  $(j,\ell)$  coupling scheme for the rare-gas Rydberg atomic state is employed where  $j$  is the cores total angular momentum and  $\ell$  is the orbital angular momentum of the Rydberg electron. This type of

coupling, like  $j, j$  coupling, gives pairs of states.<sup>24</sup> The number in the brackets (Table 5) is the average  $J$  value of the pair of states.

If the order of the UA Rydberg limits were known the exact state correlation diagram could be drawn in the usual fashion. Mulliken has estimated these energies for  $Xe_2 6s$  and  $5p$  Rydberg states creating approximate potential energy curves.<sup>6</sup> Several reasonable assumptions were used concerning the united atom limits. These assumptions are:

$${}^2P_{ns} + {}^1S_0 + ns\sigma_g \text{ or } (n+1)p\sigma_u$$

$${}^2P_{np} + {}^1S_0 + (n+1)d\sigma_g, np\pi_u, (n+1)d\pi_g, (n+2)f\sigma_u .$$

The corresponding relationship for the  $d$  states is:

$${}^2P_{nd} + {}^1S_0 + (n+3)g_g, (n+2)f\pi_u, nd\delta_g, (n+2)f\delta_u, (n+3)g\pi_g, (n+4)h\sigma_u .$$

The correlation diagram, not drawn to scale, for an  $ns$  Rydberg state is shown in Fig. 8. Schematic potential energy curves for the  $6s$  states of  $Ne_2^*$  are depicted in Fig. 7. Of the total 16 states only 5 are dipole allowed. Of these five, two are  $O_u^+$  and three are  $lu$  symmetry. The lowest lying  $lu$  state retains a significant  ${}^3\Sigma_u^+$  character at all internuclear distance, nearly coincident with the  $O\bar{u}$  state. Therefore, transitions to this state are not expected to be intense. The next highest state,  $O_u^+$ , has the  $A^2\Sigma_u^+$  core and closely resembles it. The next highest  $lu$  state has a  $B^2\Pi_{3/2g}$  core. This core state is overall repulsive but with a long-range minimum as previously described. The Rydberg state should resemble the core state at small  $R$  but dissociate over a maximum, characteristic of a promoted MO. Thus, this state is

most likely repulsive in the vertical transition region of the van der Waals molecule. The remaining two dipole allowed states ( $O\bar{u}^+$ ,  $lu$ ) have  $B^2\Pi_{1/2g}$  cores. The ionic state ( $B^2\Pi_{1/2g}^+$ ) is believed to be repulsive, aside from a possible attractive dispersion minima. However, the Rydberg states of  $O\bar{u}^+$  symmetry are a mixture of two LCAO configurations at large  $R$ , due to spin-orbit interactions. One of these configurations is primarily responsible for the attractiveness of the lowest  $O\bar{u}^+$  ( $A^2\Sigma_{1/2u}^+$  core) state. The other configuration is repulsive. The spin-orbit interaction mixes these two configurations. Therefore, the higher lying  $O\bar{u}^+$  state is less repulsive than its predominant ionic core configuration,  $B^2\Pi_{1/2g}^+$ . This effect, as well as the attractive dispersion force, give this state a long range minimum.

As far as the p Rydberg state are concerned, the energy order of the united atom (UA) molecular states are not known, making a definitive correlation diagram impossible to construct. Mulliken estimated both the energy order for the lowest UA states and Rydberg potential energy curves.<sup>6</sup> Using an ordering similar to Mulliken for the UA states Fig. 9 was constructed. Only the  $O\bar{u}^+$  and  $lu$  correlations are shown. In these atomic limits only  $J = 0$  and  $J = 2$  produce  $O\bar{u}^+$  and  $lu$  states. The  ${}^2P_{3/2}np$  manifold forms three  $O\bar{u}^+$  and five  $lu$  states while the  ${}^2P_{1/2}np$  manifold gives two states of  $O\bar{u}^+$  and three of  $lu$  symmetry. At small  $R$  the UA limit of  $A^2\Sigma_{1/2u}^+(n+1)d\pi_g$  forms an  $O\bar{u}^+$  and two  $lu$  states, while the  $A^2\Sigma_{1/2u}^+(n+1)d\sigma_g$  yields a  $O\bar{u}^+$  state and a  $O\bar{u}$ ,  $lu$  state. This latter  $lu$  state is derived from a  ${}^3\Sigma_u^+$  configuration and, as noted before, is expected to have a small cross-section. Therefore, the existence of two  $O\bar{u}^+$  and two  $lu$  states shaped like the  $A^2\Sigma_{1/2u}^+$  ionic

state is predicted. Two  $O_u^+$  and three  $l_u$  states result from coupling a new Rydberg electron to a  $B^2\Pi_g$  core. One of these  $O_u^+$  and three  $l_u$  states are expected to have significant  $^3\Sigma_u^+$  character, and thus small cross-sections. Finally the  $B^2\Pi(n+2)f_{O_u}$  states has one  $O_u^+$  and two  $l_u$  components.

The nd Rydberg states are even more numerous than the np Rydberg states. There are four  $O_u^+$  and seven  $l_u$  states derived from  $^2P_{3/2}nd + ^1S_0$  and two  $O_u^+$  and four  $l_u$  states resulting from  $^2P_{1/2}nd + ^1S_0$ , with only  $J = 1$  or 3 atomic states contributing. In the UA limit the  $A^2\Sigma_{1/2u}^+$  core is responsible for two  $O_u^+$  and four  $l_u$  states, the  $B^2\Pi_{3/2g}$  core creates only one  $O_u^+$  and three  $l_u$  states, and the  $B^2\Sigma_{1/2g}$  core gives three  $O_u^+$  and four  $l_u$  states. If the  $A^2\Sigma_{1/2u}^+$  core UA states lie lower in energy than those with a  $B^2\Pi_g$  core, there will be at least one  $O_u^+$  state with an  $A^2\Sigma_{1/2u}^+$  core and an atomic limit of  $^2P_{3/2}nd$ . The other  $O_u^+$  state will probably also have an  $^2P_{3/2}nd$  atomic limit. The lower of these two  $O_u^+$  states will have an atomic parentage of  $J = 1$ . A plausible correlation diagram for these  $O_u^+$  and  $l_u$  states is shown in Fig. 10.

### 3. Ionization Process

Photoabsorption studies of molecules above the ionization potential indicate that both continuous and "discrete" processes play an important role. The familiar energy conservation equation is indicated below:

$$A(E_{INT}^{\prime\prime}) + h\nu + A^+(E_{INT}^{\prime}) + e^-(KE)$$

$$E(h\nu) = E_{INT}^{\prime} - E_{INT}^{\prime\prime} + KE + IP$$



where  $E_{INT}''$  and  $E_{INT}'$  are the internal energies of the neutral and ion respectively, KE is the kinetic energy of outgoing electron and IP is the adiabatic ionization potential. The transition moment for dipole radiation between the initial state  $\psi''$  and the final state (ion and electron)  $\psi'$  is

$$\underline{M} = \langle \psi'' | \Sigma p | \psi' \rangle .$$

Using the Born-Oppenheimer approximation the transition probability is proportional to

$$|\langle \psi_e''(\mathbf{r}, R) | \Sigma p_e | \psi_e''(\mathbf{r}, R) \rangle|^2 |\langle \psi_v''(R) | \psi_v'(R) \rangle|^2 .$$

The first term is a slowly varying function of R, and non-zero for single excitations, due to the fact that the free-electron wavefunction is not restricted with respect to its orbital angular momentum or energy. The free electron final state is responsible for the continuous nature of this process.

The "discrete" processes are also included in these matrix elements, if the full Hamiltonian and true eigenstates of the system are used. However, the popular one-electron one-orbital and Born-Oppenheimer pictures of a molecule does not adequately account for all of the observed processes.<sup>39</sup> The approach usually taken is to use perturbation theory to account for missing terms in the Hamiltonian. This is most useful when calculating perturbations that the initial basis set can easily accommodate. When this is not the case, the more difficult task of increasing the basis set and including a more complete Hamiltonian in a variational calculation should be followed.

The "discrete" processes in the ionization of molecules have classically been described as involving two steps. First, the photon excites a "discrete" state in the ionization continuum which then decays via autoionization (AI) to the ionic state and an electron. For atoms, Fano and Cooper<sup>40</sup> demonstrated that the details of autoionization process cannot be described using the above model since there is in fact, no intermediate state. In essence, the Hamiltonian that would couple the imaginary discrete state to the continuum cannot be turned on and off at will. However, the gross features of autoionization can be estimated by examining the process with a perturbation Hamiltonian. The matrix elements are of the form

$$\langle \psi' | H' | \psi^* \rangle$$

where  $H'$  is the perturbation and  $\psi^*$  is the discrete state that is autoionized.

Several different types of AI have been observed in atomic and molecular systems. For molecules excited only slightly above the first ionization potential the predominant processes are vibrational and electronic AI. Vibrational AI involves the transfer of vibrational energy of the AI state to kinetic energy in the out-going electron. Treatments by Berry et al.<sup>41-43</sup> have shown that for  $H_2$  the dominate perturbation element is of the form:

$$\langle \psi_e' \psi_v' | \frac{\partial}{\partial R} \psi_e^* | \langle \frac{\partial}{\partial R} \psi_v^* \rangle$$

where  $\psi_v^*$  is the vibrational wavefunction of the AI state. They found a propensity rule for this type of AI which is  $v^* - v' = 1$ , and an increase in intensity with increasing  $v^*$ . Their results adequately explain the photoionization efficiency of  $H_2$ . However, this propensity rule, does not work well for  $N_2$  or  $NO$ , where  $v^* - v' = 1, 2, 3$  transitions have been observed.<sup>43,44</sup> For  $H_2$ , the nuclear momentum operator term considered by Berry et al. is the most important. However, when this terms is small, the other terms in their model dominate. These are

$$\begin{aligned} & \langle \psi_e' | \partial^2 / \partial R^2 | \psi_e^* \rangle \langle \psi_v' | \psi_v^* \rangle \langle \psi_r' | \psi_r^* \rangle \\ & \langle \psi_e' | \hat{J} - \hat{L} | \psi_e^* \rangle \langle \psi_r' | \hat{J} - \hat{L} | \psi_r^* \rangle \langle \psi_v' | \psi_v^* \rangle \\ & \langle \psi_e' | (\hat{J} - \hat{L})^2 | \psi_e^* \rangle \langle \psi_r' | \psi_r^* \rangle \langle \psi_v' | \psi_v^* \rangle . \end{aligned}$$

The first term is the largest and only when the shape of the AI state differs significantly from the final ionic state.<sup>41</sup> This can be the case when an AI Rydberg state core is different than the final ionic state. However, no longer will just vibrational energy be transferred to the electron, but in addition electronic energy from the core relaxation. This process is referred to as electronic AI. The matrix elements that control this interaction will have the form

$$\langle \psi_e' | \frac{1}{r_{jk}} | \psi_e^* \rangle$$

where  $e^2/r_{jk}$  is the repulsion between the Rydberg electron and some core electron.

Smith<sup>44</sup> has derived the vibrational intensity dependence of AI by using the formalism of Fano. There are two distinct cases: 1) where the excitation width is narrower than the AI resonance

$$I \propto |\langle \psi'_v | \psi''_v \rangle|^2 + |\langle \psi'_v | \psi^*_v \rangle|^2 |\langle \psi^*_v | \psi''_v \rangle|^2 \cdot q^2$$

where  $q$  is the enhancement due to autoionization; and, 2) when the excitation width  $\delta(h\nu)$  is larger than  $\Gamma$  the resonance width. The ionic state vibrational distribution will be described by

$$I \propto |\langle \psi'_v | \psi''_v \rangle|^2 + |\langle \psi'_v | \psi^*_v \rangle|^2 |\langle \psi^*_v | \psi''_v \rangle|^2 \frac{\pi q^2 \Gamma}{2\delta(h\nu)} .$$

The shape of the resonance is given by

$$\sigma(E) = \sigma_0(E) (q + \epsilon)^2 / (1 + \epsilon^2)$$

where  $\sigma_0(E)$  is the cross section in the absence of the resonance, and  $\epsilon$  is the reduced energy,  $\epsilon = (E - E_r) / (1/2\Gamma)$ . Characteristic features of AI are an asymmetrical line shape and vibrational state populations proportional to the products of Franck-Condon type factors.

Recalling that vibrational AI occurs when the Rydberg state core is the same as the ionic state and that the ionic vibrational state populations are controlled by the propensity rule, the outgoing electrons will have, at most, kinetic energies equal to a vibrational quantum. As the excitation energy increases above threshold the majority of the excess energy is left in internal degrees of freedom of the molecular ion. In contrast, electronic AI can produce electrons as energetic as those produced by direct ionization (i.e.,  $h\nu - IP$ ). Electronic

AI has been observed in several systems. Recent studies on  $N_2O$ <sup>46,47</sup> have shown that AI can also produce very low kinetic energy electrons.

#### 4. Rare Gas van der Waals Dimer Ionization

The rare gas van der Waals minimum lies at a much larger inter-nuclear distance than the ionic state minimum. Therefore, direct ionization populates only the very high vibrational states of the ion. This results in an vertical ionization potential for the  $A^2\Sigma_u^+$  state much larger than the adiabatic IP. For example, the  $Ar_2^+$ ,  $2\Sigma_{1/2u}^+$ , vertical IP is 15.55 eV while the adiabatic IP is at least 14.44 eV, a difference of 1.11 eV.<sup>34</sup> The vertical transition is to approximately  $v' = 40$  of the ionic state with its  $v'_{max} = 49$ , and has a width of approximately 16 states.<sup>47</sup> Schneider and Cohen calculated Franck-Condon factors for the theoretical potential for a similar state in  $Ne_2$  and found them to be exceedingly small, less than  $10^{-10}$  for the lowest  $v'$  levels.<sup>48</sup> This evidence as well as the measured photoionization efficiency curves from this laboratory rule out direct ionization as a possible mechanism for production of the dimer ions near threshold. The sharp structures in the yield curves are most certainly due to AI molecular Rydberg states of the rare gas dimers. In fact, these states have significant cross-sections very close to the adiabatic ionization potential. As previously discussed, there are two possible AI processes to be considered. Vibrational autoionization will be first.

The type of state necessary for vibrational AI is one that is very similar in shape to the ionic state. Since the ground ionic state is  $A^2\Sigma_{1/2u}^+$  (indeed, quite different from the other ionic states) the Rydberg states involved must have this core. As previously noted, there

are several states of this type with the proper symmetry that can be reached by dipole selection rules. However, like the A state, in the vertical transition region, at large R, they can only be populated in high v states. For this type of autoionization, if the propensity rule is valid, only high v states of the ion can be produced, as shown in Fig. 11(a). Consequently, vibrational AI will not produce ions near threshold.

On the other hand, electronic AI is not restricted by the propensity rule. The vibrational states populated are governed by Franck-Condon type factors and the dipole matrix elements between true eigenstates. The importance of configuration interaction modifying the results obtained by using single configuration wavefunctions in similar situations has been described elsewhere.<sup>31</sup> Recalling that the description of the  $B^2\Pi_g$  core Rydberg state at large R is indicative of considerable mixing with the A core configuration by spin-orbit interactions, these dipole matrix elements might be significant. In addition, the Rydberg states with predominantly  $B^2\Pi_g$  cores have larger Franck-Condon factors coupling to the ground state, due both to their large  $R_e$ , and to their widths. They will also have significant Franck-Condon factors coupling to the ground ionic state. The Franck-Condon overlaps are demonstrated in Fig. 11(b).

In the perturbation approach this process is an energy transfer between the core and the Rydberg electron. The perturbation Hamiltonian is the Rydberg electron-core repulsion. This type of perturbation is similar to that responsible for the pronounced AI in the rare gas atoms.

It has also been used to explain observed AI in molecular systems like,  $N_2$ <sup>49</sup>.

High resolution VUV absorption spectra of the rare gas dimers have been reported.<sup>8-14</sup> All of the states observed were molecular Rydberg states in character, formed from Rydberg atomic states and ground state atoms. These studies are limited to relatively-low lying Rydberg states by the extensive broadening of the numerous atomic lines. This is in contrast to the photoionization studies reported here which (although of much lower resolution) are not sensitive to the atomic transitions or to strongly dissociative molecular states. For both  $Ne_2$  and  $Ar_2$  few states above the adiabatic IP were assigned in addition to the many lower-lying states. Nevertheless, several generalizations are made from the reported absorption data.

Two Rydberg molecular states are observed which arise from the  $2P_{3/2}ns + 1S_0$  atomic limits. The lower lying of these is assigned to the  $1u$  state which consists of an extension  $v'$  progression up to the dissociation limit (10 bands) and is about a factor of 10 less intense than the higher energy state. The higher states are most likely  $O_u^+$  and display a somewhat shorter  $v'$  progression to the dissociation limit. As indicated beforehand, these states have a  $A^2\Sigma_{1/2u}^+$  core.

In the region of the  $2P_{1/2}n$  atomic limit, a  $O_u^+$  state which has a much smaller vibrational spacing, but an intensity comparable to that of the lower  $O_u^+$  state is observed. This lower vibrational frequency is just what is anticipated for a Rydberg state with a  $B^2\Pi_{3/2g}$  core.

At least three systems are observed near the  $np$  atomic states. The highest energy state has the longest  $v'$  progression and the most intensity. It is assigned to a  $Ou^+$  state, dissociating to  ${}^2P_{1/2}np$  ( $J = 0$ ) and  ${}^1S_0$  atoms. The lower systems of bands are approximately 25% as intense with only a few  $v'$  states observed. These systems have not been conclusively assigned. As a whole the  $np$  systems are a factor of 200 less intense than the  $Ou^+$  states observed in the  $ns$  series for  $Ne_2$  but increase intensity from the heavier rare gases.

Several of the band systems for  $Ne_2$  and  $Xe_2$  in the region  ${}^2P_{3/2}nd$  states appear to be similar in structure and only slightly less intense than the  $Ou^+$  states derived from  ${}^2P_{3/2}ns$  atoms. Only two systems in the region of the  ${}^2P_{3/2}$  states are observed in  $Ne_2$ , being assigned to  $Ou^+$  molecular states dissociating to  ${}^2P_{3/2}3d[1/2]_1$  plus  ${}^1S_0$  and  ${}^2P_{3/2}3d[3/2]_1$  plus  ${}^1S_0$  atoms. Many additional systems are observed in  $Xe_2$ ; however, state symmetries are not assignable, due to irregular vibrational spacing, which might be evidence a curve crossing.

A  ${}^2P_{1/2}nd$  and  ${}^1S_0$  atom couple to two  $Ou^+$  and four  $lu$  molecular states. Only in  $Ne_2$ , have systems in this energy range been reported, but atomic limits were still not assigned. The vibrational spacings are irregular suggesting the possibility of two states or a curve crossing. It is reasonable to assume that at least the highest of these systems would have  $B^2\Pi_g$  core.

Because the states involved in the AI of the rare gas dimmers are the same as those observed in absorption but modified in intensity by coupling with the continuum and Franck-Condon factors, the following predictions are made.



- I). Of the molecular Rydberg states derived from  ${}^2P_{3/2}ns$  or  $nd$  atoms and a ground state atom, the ones with an  $A^2\Sigma_{1/2}^+$  core will be more intense in absorption than in photoionization near threshold.
- II). Considering the states with atomic limits of  ${}^2P_{1/2}ns$  or  $nd$  plus  ${}^1S_0$ , the most intense will have  $O\dot{u}^+$  symmetry with a  $B^2\Pi_g$  core and appear with comparable intensity in both absorption and in photoionization.
- III). The states with  ${}^2P_{1/2,3/2}np$  atomic limits will be weak for  $Ne_2$  and increase in intensity for the heavier systems. Again we expect the  $B^2\Pi_g$  core Rydberg states to be more pronounced in photoionization spectra than absorption spectra.

Figure 12 shows the photoionization efficiency of  $Ne_2$  in the region of the sharp A1 structure near threshold. In the top position of this figure, the absorption data of Tanaka and Yoshino<sup>8</sup> are plotted. The first peak, which is red-shifted from the atomic  ${}^2P_{1/2}5s$  state, agrees with system XII in absorption. This is an  $O\dot{u}^+$  with a  $B^2\Pi_{1/2g}$  core. The absence of an intense peak corresponding to system XI ( $O\dot{u}^+$  from  ${}^2P_{3/2}5s$ ) is consistent with prediction I, namely, that a  $A^2\Sigma_{1/2}^+$  core Rydberg state will not be efficient in autoionization near threshold. The second peak in the efficiency curve lies coincident in energy with the  ${}^2P_{3/2}4d$  atomic states. If the energy ordering of the UA states indicated in Fig. 10 is correct, there will be two  $O\dot{u}^+$  states and three  $1u$  states with  $B^2\Pi_g$  cores and two  $O\dot{u}^+$  states and four  $1u$  states with  $A^2\Sigma_{1/2}^+$  cores. It is possible that, again, the B core states yield significant intensity; however, the A core states can not be ruled out.

If the A core states make a significant contribution to this peak, prediction I would be contradicted. Unfortunately, absorption studies have not been reported in this energy region.

The third peak is red-shifted from  ${}^2P_{1/2}4d$  atomic state which produces two  $O_u^+$  states and three  $l_u$  states, all certainly with B core. The observed red-shift of this state is in excellent agreement with the  ${}^2P_{1/2}3d$  state reported from absorption measurements. The intensity of this peak is as expected from prediction I. There are several  ${}^2P_{3/2}5p$  states in this energy region which might contribute, but not to a significant degree.

The fourth peak, which is weak and well removed from Ne s and d atomic states, is red-shifted from the  ${}^2P_{1/2}5p$  states. The molecular state responsible for this structure will have a  $B^2\Pi_g$  core. Although this peak is weak, it is twenty times as intense as  ${}^2P_{1/2}3p$  and  $4p$  analogues seen in absorption studies. This behavior is in agreement with prediction III.

The  ${}^2P_{3/2}6s$  state of neon lies slightly to the blue of the maximum of the fifth peak. There are no other known atomic states between the  ${}^2P_{3/2}6s$  and  ${}^2P_{3/2}5d$  states of Ne. Therefore this peak's blue shift is assigned as AI through the repulsive  $l_u$  state derived from  ${}^2P_{3/2}6s$ ,  $J = 1$  and  ${}^1S_0$  combination. This state is responsible for the broadening, toward the blue, of the atomic line in absorption at high pressures. It has a  $B^2\Pi_{1/2g}$  core, and a positive dispersion force, and a promoted Rydberg MO. All of these effects make this state repulsive; however, an avoided crossing at large R can yield a local minimum. Fig. 11(c) shows how such a local minimum can enhance the autoionization cross-

section over that for a completely repulsive state. The red-shifted portion of this peak, in the photoionization efficiency, is due to the  $Ou^+$  state with an  $A^2\Sigma_{1/2u}^+$  core. It is the higher energy analog of the state responsible for system XI in the absorption spectra of Tanaka and Yoshino.<sup>8</sup>

The sixth peak is coincident with  $^2P_{3/2}5d$  states, red-shifted from the  $^2P_{1/2}6s$  state and broader than the other intense peaks. This peak is assigned to molecular states arising from both of the atomic states. This assignment is consistent with the first and second peaks both in red-shift and intensity.

The seventh and final peak to be assigned is red-shifted from the  $^2P_{1/2}5d$  just as the third peak is from the  $4d$  state. Its intensity is consistent with prediction II.

At higher photon energy the density of states increases, thereby blending the peaks together and preventing further assignments with the available resolution. Below the onset of the sharp structure, the photoionization efficiency decays very slowly to threshold. Several processes contribute to this decay. The largest of these will still be autoionization. The atomic states in this energy region are  $^2P_{3/2}5s$ ,  $^2P_{1/2}4p$  and  $^2P_{3/2}4p$ . The observed ionization potential is in the region where AI states from  $^2P_{1/2}4p + ^1S_0$  are predicted to have intensity in analogy with the fourth peak.

The photoionization efficiency of  $Xe_2$ ,  $Kr_2$  and  $Ar_2$  studied in this laboratory by Ng et al. are shown in Fig. 13. The smaller  $D_0$  of these ions, the stronger spin-orbit interactions, and the poorer resolution made assignments similar to those for  $Ne_2$  impossible. However, an

obvious trend is observed in going from  $\text{Ar}_2$  to  $\text{Xe}_2$ . The major intensity in  $\text{Ar}_2$  is in the region of the ns and nd, states while for  $\text{Kr}_2$  considerable intensity is observed between these states, and for  $\text{Xe}_2$  this tendency is lost. In the absorption studies for these systems, the np type states increase in intensity in going from Ne to Xe. In addition any propensity towards  $\Omega = 0$  instead of  $\Omega = 1$  is expected to decrease with increasing spin-orbit interaction. Therefore, the number of accessible states will increase in going from  $\text{Ne}_2$  to  $\text{Xe}_2$ , resulting in the observed trend in the photoionization efficiencies of the rare gas systems.

Very recent photoionization mass spectrometric results, on  $\text{Ar}_2$ , reported by Dehmer and Poliakoff<sup>50</sup> using higher resolution, show that indeed the broad structure in Fig. 13 is comprised of several electronic states. They assigned the first band system above threshold, which is also observed in absorption spectra by Tanaka et al.,<sup>9</sup> to a state derived from  $^2P_{1/2}5p + ^1S_0$  atoms. Similarly, an analogous state in Ne,  $^2P_{1/2}4p + ^1S_0$ , is predicted to be responsible for the observed threshold signal in this work.

##### 5. (He)<sub>n</sub> Discussion

Supersonic expansions are excellent sources of weakly bound clusters. By combining this technique with photoionization mass spectroscopy it was hoped that the stability or instability of  $\text{He}_2$  could be determined. The key to the experiment is observation of not only  $\text{He}_2^+$  ion but also the  $\text{He}_3^+$  ion. If  $\text{He}_3^+$  is more stable than  $\text{He}_2^+$ , photoionization yield measurements between the two thresholds would quantify the  $\text{He}_3$  component in the beam. The  $\text{He}_2^+$  produced by dissociative photoionization could

then be estimated above the  $\text{He}_2^+$  appearance potential. However, no  $\text{He}_3^+$  ions were observed; and, in fact, the only significant  $\text{He}_2^+$  yield was at autoionization resonances. In addition, a decrease in beam intensity, which resulted from a partially clogging nozzle, prevented reproducible pressure measurements.

The most likely source of the observed  $\text{He}_2^+$  ion was dissociative photoionization of larger clusters. Unfortunately, the observed autoionization structure cannot be assigned to molecular states since the initial molecular species remains undetermined. Nevertheless, the major features of the spectrum can still be rationalized by considering a hypothetically bound  $\text{He}_2$  molecule.

The lowest molecular ionic states of  $\text{He}_2^+$  are  $A = 1s\sigma_u^2 1s\sigma_g$  and  $B = 1s\sigma_u 1s\sigma_g^2$ . The B state dissociates into an ion pair ( $\text{He}^+ + \text{He} + e^-$ ) while the A state forms an excited Rydberg He atom and a ground state atom ( $\text{He}^* + \text{He}$ ). The Rydberg states of  $\text{He}_2$  have been extensively studied<sup>20,51,52</sup> and Mulliken has estimated their potential energy curves.<sup>36</sup> The Rydberg states pertinent to this work have dissociation products of  $2Snp + 1S$  symmetry. These atomic limits are given on the top of Fig. 5. The wavelength offset for this scan, due to instrumental problems, was determined by aligning the atomic ionization potential with the onset which is indicated in the figure. The accuracy of this procedure is estimated to be  $\pm 0.3 \text{ \AA}$ . Therefore, the red-shifts are real, as expected for this type of a molecular system, but their values cannot be accurately determined.

## E. Conclusions and Summary

The dissociation energy,  $D_0$ , of  $\text{He}_2^+$  is determined to be greater than  $1.36 \pm 0.05$  eV by photoionization mass spectroscopy. A simple spin-orbit interaction model is shown to explain the decrease in the dissociation energies of the heavier rare-gas molecular ions. The supersonic molecular beam technology and intense continuum synchrotron radiation source, employed in this work, yielded sufficient signal to resolve a few of the lowest autoionizing molecular Rydberg states. Careful consideration, of the autoionization mechanism(s), absorption spectra, and electronic configurations of the molecular Rydberg states led to several assignments in the photoionization efficiency. The molecular Rydberg states with  $B^2\Pi_g$  core configurations are found to make the most important contribution to the photionization cross-section near threshold, due to their ability to bridge the excitation between the large initial R of the van der Waals dimer and the small R of the ionic molecular state. Vibrational autoionization is shown not to be a plausible mechanism near threshold due to the vertical transition region at the large internuclear distance of the van der Waals molecule. Electronic autoionization is not restricted as such and is expected to be further assisted by the spin-orbit interaction's ability to mix A core character into a B core molecular Rydberg state.

Finally, the search for the elusive  $\text{He}_2$  molecule failed. The observed  $\text{He}_2^+$  signal was most likely due to complete dissociative autoionization of  $\text{He}_3$ .

**References: Chapter II**

1. N. Helm, K. Stephan and T. D. Mark, *Phys. Rev. A* 19, 2154 (1979).
2. R. E. Huffman and D. H. Katayama, *J. Chem. Phys.* 45, 138 (1966).
3. T. R. Connor and M. A. Biondi, *Phys. Rev.* 140, A778 (1965) and  
L. Frommhold and M. A. Biondi, *ibid.* 185, 244 (1969).
4. C. Y. Ng, D. J. Trevor, B. H. Mahan, and Y. T. Lee, *J. Chem. Phys.*  
65, 4327 (1976).
5. C. Y. Ng, D. J. Trevor, B. H. Mahan and Y. T. Lee, *J. Chem. Phys.*  
66, 446 (1977).
6. R. S. Mulliken, *J. Chem. Phys.* 52, 5170 (1970).
7. For example see J. C. Cohen and B. Schneider, *J. Chem. Phys.* 61,  
3230 (1974); and W. R. Wadt, *J. Chem. Phys.* 68, 402 (1978).
8. Y. Tanaka and K. Yoshino, *J. Chem. Phys.* 57, 2964 (1972).
9. Y. Tanaka and K. Yoshino, *J. Chem. Phys.* 53, 2012 (1970).
10. Y. Tanaka, K. Yoshino and D. E. Freeman, *J. Chem. Phys.* 59, 5160  
(1973).
11. D. E. Freeman, K. Yoshino, and Y. Tanaka, *J. Chem. Phys.* 61, 4880  
(1974).
12. M. C. Gastex and N. Damany, *Chem. Phys. Letters* 13, 158 (1972).
13. M. C. Gastex and N. Damany, *Chem. Phys. Letters* 24, 437 (1974).
14. M. C. Gastex, *Chem. Phys.* 5, 448 (1974).
15. P. E. Siska, J. M. Parson, T. P. Schafer, and Y. T. Lee, *J. Chem.  
Phys.* 55, 5782 (1971).
16. P. J. Bertoncini and A. C. Wahl, *J. Chem. Phys.* 58, 1259 (1973);  
B. Liu and A. D. McLean, *J. Chem. Phys.* 59, 4557 (1973).

17. R. A. Aziz, V. P. S. Nain, J. C. Carley, W. L. Taylor, and G. T. McConville, *J. Chem. Phys.* 70, 4330 (1979); M. Krauss, D. B. Neumann and W. J. Stevens, *Chem. Phys. Lett.* 66, 29 (1979); V. V. Starykh and V. K. Kapyshev, *J. Chem. Phys.* 72, 2713 (1980).
18. A. P. J. van Deursen and J. Reuss, *J. Chem. Phys.* 63, 4559 (1975).
19. P. W. Stephens and J. G. King, *Bull. Am. Phys. Soc.* 23, 240 (1978).
20. Y. Tanaka and K. Yoshiro, *J. Chem. Phys.* 50, 3087 (1969).
21. V. Rehn, A. D. Baer, J. L. Stanford, D. S. Kyser and V. O. Jones, *Proc. of the Int. Conf. on Vacuum Ultraviolet Rad. Physics IV*, 780 (1974).
22. M. G. White, R. A. Rosenberg, G. Gabor, E. D. Poliakoff, G. Thornton, S. H. Southworth and D. A. Shirley, *Rev. of Sci. Instrum.* 50, 1268 (1979).
23. J. R. Samson, "Techniques of Vacuum Ultraviolet Spectroscopy," John Wiley and Sons, Inc. (1967).
24. C. E. Moore, "Atomic Energy Levels: Vol. I," Circular of the Nat. Bureau of Stand. 467 (1949).
25. B. Brunett, R. Cambi, F. Pirani, F. Vecchiocattivi and M. Tomassini, *Chem. Phys.* 42, 397 (1979).
26. M. S. B. Munson, J. L. Franklin and F. H. Field, *J. Phys. Chem.* 67, 1542 (1963).
27. E. A. Mason and J. T. Vanderslice, *J. Chem. Phys.* 30, 599 (1959).
28. J. A. Barker, R. O. Watts, J. K. Lee, T. P. Schafer, and Y. T. Lee, *J. Chem. Phys.* 61, 3081 (1974).



29. G. Herzberg, "Molecular Spectra and Molecular Structure, I. Spectra of Diatomic Molecules," second edition Van Nostrand Reinhold Co. (1950).
30. H. H. Michels, R. H. Hobbs and L. A. Wright, J. Chem. Phys. 69, 5151 (1978).
31. E. U. Condon and G. N. Shortly, "The Theory of Atomic Spectra" Cambridge University Press (1957).
32. The values of  $D_0$  used are from Ref. 5 and 50. The  $Kr_2$  threshold measured in Ref. 5 is the least accurate due to very low lamp intensity in this region. However it is doubtful that it is high by as much as 40 meV.
33. H. Margenau, Rev. of Modern Phys. 2, 1 (1939).
34. P. M. Dehmer and J. L. Dehmer, J. Chem. Phys. 68, 3462 (1978), 69, 125 (1978).
35. In their calculations this state,  $Ou^+$ , dissociates over a maximum  $V_{max} = 0.198$  eV.
36. R. S. Mulliken, Phys. Rev. A36, A962 (1964).
37. R. S. Mulliken, J. Amer. Chem. Soc. 86, 3183 (1964), 88, 1849 (1965).
38. S. L. Guberman and W. A. Goddard, Phys. Rev. 12A, 1203 (1975).
39. D. A. Shirley, J. De Physique Sup. 7 39, C4 (1978).
40. U. Fano and J. W. Cooper, Rev. Modern Phys. 40, 441 (1968).
41. R. S. Berry and S. E. Nielsen, Phys. Rev. 1A, 395 (1970).
42. G. B. Shaw and R. S. Berry, J. Chem. Phys. 56, 5808 (1972).
43. J. Berkowitz and W. A. Chupka, J. Chem. Phys. 51, 2341 (1969).
44. E. Miescher, Y. T. Lee and P. Gunther, J. Chem. Phys. 68, 2753 (1978).

45. A. L. Smith, *Phil. Trans. Roy. Soc. London* A268, 169 (1970).
46. I. Nenner, P. Guyon, T. Baer, and T. R. Govers, *J. Chem. Phys.* 72, 6587 (1980).
47. P. M. Dehmer, J. L. Dehmer and W. A. Chupka, *J. Chem. Phys.* 73, 128 (1980).
48. Estimated from  $\omega_e$  and  $\omega_e X_e$  of the theoretical potential given in Ref. 30.
49. B. Schneider and J. S. Cohen, *J. Chem. Phys.* 61, 3240 (1974).
50. P. M. Dehmer and E. D. Poliakoff, "VI International Conference on Vac. Ultraviolet Rad. Phys." (1980).
51. M. L. Ginter, *J. Chem. Phys.* 42, 561 (1965).
52. K. P. Huber and G. Herzberg, "Molecular Spectra and Molecular Structure, VI. Constants of Diatomic Molecules," Van Nostrand Reinhold Co. (1979).

Table 1. Correlations between  $\Lambda$ - $\Sigma$  states and  $\omega$ - $\Omega$  (case (c)) states from  $2P_{3/2}$ ,  $2P_{1/2}$  states coupled to a  $1S_0$  state.

$\Lambda$ - $\Sigma$ coupling	Case (c)	Atomic limits
$A^2\Sigma_u^+$	$A^2\Sigma_{1/2u}^+$ 1/2u I	} $np^5 2P_{3/2} + 1S_0$
$B^2\Pi_g$	$B^2\Pi_{3/2g}$ 3/2g	
	$B^2\Pi_{1/2g}$ 1/2g I	
$C^2\Pi_u$	$C^2\Pi_{3/2u}$ 3/2u	
	$C^2\Pi_{1/2u}$ 1/2u II	} $np^5 2P_{1/2} + 1S_0$
$D^2\Sigma_g^+$	$D^2\Sigma_{1/2g}^+$ 1/2g II	

Table 2. Coefficients of the two configurations in the  $1/2u$  I and  $1/2u$  II states evaluated for the reduced potential ( $D_e^0 = 1.39$  eV,  $T^0 = 3.0$  eV) at  $R_e$ .

	$C_1$	$C_2$	$D_e$ (eV)	$T$ (eV)	$1/2 \zeta$
	$1/2u$ I = $C_1(C^2\Pi_u) + C_2(A^2\Sigma_u^+)$				
	$1/2u$ II = $C_2(C^2\Pi_u) - C_1(A^2\Sigma_u^+)$				
$Ne_2^+$	0.006	0.9999	1.36	3.03	-0.0324
$Ar_2^+$	0.014	0.9998	1.33	2.94	-0.0592
$Kr_2^+$	0.066	0.997	1.19	2.80	-0.2220
$Xe_2^+$	0.125	0.992	1.03	2.64	-0.4356

Table 3. The ion induced dipole potential evaluated at  $R_e$  of the van der Waals dimer.

Molecular Ion	Polarizability <sup>a</sup> $\alpha(A^3)$	$R_e(A)$ <sup>b</sup>	$-\alpha/2R^4$ (eV)	Vertical <sup>c</sup> IP of 1/2u I (eV)		E( $R_e$ ) <sup>d</sup> of 1/2u I (eV)		Adiabatic <sup>e</sup> IP of (eV)		D <sub>0</sub> <sup>f</sup> 1/2u II (eV)	
He <sub>2</sub> <sup>+</sup>	0.2051	2.96	-0.019	--	--	--	--	--	--	--	--
Ne <sub>2</sub> <sup>+</sup>	0.395	3.03	-0.034	--	--	--	--	--	--	--	--
Ar <sub>2</sub> <sup>+</sup>	1.64	3.761	-0.059	15.55	0.025	-0.227	0.025	15.85	0.015	0.10	0.015
Kr <sub>2</sub> <sup>+</sup>	2.48	4.007	-0.069	13.76	0.03	-0.257	0.2	14.54	0.015	0.14	0.015
Xe <sub>2</sub> <sup>+</sup>	4.04	4.361	-0.080	11.85	0.015	-0.304	0.015	13.27	0.015	0.19	0.015

94

<sup>a</sup>Atomic polarizabilities from index of refraction measurements, A. Dalgarno and A. E. Kingston, Proc. Roy. Soc. (London) A259, 424 (1961).

<sup>b</sup>Equilibrium internuclear distance of van der Waals dimers Ref. 25 and 28.

<sup>c</sup>Vertical ionization potentials from Ref. 34.

<sup>d</sup>Potential energy of the 1/2u I state at  $R_e$ , with respect to the  $2P_{3/2}$  ionic state by  $E(R_e) = IP(2P_{3/2}) + D_0(R_e)_2 - VIP(1/2u I)$  where  $IP(2P_{3/2})$  is the ionic ionization potential,  $D_0(R_e)_2$  is the rare gas van der Waals binding energy (Ref. 25 and 28) and  $VIP(1/2u I)$  is the vertical ionization potential of Ref. 34.

<sup>e</sup>Adiabatic ionization potentials of Ref. 34.

<sup>f</sup>The dissociation energy of the 1/2u II state (Ref. 34).

Table 4. Rydberg states resulting from coupling the four lowest ionic cores with a UA Rydberg orbital.

Ionic Core	UA Orbital	$\Lambda - \Sigma$	$(\Omega_c, \omega)$
$A^2\Sigma_u^+$	$ms\sigma_g$	$1,3\Sigma_u^+$	$0u, 0u, 1u$
$B^2\Pi_g$	$ms\sigma_g$	$1,3\Pi_g$	$0g, 0g, (2)1g, 2g$
$C^2\Pi_u$	$ms\sigma_g$	$1,3\Pi_u$	$0u, 0u, (2)1u, 2u$
$D^2\Sigma_g^+$	$ms\sigma_g$	$1,3\Sigma_g^+$	$0g, 0g, 1g$
$A^2\Sigma_u^+$	$mp\sigma_u$	$1,3\Sigma_g^+$	$0g, 0g, 1g$
$B^2\Pi_g$	$mp\pi_u$	$1,3\Pi_g$	$0g, 0g, (2)1g, 2g$
	$mp\sigma_u$	$1,3\Pi_u$	$0u, 0u, (2)1u, 2u$
$C^2\Pi_u$	$mp\pi_u$	$1,3\Sigma_u^\pm, 1,3\Delta_u$	$(2)0u, (2)0u, (2)1u, (2)2u, 3u$
	$mp\sigma_u$	$1,3\Pi_g$	$0g, 0g, (2)1g, 2g$
$D^2\Sigma_g^+$	$mp\pi_u$	$1,3\Sigma_g^\pm, 1,3\Delta_g$	$(2)0g, (2)0g, (3)1g, (2)2g, 3g$
	$mp\sigma_u$	$1,3\Sigma_u^+$	$0u, 0u, 1u$
	$mp\pi_u$	$1,3\Pi_u$	$0u, 0u, (2)1u, 2u$

Table 4. (continued)

Ionic Core	VA Orbital	$\Lambda - \Sigma$	$(\Omega_c, \omega)$
$A^2\Sigma_u^+$	$md\sigma_g$	$1,3 \Sigma_g^+$	$0u, 0u, 1u$
	$md\pi_g$	$1,3 \Pi_u$	$0u, 0u, (2)1u, 2u$
	$md\delta_g$	$1,3 \Delta_u$	$1u, (2)2u, 3u$
$B^2\Pi_g$	$md\sigma_g$	$1,3 \Pi_g$	$0g, 0g, (2)1g, 2g$
	$md\pi_g$	$1,3 \Sigma_g^{\pm}, 1,3 \Delta_g$	$(2)0g, (2)0g, (3)1g, (2)2g, 3g$
	$md\delta_g$	$1,3 \Pi_g, 1,3 \Phi_g$	$0g, 0g, (2)1g, 2g, 3g, (2)4g, 5g$
$C^2\Pi_u$	$md\sigma_g$	$1,3 \Pi_u$	$0u, 0u, (2)1u, 2u$
	$md\pi_g$	$1,3 \Sigma_u^{\pm}, 1,3 \Delta_u$	$(2)0u, (2)0u, (3)1u, (2)2u, 3u$
	$md\delta_g$	$1,3 \Pi_u, 1,3 \Phi_u$	$0u, 0u, (2)1u, 2u, 3u, (2)4u, 5u$
$D^2\Sigma_g^+$	$md\sigma_g$	$1,3 \Sigma_g^+$	$0g, 0g, 1g$
	$md\pi_g$	$1,3 \Pi_g$	$0g, 0g, (2)1g, 2g$
	$md\delta_g$	$1,3 \Delta_g$	$1g, (2)2g, 3g$

Table 5. Rydberg states resulting from coupling a  $1s_0$  rare gas atom with an excited atom in atomic Rydberg states corresponding to configurations  $np^5n's$ ,  $np^5n'p$ ,  $np^5n'd$ . The atomic states in each of these configurations are ordered in increasing energy as they occur for Ne,  $n' = 3$ .

<u><math>np^5n's</math></u>		
$^2P_{3/2}n's$	$s[3/2]_2$	$\bar{0}g,u, 1g,u, 2g,u$
	$s[3/2]_1$	$+0g,u, 1g,u$
$^2P_{1/2}n's$	$s'[1/2]_0$	$\bar{0}g,u$
	$s'[1/2]_1$	$+0g,u, 1g,u$
<hr/>		
<u><math>np^5n'p</math></u>		
$^2P_{3/2}n'p$	$p[1/2]_1$	$\bar{0}g,u, 1g,u$
	$p[5/2]_3$	$\bar{0}g,u, 1g,u, 2g,u, 3g,u$
	$p[5/2]_2$	$+0g,u, 1g,u, 2g,u$
	$p[3/2]_1$	$\bar{0}g,u, 1g,u$
	$p[3/2]_2$	$+0g,u, 1g,u, 2g,u$
$^2P_{1/2}n'p$	$p'[3/2]_1$	$\bar{0}g,u, 1g,u$
	$p'[3/2]_2$	$+0g,u, 1g,u, 2g,u$
$^2P_{3/2}n'p$	$p[1/2]_0$	$+0g,u$
$^2P_{1/2}n'p$	$p'[1/2]_1$	$\bar{0}g,u, 1g,u$
	$p'[1/2]_0$	$+0g,u$
<hr/>		



Table 5. (continued).

---

$\underline{np}^5 n'd$		
${}^2P_{3/2} n'd$	$d[1/2]_0$	$-$ $0g,u$
	$d[1/2]_1$	$+$ $0g,u, 1g,u$
	$d[7/2]_4$	$-$ $0g,u, 1g,u, 2g,u, 3g,u, 4g,u$
	$d[7/2]_3$	$+$ $0u,g, 1u,g, 2u,g, 3u,g$
	$d[3/2]_2$	$-$ $0u,g, 1u,g, 2u,g$
	$d[3/2]_1$	$+$ $0u,g, 1u,g$
	$d[5/2]_2$	$-$ $0u,g, 1u,g, 2u,g$
	$d[5/2]_3$	$+$ $0u,g, 1u,g, 2u,g, 3u,g$
${}^2P_{1/2} n'd$	$d'[5/2]_3$	$-$ $0u,g, 1u,g, 2u,g$
	$d'[5/2]_3$	$+$ $0u,g, 1u,g, 2u,g, 3u,g$
	$d'[3/2]_2$	$-$ $0g,u, 1g,u, 2g,u$
	$d'[3/2]_1$	$+$ $0g,u, 1g,u$

---

Figure Captions: Chapter II

- Fig. 1.** Cross-sectional view of supersonic molecular beam photoionization mass spectrometer used at SSRL. The photon beam is coming out of the plane of the paper. 1. Beam source differential pumping wall; 2. Outer dewar and heat shield; 3. Inner dewar; 4. Nozzle; 5. Skimmer; 6. Ion extraction field lens; 7. Focussing lenses; 8. Quadrupole mass filter; 9. Spiraltron ion detector; and 10. Gas catch.
- Fig. 2.** The photon flux as a function of wavelength on the  $8^{\circ}$  (I-2) line at SSRL after passing through a 1500 Å thick Al/Si window and a 1200 lines/mm Osmium coated gating blazed at 540 Å, measured, using a sodium salicylate VUV to visible converter and a RCA 8850 photomultiplier tube calibrated with a NBS photodiode at 584 Å, on May 8, 1980 during dedicated operation of SPEAR with a stored electron beam current of 42 mA.
- Fig. 3.** Photoionization efficiency of  $\text{Ne}_2$  measured with a photon resolution of 2.5 Å FWHM.
- Fig. 4.** Photoionization efficiency of  $\text{Ne}_2$  measured with a photon resolution of 0.8 Å FWHM. Plotted, in the upper portion, are the energies of the dipole allowed atomic transitions for Ne.
- Fig. 5.** The photoion yield of  $\text{He}_2^+$  from a 700 torr, 4.2 K He beam, measured with a photon resolution of 0.8 Å FWHM. Also plotted are the energies of the dipole allowed atomic transitions for He.

Fig. 6. In part (a) the dissociation energies,  $D_e$ , of the  $1/2u$  I' states of the diatomic rare-gas molecular ions,  $Ne_2^+$ ,  $Ar_2^+$ ,  $Kr_2^+$  and  $Xe_2^+$  are plotted versus the spin-orbit splitting of the respective atomic ionic states,  $\zeta$ . Similarly, part (b) is a plot of the energies of the  $1/2u$  II state. The solid lines are the predictions of the model described in the text.

Fig. 7. Schematic molecular potential energy curves of  $Ne_2$ ,  $Ne_2^+$  (in the region of the  $6s$  Rydberg states) and  $Ne_2^+$ .

Fig. 8. Correlation diagram for the  $5p$  Rydberg states. The atomic limits are on the left-hand side while the UA states are on the right.

Fig. 9. A correlation diagram for the  $0u^+$ ,  $1u$  molecular Rydberg states of  $p^5np$  type. The dissociation products are on the left and the UA states on the right.

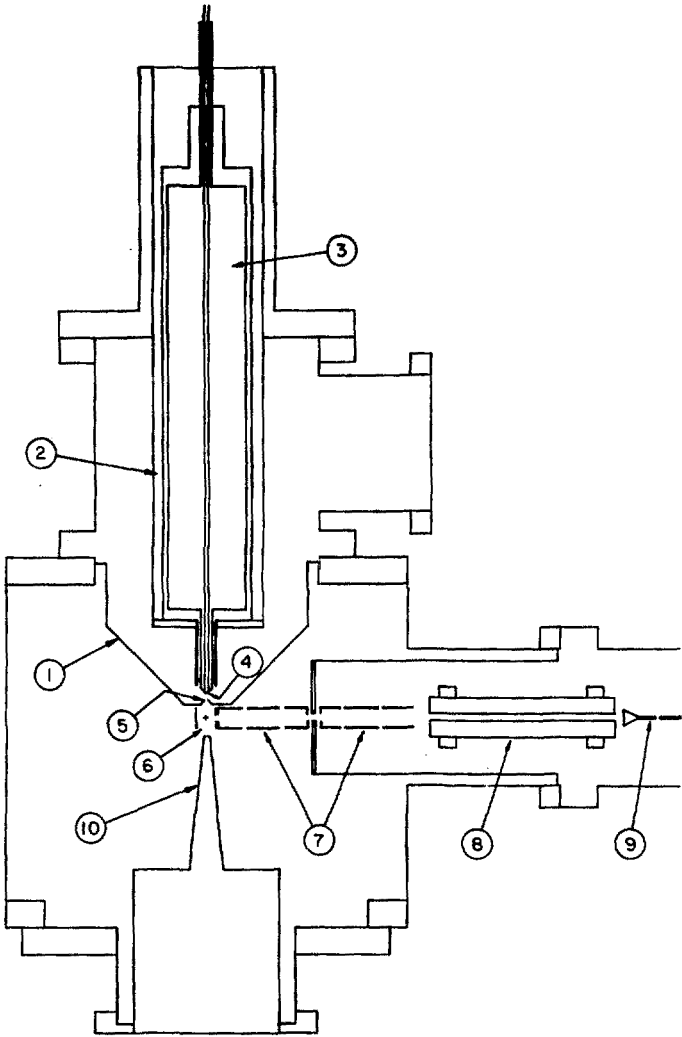
Fig. 10. A correlation diagram for the  $0u^+$ ,  $1u$  molecular Rydberg states of  $p^5nd$  type. The states in the atomic limits are listed on the left while the UA states are listed on the right.

Fig. 11. Schematic of potential energy curves of the different types of states that are important in the rare-gas systems, for different autoionization mechanisms. a) Vibrational Autoionization: allowed states in the vertical transition region produce highly excited molecular ions. b) Electronic autoionization from Rydberg states with a different core than the ionic state. Good vibrational wavefunction overlap can be obtained even near the adiabatic ionization potential.

c) autoionization from locally bound and repulsive Rydberg states.

**Fig. 12.** The photoionization efficiency of  $\text{Ne}_2$  at 0.8 Å FWHM in the region, near threshold, of the sharp autoionization structure. The insert near the top shows the absorption spectra of Ref. 8 on the same wavelength scale. Note the intensity of the states in System X, shown in this figure, have been amplified by a factor of 14. The atomic transitions are indicated by lines drawn beneath the data at the appropriate wavelengths.

**Fig. 13.** The photoionization efficiency of  $\text{Xe}_2$ ,  $\text{Kr}_2$  and  $\text{Ar}_2$  obtained in this laboratory (Ref. 4 and 5) plotted as a function energy in  $\text{cm}^{-1}$ . The energies of the allowed atomic transitions are shown above each of the experimental curves.



XRL 809-11811

Fig. 1.

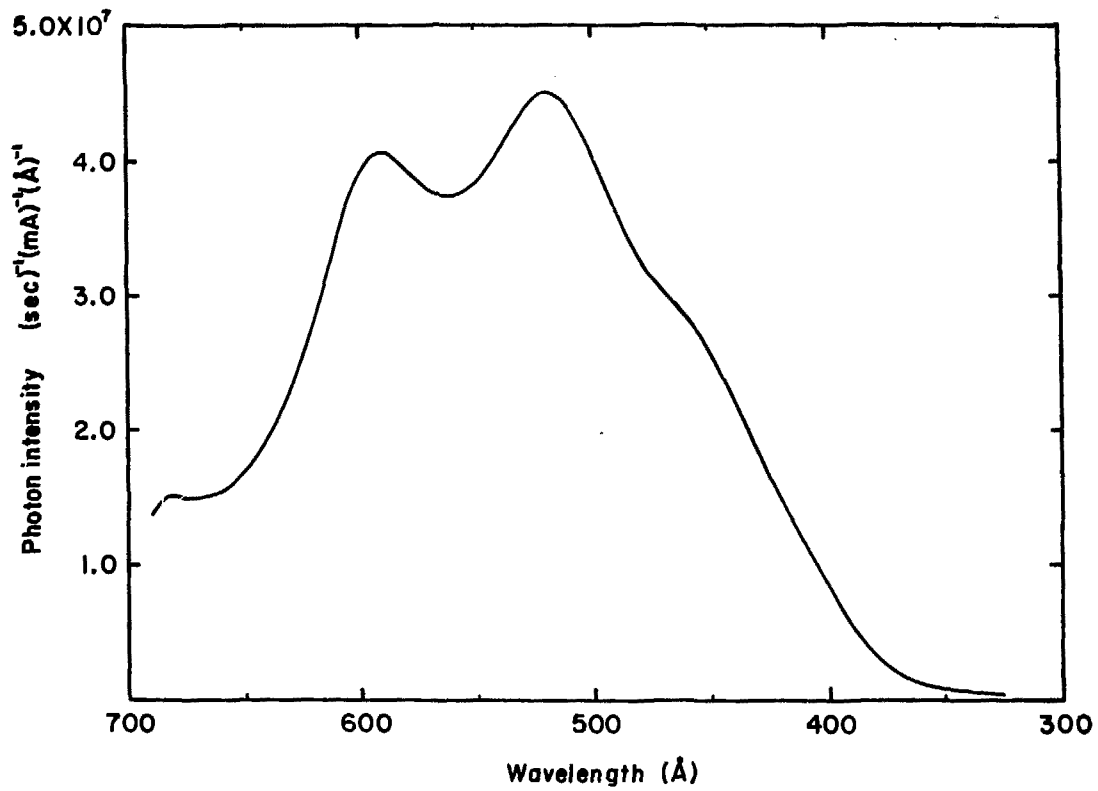
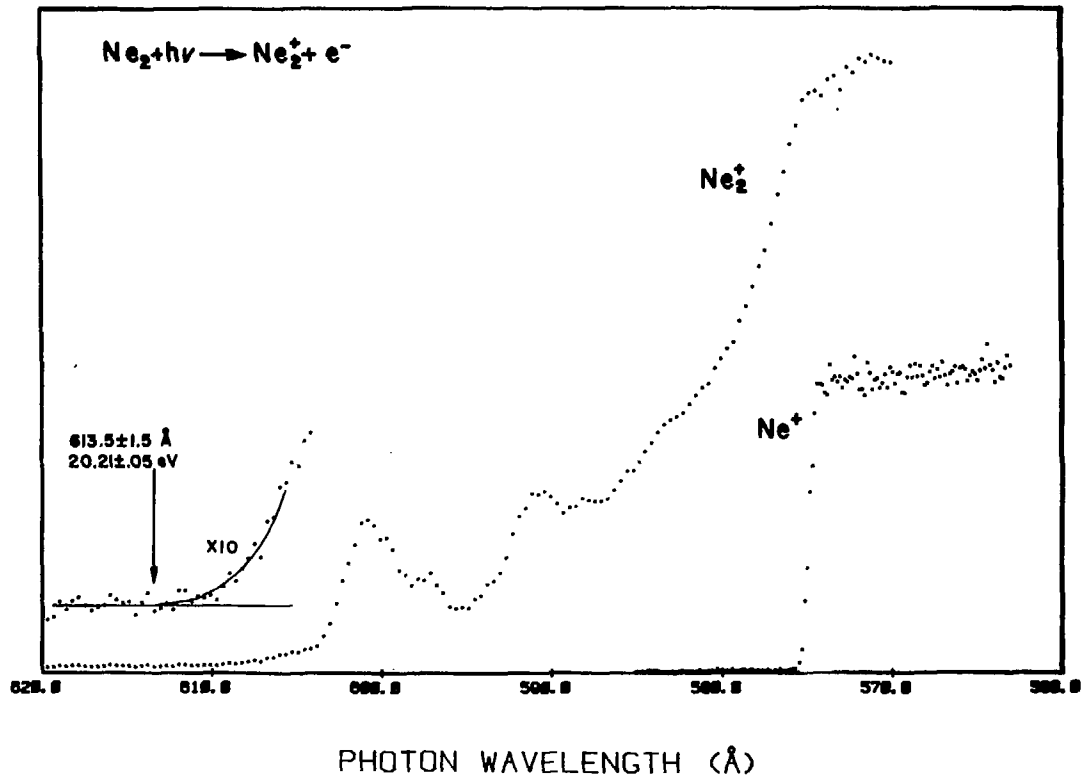


Fig. 2.

XBL 809-11808

PHOTOIONIZATION EFFICIENCY



XBL 806-9896

Fig. 3.

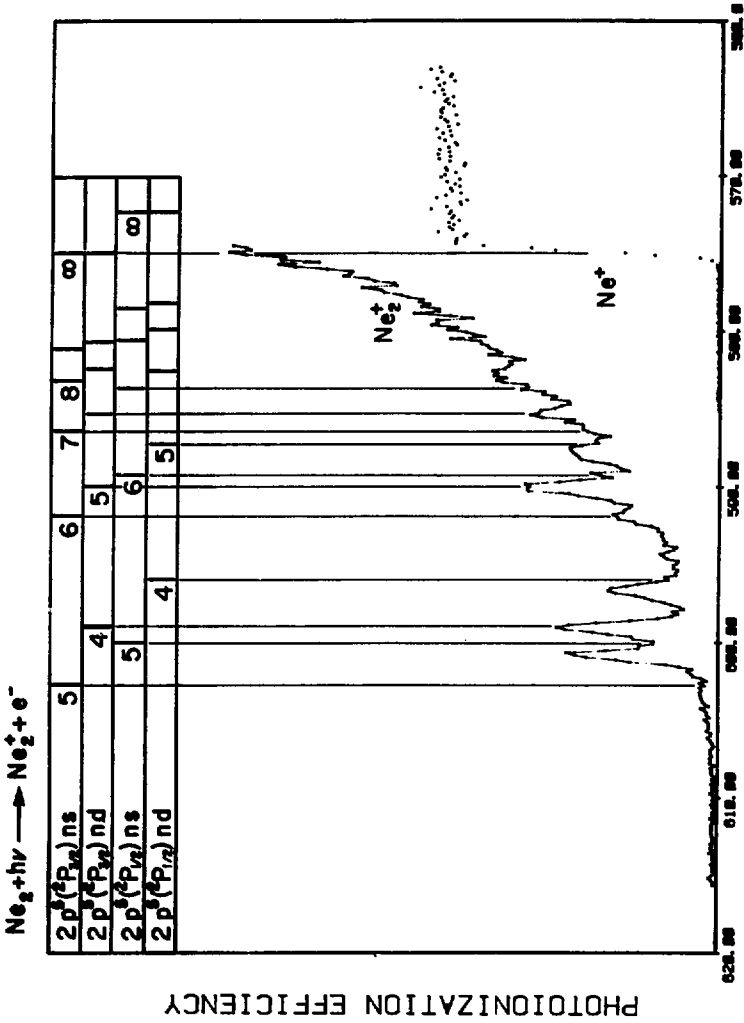


Fig. 4.

XBL 806-9891



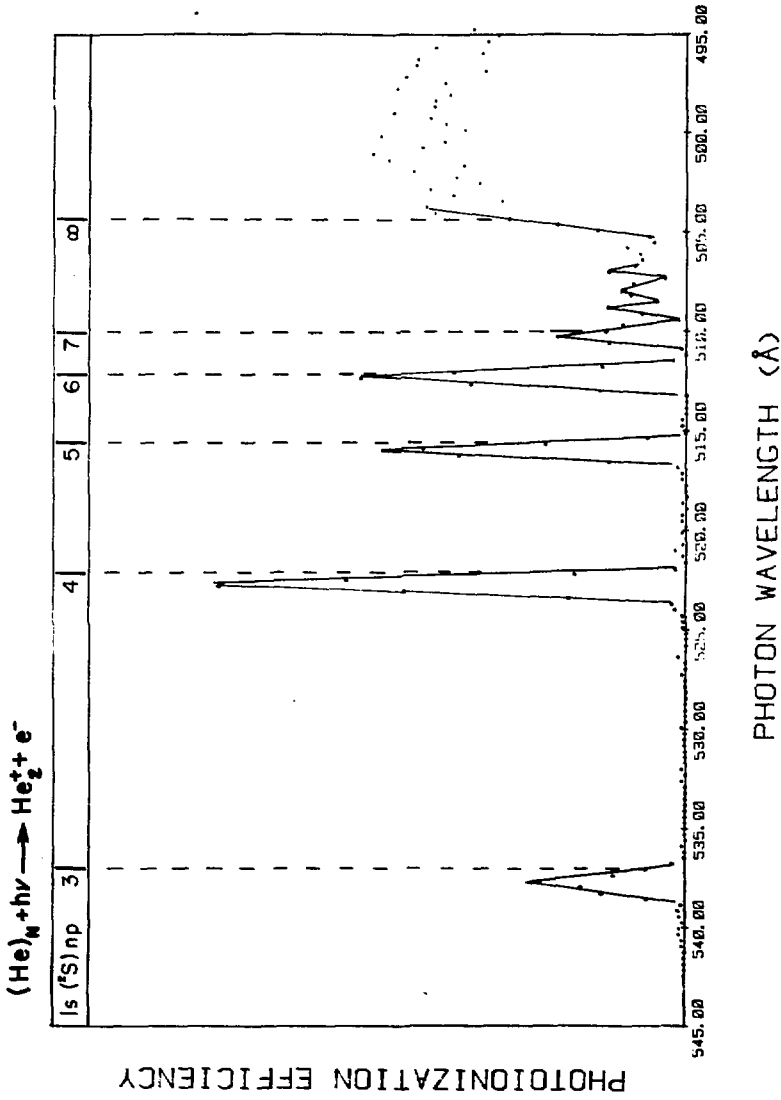
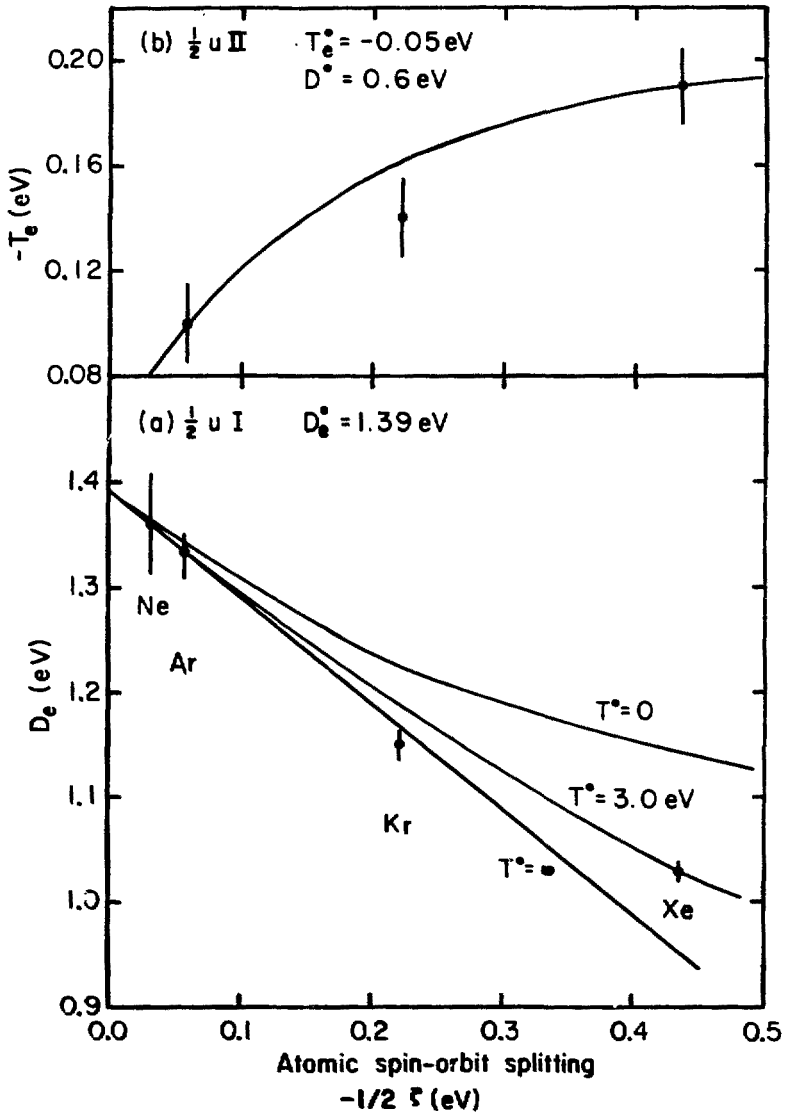


FIG. 5.

XBL 809-11805



XBL 809-11809

Fig. 6.

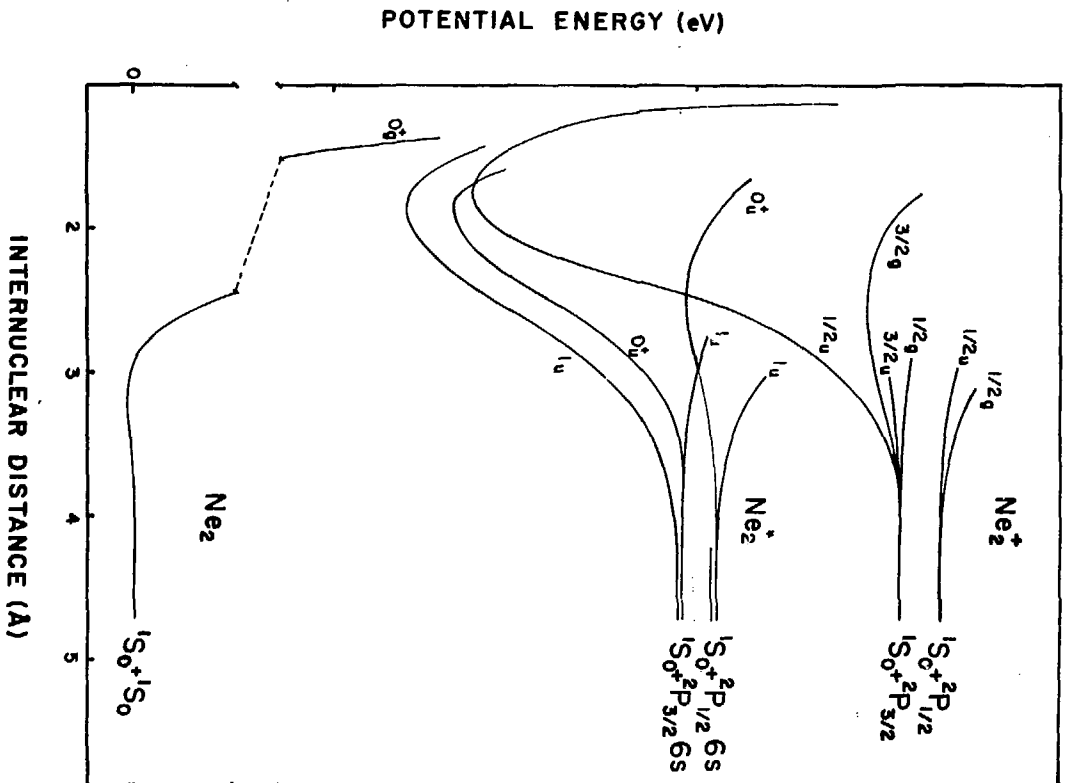
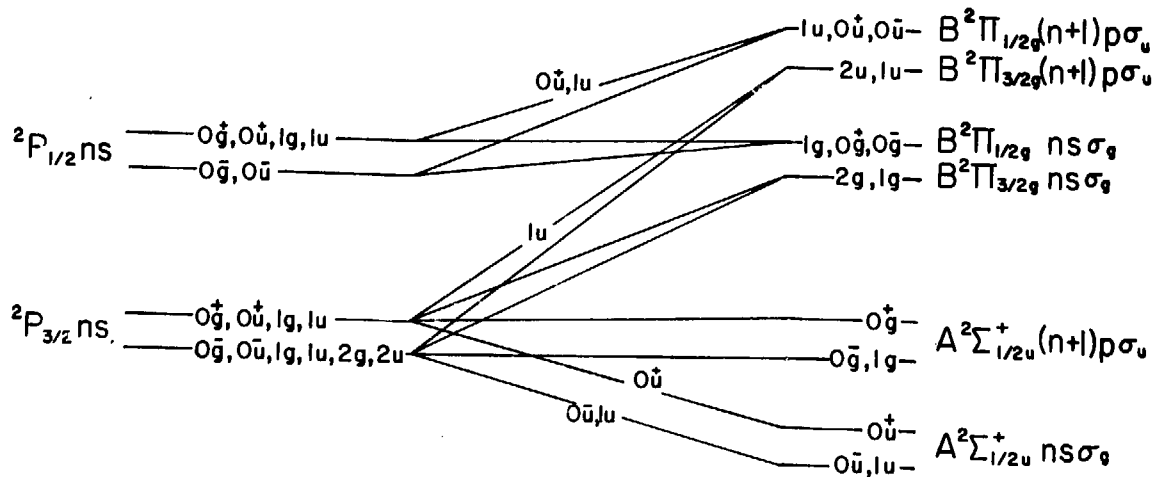


Fig. 7.

XBL 809-11810



21

Fig. 8.

XBL 809-11859

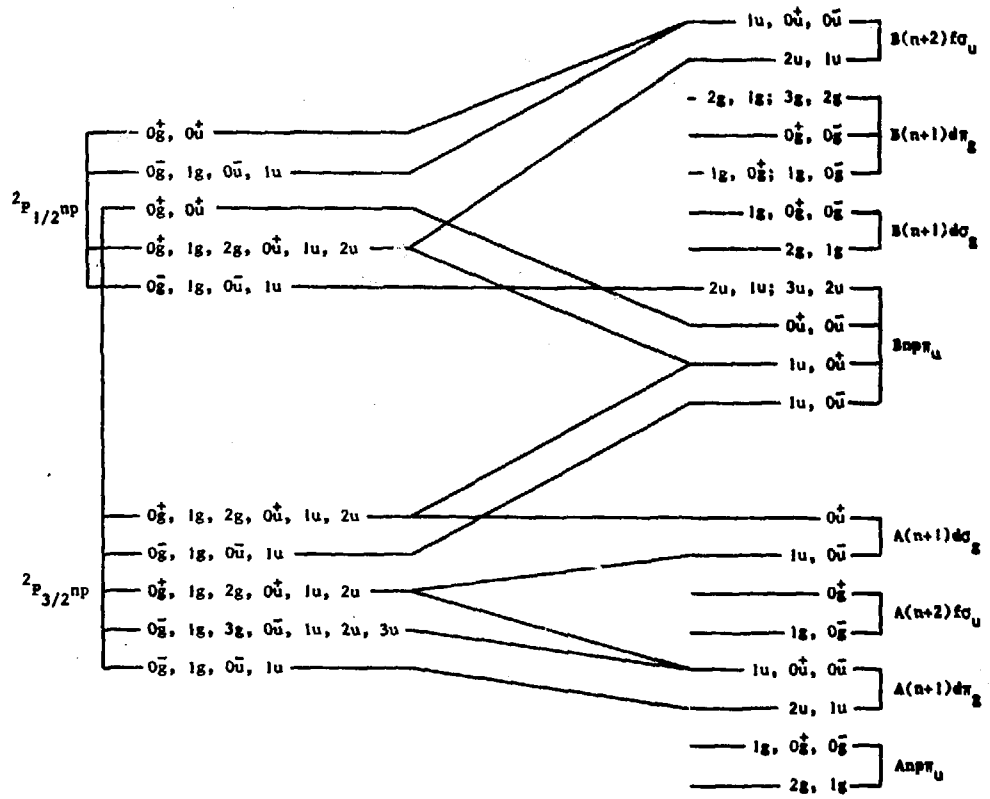
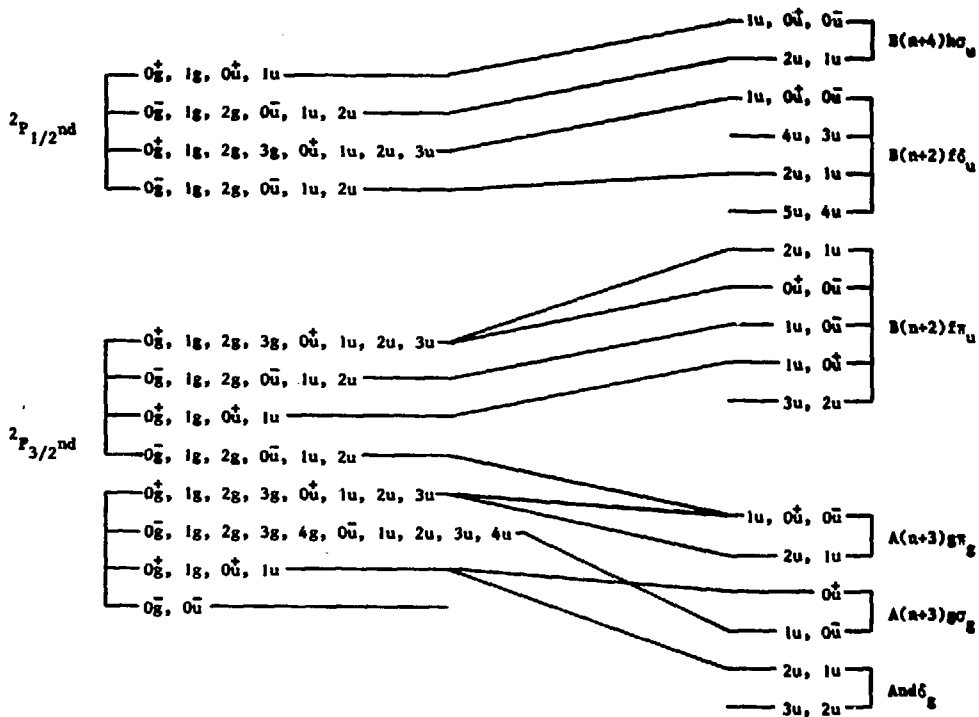


Fig. 9.

XBL 809-11875



63

XBL 809-11874

Fig. 10

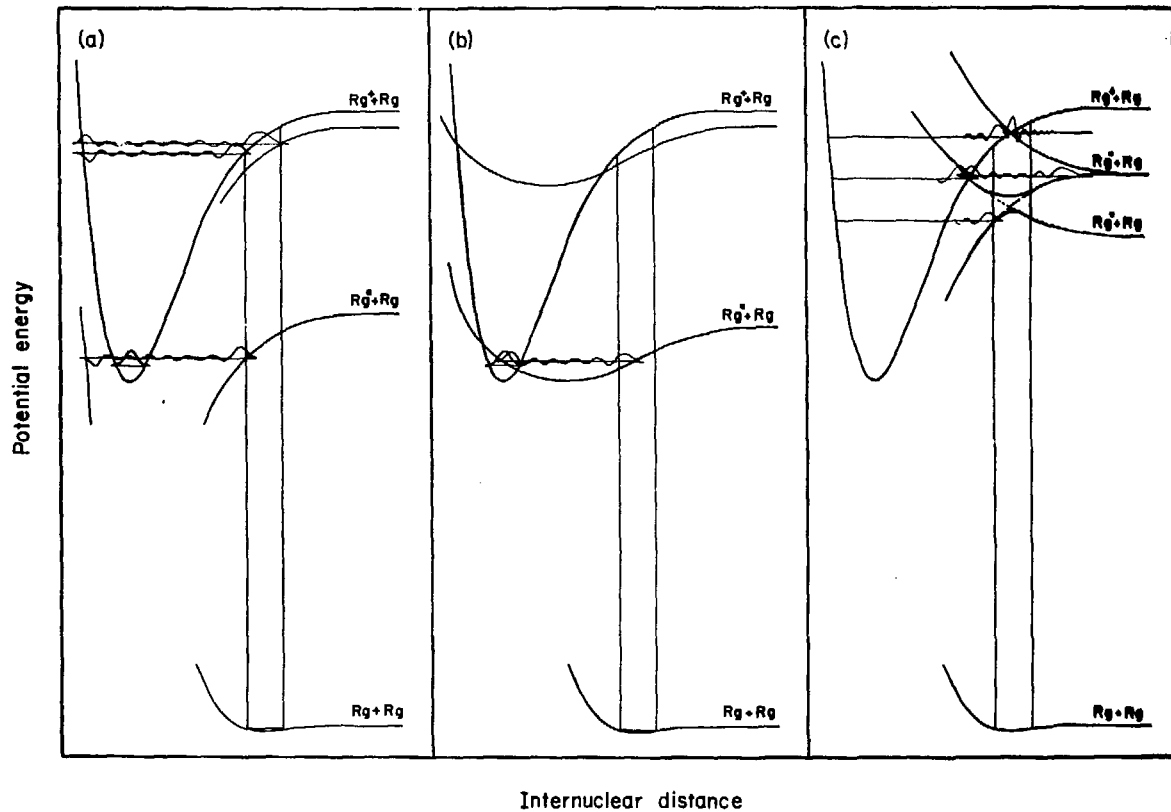


Fig. 11.

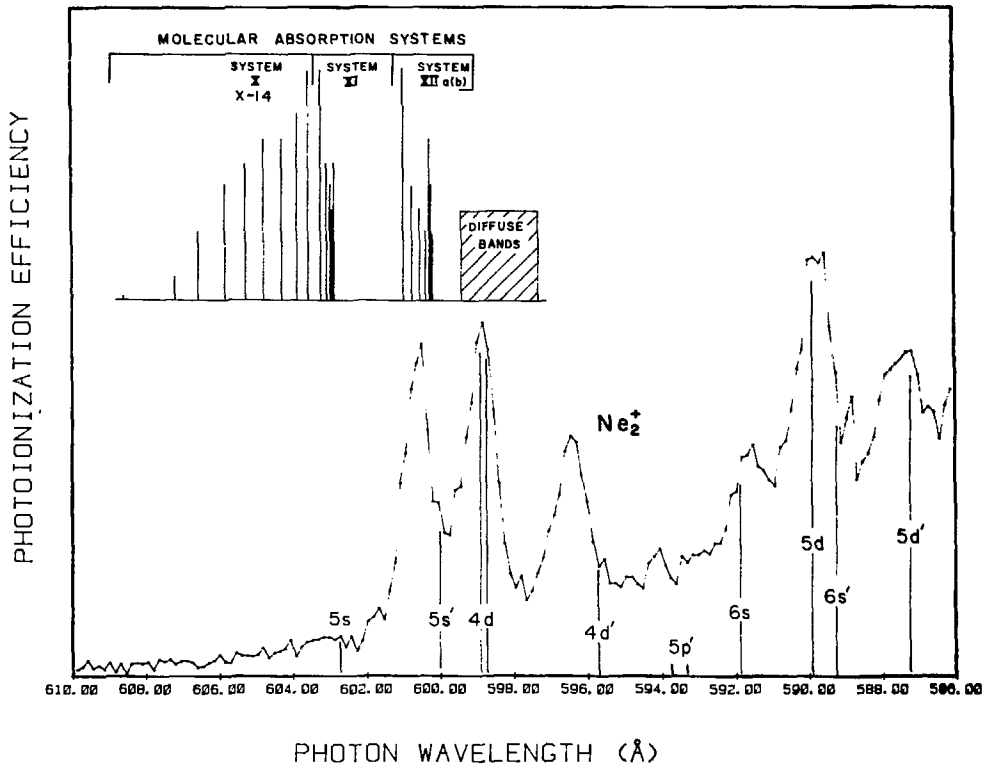
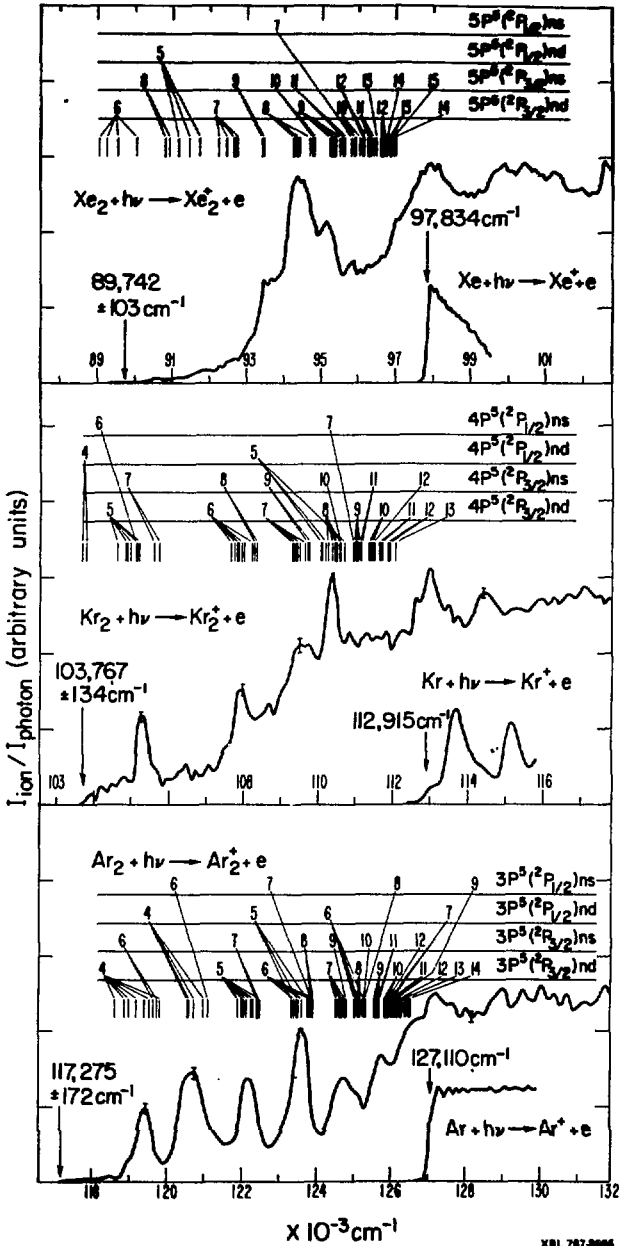


Fig. 12.

XBL 809-11804





XBL 707-8006

Fig. 13.

## CHAPTER III

## PHOTOIONIZATION MASS SPECTRA OF A FEW MOLECULES AND CLUSTERS

A. Introduction

Besides the rare gas systems, the photoionization mass spectra of  $O_3$ ,  $NH_3$ ,  $H_2O$ ,  $(H_2O)_2$ ,  $N_2$ ,  $(N_2)_2$ ,  $CO$ ,  $(CO)_2$  and  $H_2$  in supersonic molecular beams have been recorded. These studies will be grouped into four categories: a)  $O_3$  and  $NH_3$ ; b)  $H_2O$ ,  $(H_2O)_2$ ; c)  $N_2$ ,  $CO$  and  $H_2$ ; and d)  $(N_2)_2$  and  $(CO)_2$ . The photoion yield spectra obtained of  $O_3^+$  and  $NH_3^+$  demonstrate the improved resolution due to the rotational cooling of molecules in a supersonic expansion. The second group,  $H_2O$  and  $(H_2O)_2$ , was studied to test the viability of using this technique to determine absolute proton affinities by measuring the threshold for photodissociative ionization of a hydrogen bonded system. These measurements were made possible by excess clusters present in the supersonic molecular beam. The photoionization mass spectra of  $N_2$ ,  $CO$  and  $H_2$  (the third category) were measured at photon energies above those which are available with conventional laboratory sources by using the synchrotron radiation available at SSRL. The objective of these studies was to examine the threshold and mechanism for the dissociative ionization process producing  $N^+$  from  $N_2$ ,  $C^+$  from  $CO$  and energetic  $H^+$  from  $H_2$ . And in the final category,  $(N_2)_2$  and  $(CO)_2$  were studied using synchrotron radiation to determine the heat of formation of  $N_3^+$  and  $C_2O^+$ .

### B. Photoionization Mass Spectroscopy of NH<sub>3</sub> and O<sub>3</sub>

When used as a source in a photoionization mass spectrometer, a supersonically expanded molecular beam enables accurate determination of ionization potentials as well as ionic state vibrational frequencies. Conventional PI studies use gas cells or effusive beams as sources. The photon energy resolution employed, limited by the photon source intensity, has usually been better than 0.010 eV ( $80 \text{ cm}^{-1}$ ) but is rarely sufficient to resolve rotational states. The energy in the rotational degrees of freedom,  $3/2 kT$  equal to 0.026 eV ( $200 \text{ cm}^{-1}$ ) at room temperature, thus limits the effective resolution. A rotational temperature of less than 10 K can readily be obtained in a supersonically expanded molecular beam. This low rotational temperature eliminates rotational broadening, permitting the experiments to benefit fully from the available, instrumental photon resolution.

The method used in these studies combined photoionization mass spectroscopy with supersonic molecular beam technology. The details of the apparatus used have been described previously.<sup>1</sup> The major components were a gas discharge vacuum ultraviolet light source and monochromator, a double differentially pumped modulated supersonic molecular beam source, a quadrupole mass filter with a Daly type ion detector, and single pulse counting electronics. The experiment was performed by crossing the monochromatic VUV light with the molecular beam which was modulated at 150 Hz. The light source used for these studies was the hydrogen many-line pseudo-continuum. This light was dispersed by a 1200 lines/mm Al/MgF<sub>2</sub> grating blazed at 1200 Å, which was used in a one-meter normal-incidence monochromator. The ions produced in the interaction region

were extracted and focused onto the entrance of the quadrupole mass filter, which was perpendicular to the plane of the molecular beam and incident photons. The ion yield was then measured as a function of the incident photon energy. The energy resolution for this technique was limited by the chosen band pass of the monochromator, 0.8 Å FWHM in this case, and shows no sign of rotational broadening.

The photoionization efficiency for ammonia expanded through a 0.13 mm diameter orifice at 100 torr is shown in Fig. 1. The first ionization potential is determined to be  $10.176 \pm 0.010$  eV. The step-like structure in the photoyield is characteristic of the direct ionization process to excited vibrational states of the ion. The vibrational frequency of  $950 \pm 32$  cm<sup>-1</sup> is assigned to the out-of-plane bending mode of the ion, NH<sub>3</sub><sup>+</sup>. The neutral species, NH<sub>3</sub>, is pyramidal while its ion is believed to be planar.<sup>2</sup> This large change in geometry implies a gradual rise in the photoionization efficiency near threshold which, indeed, is observed. These results are in excellent agreement with previous studies of ammonia as shown in Table 1.

The sharp resonance-like structure is indicative of excitation to autoionizing states. This feature, which is predominant in these measurements, was not observed in a previous investigation due to rotational broadening, which was three times greater than the photon resolution employed.<sup>3</sup> A recent measurement with six times greater photon resolution (0.14 Å FWHM) than used here only begins to show the structure which is resolved in Fig. 1. Further improvement in the photon resolution and the use of a true continuum light source is necessary before assignment of these autoionizing states can be made.

The photoionization efficiency of ozone expanded through a 0.15 mm-diameter nozzle at a partial pressure of approximately 10 torr in 250 torr Ar is shown in Fig. 2. The adiabatic ionization potential determined from this study is  $12.523 \pm 0.010$  eV. The distinctive step-like structure is indicative of ionization to successively higher vibrational levels of the ion. The average spacing of these steps is  $620 \pm 40$   $\text{cm}^{-1}$ , which is in excellent agreement with the previous studies given in Table 2. This vibrational progression is assigned to the  $\nu_2$  bending mode, which is  $705$   $\text{cm}^{-1}$  in the ground molecular state.<sup>5</sup> In addition, on each of these steps there are much weaker onsets in the yield curve. These could be evidence of an additional vibrational progression, a higher-lying ionic state, or most likely, unresolved autoionization structure. At higher photon energies the steps become more diffuse, due to decreasing Franck-Condon factors, additional ionic states, and unresolved autoionization structure.

### C. Proton Affinity of $\text{H}_2\text{O}$

#### 1. Introduction

Proton transfer represents one of the fastest and most important classes of reactions in both the gas and condensed phases. When proton transfer between two molecules is exothermic, it is usually the dominant reaction. The equilibrium  $\text{M}_1\text{H}^+ + \text{M}_2 \rightleftharpoons \text{M}_1 + \text{M}_2\text{H}^+$  will be displaced to the side of the molecule with the higher proton affinity. Relative values of proton affinities can easily be obtained by measurements of  $[\text{M}_1\text{H}^+]/[\text{M}_2\text{H}^+]$ , and  $[\text{M}_1]/[\text{M}_2]$  when the system is at equilibrium in the ion source of a mass spectrometer. This will give the equilibrium constant and therefore  $\Delta G^\circ$  of the reaction. Since  $\Delta S^\circ$  for the proton

transfer reaction is usually very small, the relative proton affinity or the enthalpy change for transfer of a proton from one entity to another can be derived.<sup>6</sup> However, in order to translate these measurements into absolute proton affinities, there is a need for accurate absolute proton affinities of a few reference compounds. Usually absolute values of proton affinities are obtainable from appearance potential measurements of  $MH^+$  in a mass spectrometer, low energy ion-neutral scattering cross section measurements, collision induced dissociation, crystal lattice energy determinations, or NMR experiments.

The fine control of photon energy makes the photoionization mass spectrometric method one of the most accurate means for the determination of the proton affinity of M from the appearance potential measurements of  $MH^+$  from a suitable parent molecule. Nevertheless, the major drawbacks of the photoionization technique in finding the proton affinity of a molecule are the low fluxes of monochromatic vacuum ultraviolet photons available from laboratory discharge light sources and the possible lack of suitable parent molecules to produce  $MH^+$ . Recent developments in molecular beam photoionization mass spectrometry,<sup>7</sup> involving careful optimization of relatively high intensity light sources, a sensitive mass spectrometer, and an intense molecular beam production system, have allowed the photoionization study of dimers<sup>8,9</sup> synthesized in supersonic expansions. Polyatomic dimers are excellent parent molecules for the photoionization production of those  $MH^+$  ions which cannot be obtained from other stable molecules.

The photoionization efficiencies of  $(H_2O)_2$  was measured to illustrate this new method for the determination of proton affinities.

## 2. Results and Discussion

The apparatus and procedures were essentially the same as previously described.<sup>7-9</sup> The light source used was the hydrogen many-line pseudo-continuum. The spectrometer grating was  $\text{MgF}_2$ - or gold-coated, ruled with 1200 lines/mm, having a reciprocal dispersion of 8.3 Å/mm. The  $\text{H}_2\text{O}$  molecular beam was produced by seeding water vapor at 89°C in 150 torr of Ar and then expanding through a 0.15 mm-diameter Pyrex nozzle. These beam conditions used to study the dimer produced a minimum of higher clusters.

The photoionization efficiency curves of  $(\text{H}_2\text{O})_2^+$  and  $\text{H}_2\text{O}^+$  as well as the ion yield of  $\text{H}_3\text{O}^+$  in the spectral range from 950 Å to 1100 Å were measured with a photon band width of 2.5 Å FWHM. These results are shown in Fig. 3. Due to the low signal for  $(\text{H}_2\text{O})_2^+$  ion no distinct threshold was observed. At  $11.21 \pm 0.09$  eV the signal decreased below the detection limit in this apparatus of 0.1 count/sec. The photoionization efficiency increases gradually above threshold without prominent features until at 1057 Å a very sharp break occurs. The ion yield of  $\text{H}_3\text{O}^+$  starts at  $1057 \pm 2.5$  Å ( $11.73 \pm 0.03$  eV) and increases constantly with no resolved structure. The coincidence between the break in the  $(\text{H}_2\text{O})_2^+$  signal and of  $\text{H}_3\text{O}^+$  ion strongly suggests that the observed  $\text{H}_3\text{O}^+$  signal is from photodissociative ionization of the dimer and not from the less abundant higher clusters. Neutral OH and not  $\text{OH}^-$  is the expected second product in this dissociative photoionization, based on the fact that  $\text{H}_2\text{O}$  does not photodissociate via an ion pair channel in this energy range.

Also shown in Fig. 3 is the photoionization yield of  $\text{H}_2\text{O}^+$  measured using the same beam conditions and photon resolution. The adiabatic ionization potential,  $12.601 \pm 0.016$  eV, obtained from the threshold of  $\text{H}_2\text{O}^+$  production, is in excellent agreement with previous measurements.<sup>10,11</sup> The sharp threshold indicates large Franck-Condon factors for the adiabatic transition. The highest occupied molecular orbital in  $\text{H}_2\text{O}$  is the oxygen lone pair. Therefore, the lowest ionic state has essentially the same geometry as the ground state. The stair-step shape of the efficiency is characteristic of direct ionization to higher vibrational levels. The spacing of these steps is in agreement with reported photoelectron spectra.<sup>12</sup> These assignments are shown in Fig. 3. On each of these steps, several partially resolved peaks appear in the ion yield. This structure is characteristic of autoionization. A recently reported photoionization spectrum using a gas cell with a photon resolution of 0.14 Å FWHM<sup>13</sup> (18 times higher than the 2.5 Å FWHM used here) barely begins to resolve this structure. This contrast is solely due to the high degree of rotational cooling in the supersonic expansion.

The stability of water dimer is attributed to a single hydrogen bond involving only the oxygen lone pair on one of the constituent water molecules. The molecular beam microwave resonance structure<sup>14</sup> indicates almost independent motion of the hydrogens not involved in the bond between the two  $\text{H}_2\text{O}$  species. Thus the photoionization of the dimer might be expected to be quite similar to the monomer. However, in forming the hydrogen bond the partial negative charge on the donor oxygen (lone pair) is increased, reducing its binding energy (shift in



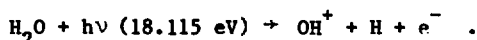
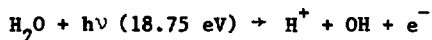
Koopman's theorem ionization potential between dimer and monomer).

In the ionic state, at the geometry of the neutral (vertical ionization region) the additional electronic relaxation will reduce the observed binding energy even further. The shift in the Koopman's theorem ionization potential of 0.9 eV and in the vertical ionization potential of 1.32 eV for water dimer, calculated by M. Newton,<sup>15</sup> demonstrate the significance of these effects. Unfortunately, the vertical ionization potential shift is not easily obtained in a photoionization experiment, due to autoionization and other cross-section effects. The slow rise in the photoionization efficiency of  $(\text{H}_2\text{O})_2$  indicates a change in geometry, and a vertical ionization potential larger than the upper bound to the adiabatic ionization potential measured in this work ( $11.21 \pm 0.09$  eV yields a shift in the adiabatic ionization potential of  $1.40 \pm 0.09$  eV using  $12.615 \pm 0.001$  eV<sup>11,12</sup> for the monomer).

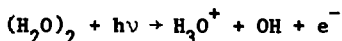
The water dimer ion,  $(\text{H}_2\text{O})_2^+$  is isoelectronic with  $\text{Ne}_2^+$ . This rare-gas molecular ion has a dissociation energy of at least 1.36 eV<sup>16</sup> and an estimated  $R_e = 1.75$  Å. The molecular dimer ion of water has the same bonding capabilities (bond order 1/2) and thus a similar stability. The measured upper bound to the adiabatic ionization potential,  $11.21 \pm 0.09$  eV, combined with the monomer's ionization potential  $12.615 \pm 0.001$  eV<sup>11,12</sup> and the bond strength of the hydrogen bond,<sup>17</sup> yields a dissociation energy of at least  $1.58 \pm 0.13$  eV for  $(\text{H}_2\text{O})_2^+$  with respect to  $\text{H}_2\text{O}^+$  and  $\text{H}_2\text{O}$ , or shows that  $(\text{H}_2\text{O})_2^+$  is stable by more than  $0.52 \pm 0.12$  eV with respect to  $\text{H}_3\text{O}^+$  and OH. This latter dissociation channel is the key to absolute proton affinity determination.

The dissociation mechanism needed in such determinations must produce threshold electrons and leave no excess potential or kinetic energy<sup>18</sup> in the products. Autoionization in many cases satisfies the first criteria, production of threshold electrons.<sup>16</sup> The latter condition is satisfied by an ionic state with the appropriate dissociation products. If the dissociation mechanism is adiabatic, then many otherwise difficult heats of formation can be determined.

The following dissociation channels of water are adiabatic:<sup>19,20</sup>

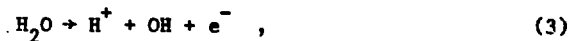
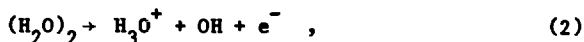


The similar dissociation process of interest



is also expected to be adiabatic.

The threshold measurements for the dissociative ionization of  $(\text{H}_2\text{O})_2$  enable the determination of the proton affinity of  $\text{H}_2\text{O}$  via the set of reactions:



The exoergicity of (1) is taken as  $0.17 \pm 0.04$  eV ( $4 \pm 1$  kcal/mole).<sup>17</sup> The enthalpy of (2) is the observed appearance potential of  $\text{H}_3\text{O}^+$ :  $11.73 \pm 0.03$  eV ( $270.5 \pm 0.7$  kcal/mole). The degree of rotational and low frequency vibrational relaxation in the supersonic expansion will make the temperature corrections to this threshold less than the other uncertainties. The fragmentation threshold (3) is  $18.75 \pm 0.03$  eV ( $432.4 \pm 0.2$  kcal/mole).<sup>19,20</sup> The appropriate sum of these enthalpies yields the proton affinity of  $\text{H}_2\text{O}$ , (4) as  $7.18 \pm 0.08$  eV ( $165.8 \pm 1.8$  kcal/mole) at 0 K. Other recent determinations of the proton affinity of water are listed in Table 3 for comparison.

Appearance potential measurements on higher clusters will yield information concerning their proton solvation energies. Preliminary measurements on  $(\text{H}_2\text{O})\text{H}^+$  indicate a larger proton affinity. The energetics of following the solvation of a proton to that in liquid water are shown in Fig. 4.

#### D. Photoion Yield of $\text{N}^+$ from $\text{N}_2$ , $\text{C}^+$ from CO and $\text{H}^+$ from $\text{H}_2$

##### 1. Introduction

The electronic structures of  $\text{N}_2$ ,<sup>21</sup> CO,<sup>22</sup> and  $\text{H}_2$ <sup>23</sup> have been extensively studied by a variety of spectroscopic techniques. Photoionization, photoelectron, absorption and other forms of spectroscopy have mapped out the electronic states of these light diatomics below 21 eV. The high energy limit is imposed by the absence of intense conventional laboratory continuum-radiation sources. The recent increase in the availability of intense continuum synchrotron light sources has fostered additional studies at higher photon energies.<sup>24</sup>

The isoelectronic diatomic ions  $N_2^+$  and  $CO^+$  are so strongly bound that photon energies greater than 21 eV are necessary to observe  $N^+$  and  $C^+$  products, respectively, from dissociative ionization of the neutrals. Previous photoionization studies using resonance-line sources measured the ion yield ratios of  $N^+/N_2^+$ ,  $C^+/CO^+$  and  $O^+/CO^+$ .<sup>25</sup> However, because of the fixed frequencies of these lines neither the details of the dissociative ionization process nor accurate thresholds were determined. The HeII photoelectron spectra of  $N_2$ <sup>26</sup> and  $CO$ <sup>27</sup> showed only weak features in the binding energy region relevant to the dissociative ionization process. Fluorescence measurements<sup>28</sup> from the electron-impact excited  $N_2^+$ ,  $C^2\Sigma_u^+$  state indicated a competition between emission and pre-dissociation. Several Rydberg series converging to this  $C^2\Sigma_u^+$  state have been observed in absorption<sup>29</sup> spectra which were obtained using synchrotron radiation. This evidence implies that autoionization might play an important role in the dissociative ionization mechanism. In order to help determine the details of the dissociative ionization mechanism, the photoionization yield of  $N^+$ ,  $N_2^+$ ,  $C^+$ ,  $CO^+$  were measured at SSRL.

Proton kinetic energies in excess of 1 eV have been measured from the dissociative photoionization of  $H_2$  at excitation energies of 26.9 eV<sup>30</sup> and 40.8 eV.<sup>31</sup> A recent theoretical work<sup>32</sup> has attributed these fast (1 to 4 eV) protons to dissociative autoionization from a  $1\Sigma_u^+$  state. The theoretical calculation also predicts an enhancement in the partial photoionization cross section near 30 eV. To test this prediction, the photoionization efficiency of  $H^+$  from  $H_2$  was measured.

## 2. Experimental

These photoionization measurements were performed in conjunction with the neon dimer experiment at SSRL. The apparatus is essentially the same as described in the first chapter except for the following changes: (1) a second 500 l/sec turbomolecular pump was added to the beam source chamber; (2) the nozzle diameter increased to 50  $\mu\text{m}$ ; and (3) the ion extraction lenses were modified to allow operation at greater electric fields than before. In all cases the pure sample gas was expanded at room temperature and at a pressure such that clusters in the beam were undetectable. The expansion pressures used, measured with a MKS Baratron pressure transducer, were 1119 torr, 1106 torr, and 741 torr for  $\text{N}_2$ , CO and  $\text{H}_2$ , respectively. The data collection scheme was identical except that the zero order position was measured before and/or after each scan in order to correct for any shift in the wavelength calibration of the monochromator.

## 3. Results and Discussion

The measured photoionization yield of  $\text{N}_2^+$  and  $\text{N}^+$  from  $\text{N}_2$  using a photon energy resolution of 2.5  $\text{\AA}$  FWHM is shown in Fig. 5. The vertical scale is arbitrary as are the relative ion mass signals. The observed threshold for  $\text{N}^+$  production,  $510.9 \pm 1.5 \text{\AA}$  ( $24.27 \pm 0.07 \text{ eV}$ ) is in excellent agreement with the spectroscopic value of  $24.2937 \text{ eV}$ <sup>33</sup> for the production of  $\text{N}^+(\text{}^3\text{P}) + \text{N}(\text{}^4\text{S})$  and the electron bombardment appearance potential measurement of  $24.32 \pm 0.03 \text{ eV}$ .<sup>34</sup> The excited product dissociation limits,  $\text{N}^+(\text{}^3\text{P}) + \text{N}(\text{}^2\text{D})$ ,  $\text{N}^+(\text{}^3\text{P}) + \text{N}(\text{}^2\text{P})$ ;  $\text{N}^+(\text{}^1\text{D}) + \text{N}(\text{}^4\text{S})$ ,  $\text{N}^+(\text{}^1\text{D}) + \text{N}(\text{}^2\text{D})$ ,  $\text{N}^+(\text{}^1\text{D}) + \text{N}(\text{}^1\text{D})$ ; and  $\text{N}^+(\text{}^1\text{S}) + \text{N}(\text{}^4\text{S})$  calculated from the known atomic energy levels<sup>35</sup> are also shown. The minor changes in the yield

observed near these energies indicate the participation of the molecular states with these atomic limits in the dissociative ionization process. The most intense feature, which peaks at 472 Å, extends from threshold to the  $N^+(^3P) + N(^2D)$  atomic limit. This feature might be due to molecular Rydberg states which have an ionic-molecular core with  $N^+(^3P) + N(^2D)$  atomic dissociation products.

The  $N_2^+$  photoionization efficiency (Fig. 5) has been extensively studied<sup>36</sup> from threshold (796 Å) to 600 Å. The sharp features between 700 Å and 660 Å appear as noise due to the few data points collected in this region. These intense sharp features are the result of autoionizing Rydberg states converging to the  $B^2\Sigma_u^+$  molecular ion.<sup>36</sup> The adiabatic ionization potential of this state and the other known higher lying molecular ionic states are also indicated in Fig. 5. Figure 6 shows the potential energy curves for these states. The broad increase in the ionization efficiency between 570 Å and 500 Å was partially resolved with 0.8 Å FWHM photon resolution. This scan and a scan of  $N^+$  production near threshold are shown in Fig. 7. The peaks in the  $N_2^+$  yield are assigned to autoionization from the Rydberg series converging to the  $C^2\Sigma_u^+$  state of  $N_2^+$ . This assignment is based on the absorption data of Codling,<sup>29</sup> shown in Fig. 7. Also indicated in this figure are the  $C^2\Sigma_u^+$  vibrational energy levels.<sup>21</sup> The  $C^2\Sigma_u^+$  state is one of several ionic states with  $N^+(^3P) + N(^2D)$  atomic dissociation products, and is the only state to which the corresponding Rydberg states have been assigned.

The peaks observed in the  $N^+$  photoionization yield agree (to within 0.4 Å) with the higher vibrational levels of the Rydberg states seen in absorption; and, as previously mentioned, also seen in the  $N_2^+$  photoionization yield. As the photon energy increases above the threshold for  $N^+$  production, the intensity of the autoionization peaks decrease in the  $N_2^+$  photoion yield but continue to increase in the  $N^+$  fragment yield.

The Rydberg states with  $C^2\Sigma_u^+$  core should autoionize to  $B^2\Sigma_u^+$  ions due to the similarity in their orbital configurations. The lowest lying orbital configurations of  $N_2^+$  are shown in the insert in Fig. 6. The  $B^2\Sigma_u^+$  and  $C^2\Sigma_u^+$  states cannot be described by single orbital configurations, but require the linear combinations of at least two of the configurations shown in Fig. 6. Above 23.583 eV (525.74 Å) an additional autoionization channel can produce  $C^2\Sigma_u^+$  ions. However, this channel should not contribute significantly, due to the large discrepancy between the vibrational quantum numbers of the observed Rydberg states and the accessible ionic states. Therefore, the observation of the same autoionizing Rydberg states in both the  $N_2^+$  and  $N^+$  photoion yield strongly indicates that dissociation is competitive with the autoionization of these Rydberg states. In addition, if these Rydberg states do have the  $C^2\Sigma_u^+$  core, as assigned in the absorption spectra,<sup>29</sup> then their observation in the  $N^+$  yield supports the recently proposed homogenous dissociation mechanism of the  $^{37}C^2\Sigma_u^+$  state.

Besides the resolved autoionization structure in the  $N^+$  photoion yield there is apparent agreement between the vibrational energy levels of the  $C^2\Sigma_u^+$  state and step-like features. Unfortunately, the inability to resolve the autoionization peaks from the steps makes it impossible to determine the importance of direct ionization in this dissociative ionization process.

The measured photoionization yields of  $C^+$  and  $CO^+$  from CO are shown in Fig. 8. Since  $N_2$  and CO are isoelectronic, the general features in their photoionization efficiency are similar. In contrast to nitrogen dissociative ion pair processes are allowed due to the stability of  $O^-$  and  $C^-$ . The possible fragmentation channels, in order of increasing energy are



Due to the very small cross-sections for the latter two channels, the photoionization yield of the  $O^+$  signal was not measured. The only fragment ion measured was  $C^+$ . The first process could only be studied between its appearance potential and that of the much more efficient second process.

Absorption,<sup>38</sup> photoelectron<sup>39</sup> and fluorescence<sup>40</sup> spectra revealed the presence of several ionic states between 21 eV and 37 eV. All of these ionic states have a primary orbital configuration that involves excitation of an additional electron besides the one removed upon ionization of the neutral. This implies that to understand the nature



of excitation to these states more than a single-configuration wave-function is necessary. The lowest two of these states are  $D^2\Pi$  and  $C^2\Sigma^+$ . The primary configuration of the  $D^2\Pi$  state is obtained by removing a  $\pi 2p$  electron and exciting an additional  $\pi 2p$  electron to the antibonding  $\pi^* 2p$  orbital. This reduces the bond order by two thus decreasing the dissociation energy and increasing the equilibrium bond distance. The  $C^2\Sigma^+$  state has a primary orbital occupancy that is reached by removing a  $\pi 2p$  electron and exciting a  $2p$  electron to the  $\pi^* 2p$  orbital. This configuration has similar effects on the dissociation energy and the equilibrium bond distance as that mentioned for the  $D^2\Pi$  state. These configurations are mixed with others to represent the  $D^2\Pi$  and  $C^2\Sigma^+$  eigenstates. These two states are responsible for weak features in the photoelectron spectra<sup>39</sup> and are the ionic cores of several intense Rydberg series observed in absorption.<sup>38</sup>

The  $C^+$  photoionization yield is shown in Fig. 8. Between the thresholds for processes (1) and (2) a large number of peaks and shoulders are observed. These features agree well with the Rydberg states converging to the C and D ion observed in absorption and thus play a role in the dissociative ionization process.

The quality of the photoionization efficiency data obtained for the  $CO^+$  ion was inferior to that reported for  $Ne_2^+$  and  $N_2^+$ . This was believed to be the result of instabilities in the position of the stored electron beam in SPEAR at the time these data were being collected. The fluctuation in the stored beam position due to the lack of an operable automatic-steering control monitor manifests itself as charges in the output photon beam position. This moves the ionization

region reducing the collection efficiency of the mass spectrometer. These changes are not directly compensated for in the measured photon flux, leaving experimental artifacts in the observed photoionization efficiency. The data collected for the  $\text{CO}^+$  channel are plagued by these artifacts to the extent that assignments of several sharp structures and overall trends are questionable.

In the course of performing these experiments on  $\text{N}_2$  and  $\text{CO}$  two other laboratories reported data on the  $\text{CO}$  system.<sup>41,42</sup> One of these groups<sup>42</sup> also reported measurements on the  $\text{N}_2$  system. Their nitrogen data are in excellent agreement with those obtained in this laboratory. The  $\text{CO}^+$  photoion yields reported by both laboratories are in agreement with each other and are of superior quality to those shown in Fig. 8. The  $\text{C}^+$  photoionization yields reported by both laboratories and that presented in Fig. 8 are very similar.

The measured photoionization yields of  $\text{H}_2^+$  and  $\text{H}^+$  from  $\text{H}_2$  between 700 Å and 350 Å are shown in Fig. 9. The primary objective of this experiment was to look for evidence in the partial photoionization cross section of a predicted dissociative autoionizing state that is responsible for production of fast (1 to 4 eV) protons. Theoretical calculations<sup>23</sup> predicted that this process should appear as a resonance in the photoabsorption cross-section with a width of 6 eV (FWHM) at approximately 30 eV photon energy. The enhancement in the total cross-section at the peak was predicted to be  $1 \times 10^{-19} \text{ cm}^2$ . Since the total absorption cross-section at 26.9 eV is  $3.6 \times 10^{-18} \text{ cm}^2$ ,<sup>43</sup> this resonance will only be a 2% effect in absorption. However, the dissociative ionization

cross section is only  $4 \times 10^{-20} \text{ cm}^2$ ,<sup>44</sup> making this resonance a dramatic effect.

The predicted resonance peak position and half-width at half-maximum (3 eV) are indicated in Fig. 9. The observed  $\text{H}^+$  photoion yield does significantly increase in this photon energy region. However, the experimental data suffer from three difficulties, none of which have been completely resolved. These difficulties are: (1) The collection efficiency of the extraction lenses for these fast protons is not known and believed to be much less than unity; (2) The transmission of the quadrupole mass filter as a function of kinetic energy and mass is also not known; and (3) The scattered light on the  $8^\circ$  line at SSRL is of the same order of magnitude as the monochromatic component at these high photon energies. Thus qualitatively the presence of the resonance is confirmed however quantitatively its position width and intensity are still uncertain.

#### E. Photoion Yield of $\text{N}_3^+$ from $(\text{N}_2)_2$ and $\text{C}_2\text{O}^+$ from $(\text{CO})_2$

Ion molecule reactions occurring at high pressures in electron bombardment mass spectrometers can produce extensively clustered ions and fragments.<sup>45</sup> Studies of  $\text{N}_2$  and CO reactions have shown that  $\text{N}_3^+$  and  $\text{C}_2\text{O}^+$  are products of an excited electronic state reaction of  $\text{N}_2^+$  and  $\text{CO}^+$  respectively.<sup>46</sup> These conclusions were based on appearance potentials and rate constant measurements. The measured appearance potentials were  $21.04 \pm 0.05 \text{ eV}$  for  $\text{N}_3^+$  and  $19.6 \pm 0.5 \text{ eV}$ <sup>47</sup> for  $\text{C}_2\text{O}_3^+$ . The excited state(s) involved in these reactions in the high pressure experiment were predicted to have lifetimes of  $>10^{-6} \text{ sec}$ .<sup>48</sup> Low pressure ICR studies on these same reactions indicated that the lifetime of the

longest lived state must be  $>10^{-2}$  sec and  $>10^{-3}$  sec for  $N_2^{+49}$  and  $CO^{+50}$  respectively. Several investigators have suggested both long-lived states could possibly be  $4\Sigma^+$  states that were theoretically predicted in this energy region.<sup>51</sup> Other investigators suggested that for  $N_2$  the high vibrational levels  $v' > 19$  of its  $A^2\Pi_u$  state, which have apparent lifetimes of  $6 - 7 \times 10^{-2}$  sec, could be responsible for the  $N_3^+$  production.<sup>52</sup>

The photoionization mass spectra of clusters in  $N_2$  and CO beams were measured, in order to determine the photoionization threshold for  $N_3^+$  and  $C_2O^+$  production from  $(N_2)_2$  and  $(CO)_2$ , respectively. These measurements were performed at SSRL in conjunction with the studies reported on  $N_2$  and CO. The experimental apparatus and technique used were the same as previously described.<sup>53</sup> The cluster formation in the beam was enhanced by expanding the pure sample gas  $N_2$  or CO at 77 K at pressures of 400 torr and 300 torr, respectively. The recorded photoionization efficiency of  $N_4^+$  and  $N_3^+$ , and  $C_2O^+$  and  $(CO)_2^+$  with a photon resolution of 8.7 Å FWHM are shown in Figs. 10 and 11 respectively.

The observed photoion signals at 458 Å for the different masses with respect to the monomer parent ion were 1.0 ( $N_2^+$ ); 0.040 ( $N_4^+$ ); 0.032 ( $N^+$ ); 0.0013 ( $N_3^+$ ) and 1.0 ( $CO^+$ ); 0.182 ( $(CO)_2^+$ ); 0.053 ( $C^+$ ); 0.0037 ( $C_2O^+$ ); 0.0021 ( $C_3O_2^+$ );  $<0.0005$  ( $CO_2^+$ ). These signals are not corrected for mass-dependent transmission of the quadrupole. The mass 44 signal  $CO_2^+$  is believed to have arisen predominately from residual gas in the ionization region. The thresholds for both  $N_3^+$  and  $C_2O^+$  were not well-defined, due to the very slow rise of the photoion signal. The  $N_3^+$  measured appearance potential of  $22.1 \pm 0.4$  eV

is larger than the high pressure electron bombardment mass spectrometry value of  $21.04 \pm 0.05$  eV,<sup>47</sup> but agrees reasonably well with the value reported in the ICR studies of  $22.6 \pm 0.6$  eV.<sup>49</sup> The appearance potential obtained for  $C_2O^+$  ion was  $19.4 \pm 0.4$  eV, which is in agreement with the high pressure mass spectrometry studies ( $19.6 \pm 0.5$  eV)<sup>47</sup> but significantly lower than the value of  $21.3 \pm 0.5$  eV<sup>50</sup> reported in the ICR work. The reason for these discrepancies is not understood and will require additional photoionization experiments.

The  $(N_2)_2^+$  photoionization yield appears to be flat over the energy region studied. However, the  $N_3^+$  photoion yield displays the two distinct changes in slope. Also shown on Fig. 10 are the adiabatic ionization potentials of the  $D^2\Pi_u$  and  $C^2\Sigma_u^+$  states of  $N_2^+$ , and the threshold for  $N^+$  production. There is a possible correlation between the  $N^+$  threshold and one of the changes in slope in the  $N_3^+$  photoion yield. However, the assignment of this feature requires higher resolution data.

The  $(CO)_2^+$  photoionization efficiency has several broad features that resemble those found in  $CO^+$ .<sup>54</sup> As with the  $N_3^+$  photoion yield the  $C_2O^+$  photoion yield has two distinct changes in its slope and again the first change above threshold is located near the  $C^+$  appearance potential. Assignment of this structure is certainly questionable until higher quality data are available.

The changes in slope in the photoionization efficiencies of  $N_3^+$  and  $C_2O^+$  imply the existence of at least two mechanisms controlling their formation. However, identification of these mechanisms has not been made. If the high  $v'$  levels of the  $A^2\Pi$  states are active, higher resolution scans should confirm this hypothesis.

**References: Chapter III**

1. C. Y. Ng, Ph.D. Thesis, University of California, Berkeley, 1976.
2. A. D. Walsh and P. A. Worsop, *Trans. Faraday Soc.* 57, 345 (1961).
3. W. A. Chupka and M. E. Russell, *J. Chem. Phys.* 48, 1527 (1968).
4. J. Berkowitz, "Photoabsorption, Photoionization and Photoelectron Spectroscopy," Academic Press (1979).
5. G. Herzberg, "Molecular Spectra and Molecular Structure," vol. III, Van Nostrand Reinhold Co. (1966).
6. R. Yamdagni and P. Kebarle, *J. Am. Chem. Soc.* 98, 1320 (1970);  
P. Kebarle, R. Yamdagni, K. Hiraoka, T. B. McMahon, *Int. J. Mass. Spectrom. Ion Phys.* 19, 71 (1976).
7. C. Y. Ng, B. H. Mahan, and Y. T. Lee, *J. Chem. Phys.* 65, 1956 (1976).
8. C. Y. Ng, D. J. Trevor, B. H. Mahan, and Y. T. Lee, *J. Chem. Phys.* 65, 4327 (1976); *ibid* 66, 446 (1977).
9. C. Y. Ng, P. W. Tiedemann, B. H. Mahan, and Y. T. Lee, *J. Chem. Phys.* 66, 3385 (1977).
10. V. H. Dibeler, J. A. Walker and M. Rosenstock, *J. Res. Nat. Bur. Stand. (U.S.)*, 70A (Phys. and Chem.), 459 (1966).
11. B. Brehm, *Z. Naturforsch* 21a, 196 (1966); A. J. C. Nicholson, *J. Chem. Phys.* 43, 1171 (1965).
12. L. Karisson, L. Mattsson, R. Jadny, R. G. Albridge, S. Puchas, T. Bergmark, and K. Siegbahn, *J. Chem. Phys.* 62, 4745 (1975);  
R. N. Dixon, G. Duxbury, J. W. Rabalais, and L. Asbrink, *Mol. Phys.* 31, 423 (1976).
13. J. Berkowitz, "Photoabsorption, Photoionization and Photoelectron Spectroscopy," Academic Press (1979) p. 243.

14. T. R. Dyke, K. M. Mack, and J. S. Kuznetz, *J. Chem. Phys.* 66, 498 (1977).
15. M. Newton, a SCF calculation using a double  $\zeta$  basis set; private communication.
16. See chapter II and references made there.
17. Many experimental and theoretical values for the heat of formation of water dimer have been reported. The majority are between 3 and 6 kcal/mole. A value of  $4 \pm 1$  kcal/mole is used as a compromise. A few of these values are: Submillimeter absorption studies between 20 - 50°C,  $E = 5.2 \pm 1.5$  kcal/mole, H. A. Gebbie, W. J. Burroughs, J. Chamberlain, J. E. Haris, and R. G. Jones, *Nature* 221, 143 (1969); Infrared band intensities, 3.8 kcal/mole, W. P. Luck, in "The Hydrogen Bond, Recent Developments in Theory and Experiments." Edited by P. Schuster, G. Zundel, and C. Sandorfy (North-Holland, New York, 1976) p. 1396; Second virial coefficient from different potentials, 3 and 4 kcal/mole, C. Braun and H. Leidecker, *J. Chem. Phys.* 61, 3104 (1974); Empirical fit to experimental parameters, 3.5 kcal/mole, L. L. Shipman and H. A. Scheraga, *J. Chem. Phys.* 78, 909 (1974); Ab initio CI,  $\sim 5$  kcal/mole, G. H. F. Diercksen, W. P. Kraemer, and B. Roos, *Theor. Chim. Acta* 36, 49 (1975).
18. If the excess energy and kinetic energy are known the the appearance potential can be corrected. However, this is rarely the case due to the complexity of such a measurement.
19. W. A. Chupka, "Chemical Spectroscopy and Photochemistry in the Vacuum Ultraviolet," (C. Sandorfy, P. J. A. Ausloos and M. B. Robin, eds.), D. Reidel Publishing Co. (1974) p. 443.

20. K. E. McCulloch, *Int. J. of Mass Spectroscopy and Ion Physics* 21, 333 (1976); R. Stockbauer, *J. Chem. Phys.* 72, 5277 (1980).
21. A. Lofthus and P. H. Krupenie, *J. Phys. and Chem. Ref. Data* 6, 113 (1977); and F. R. Gilmore, *J. Quant. Spectrosc. Radiat. Transfer* 5, 369 (1965).
22. K. P. Huber and G. Herzberg, "Molecular Spectra and Molecular Structure IV. Constants of Diatomic Molecules," Van Nostrand Reinhold Co., 1979, pp. 158-171.
23. K. P. Huber and G. Herzberg, "Molecular Spectra and Molecular Structure IV. Constants of Diatomic Molecules," Van Nostrand Reinhold Co., 1979, pp. 240-255; and T. E. Sharp, *Atomic Data* 2, 119 (1971).
24. L. C. Lee, R. W. Carlson, D. L. Judge, M. Ogawa, *J. Quant. Spectrosc. Radiat. Transfer* 13, 1023 (1973); P. Gurtler, V. Saile, and E. E. Koch, *Chem. Phys. Lett.* 48, 245 (1977); E. W. Plummer, T. Gustafsson, W. Gudat and D. E. Eastman, *Phys. Rev. A* 15, 2339 (1977).
25. P. L. Kronebusch, J. Berkowitz, *Int. J. Mass Spec. Ion Phys.* 22, 283 (1976).
26. L. Asbrink and C. Fridh, *Physica Scripta* 9, 338 (1974); J. L. Gardner and J. A. R. Samson, *J. Elect. Spec. Relat. Phenom.* 2, 259 (1975), *J. Chem. Phys.* 62, 1447 (1975).
27. J. A. R. Samson and J. L. Gardner, *J. Elect. Spec. Relat. Phenom.* 8, 35 (1976).
28. C. A. van de Runstraat, F. J. de Heer, and T. R. Govers, *Chem. Phys.* 3, 431 (1974).



29. K. Codling, *Astrophys. J.* 143, 552 (1966).
30. R. Browning and J. Fryar, *J. Phys. B* 6, 364 (1973).
31. J. L. Gardner and J. A. R. Samson, *Phys. Rev. A* 12, 1404 (1975).
32. K. Kirby, S. Guberman, and A. Dalgarno, *J. Chem. Phys.* 70, 4635 (1979).
33. This value obtained using  $D_0(X^2\Sigma_g^+, N_2^+) = 70273 \text{ cm}^{-1}$  and  $T_0 = 125667.5 \text{ cm}^{-1}$ . See Ref. 21 page 165 for discussion.
34. P. M. Hierl and J. L. Franklin, *J. Chem. Phys.* 47, 3154 (1967).
35. C. E. Moore, "Atomic Energy Levels; Vol. I" Circular of Nat. Bureau of Stand. 467 (1949).
36. G. R. Cook and P. H. Metzger, *J. Chem. Phys.* 41, 321 (1964); and J. Berkowitz "Photoabsorption, Photoionization and Photoelectron Spectroscopy" Academic Press, New York, 1979 page 218.
37. A. L. Roche and J. Tellinghuisen, *Mol. Phys.* 38, 129 (1979).
38. K. Codling and A. W. Potts, *J. Phys. B* 7, 163 (1974).
39. M. S. Banna and D. A. Shirley, *J. Electron Spectrosc. Relat. Phenom.* 8, 367 (1976); and K. Siegbahn et al., "ESCA Applied to Free Molecules," North-Holland Publ. (1969).
40. D. A. Shirley, "Topics in Applied Physics," vol. 26 page 165.
41. H. Oertel, H. Schenk, and H. Baumgartel, DESY preprint SR-79/28, October 1979.
42. M. Nakamura, Y. Morioka, Y. Iida, H. Masuko, T. Hayaishi, E. Ishiguro and M. Sasanauma, "VI International Conf. on Vac. Ultraviolet Rad. Phys.," Abstract II-23 (1980).
43. G. R. Cook and P. H. Metzger, *J. Opt. Soc. Am.* 54, 968 (1964).
44. S. V. O'Neil and W. P. Reinhardt, *J. Chem. Phys.* 69, 2126 (1978).

45. J. L. Franklin, "Ion-Molecule Reactions," vol. I, Plenum Press (1972) Chapter 2.
46. M. S. B. Munson, F. H. Field and J. L. Franklin, J. Chem. Phys. 37, 1790 (1962).
47. E. W. McDaniel, V. Cermak, A. Dalgarno, E. E. Ferguson, and L. Friedman, "Ion-Molecule Reactions," Wiley (1970).
48. M. C. Cress, P. M. Becker and F. W. Lampe, J. Chem. Phys. 44, 2212 (1966).
49. M. T. Bowers, P. R. Kemper, and J. B. Laudenslager, J. Chem. Phys. 61, 4394 (1974).
50. M. T. Bowers, M. Chau and P. R. Kemper, J. Chem. Phys. 3, 3656 (1975).
51. J. C. Lorquet and M. Desouter, Chem. Phys. Lett. 34, 136 (1972).
52. R. F. Holland and W. B. Maier II, J. Chem. Phys. 57, 4497 (1972).
53. See Chapter II.B and III.D.
54. See Fig. 8, Ref. 41, and 42.

Table 1. Ammonia.

Adiabatic IP (eV)	Vibrational Spacing ( $\text{cm}^{-1}$ )	Method*	Reference
10.176 $\pm$ 0.008	950 $\pm$ 32	This work	
10.154 $\pm$ 0.01	not assigned	PI	a
10.35	not assigned	PE	b
10.17 $\pm$ 0.01	960 (average value)	PI	c
10.15	950 (average value)	PE	d
10.17 $\pm$ 0.010	970	PE	e
10.14	968	PE	f
10.15 $\pm$ 0.02	900	PE	g

\* PI denotes photoionization PE denotes photoelectron spectroscopy

<sup>a</sup>K. Watanabe, J. Chem. Phys. 26, 542 (1957).

<sup>b</sup>D. C. Frost, C. A. McDowell, and D. A. Vroom, Can. J. Chem. 45, 1343 (1967).

<sup>c</sup>W. A. Chupka and M. E. Russell, J. Chem. Phys. 48, 1527 (1968).

<sup>d</sup>G. R. Branton, D. C. Frost, F. G. Herring, C. A. McDowell, and I. A. Stenhouse, Chem. Phys. Lett. 3, 581 (1969).

<sup>e</sup>M. J. Weiss and G. M. Lawrence, J. Chem. Phys. 53, 214 (1970).

<sup>f</sup>G. R. Branton, D. C. Frost, T. Makita, C. A. McDowell, and I. A. Stenhouse, Phil. Trans. Roy. Soc. Lond. A268, 77 (1970).

<sup>g</sup>A. W. Potts and W. C. Price, Proc. Roy. Soc. Lond. A326, 181 (1972).

Table 2. Ozone.

Adiabatic IP (eV)	Vibrational Spacing ( $\text{cm}^{-1}$ )	Method*	Reference
$12.523 \pm 0.010$	$650 \pm 40$	This work	
$12.53 \pm 0.01$	630 (average value)	PE	a
$12.52 \pm 0.05$	not assigned	PE	b
$12.67 \pm 0.02$	not assigned	PI	c
$12.44 \pm 0.01$	650 (average value)	PE	d
$12.519 \pm 0.004$	$655 \pm 60$	PI	e

\*PI denotes photoionization      PE denotes photoelectron spectroscopy

<sup>a</sup>D. C. Frost, S. T. Lee, and C. A. McDowell, Chem. Phys. Lett. 24, 149 (1974).

<sup>b</sup>T. N. Radwan and D. W. Turner, J. Chem. Soc. A, 85 (1966).

<sup>c</sup>G. R. Cook, "Recent Developments in Mass Spectrometry," eds. K. Ogata and T. Kayakawa (Univ. Park Press, 1970) p. 761.

<sup>d</sup>J. M. Dyke, L. Golob, Neville Jonathan, A. Morris, and M. Okuda, J. Chem. Soc. Faraday Trans. II, 70, 1828 (1974).

<sup>e</sup>M. J. Weiss, J. Berkowitz, and E. H. Appelman, J. Chem. Phys. 66, 2049 (1977).

Table 3. Proton affinity of water.

Value (kcal/mole)	Temperature (k)	Reference
165.8 ± 1.8	0	This work
169 ± (1 or 2)	600	a
166.4 ± (1 or 2)	0	b
166 ± 2	...	c
165 ± 3	323-373	d
168.2 ± 3.4	340	e
164 ± 4	...	f
165.5	...	g

<sup>a</sup>Equilibrium measures with high pressure electron bombardments mass spec: Ref. 1.

<sup>b</sup>The value of Ref. 1 corrected to 0 K the JANAF Thermochemical Tables, Nat. Stand. Ref. Data Ser. 37, NBS (1971).

<sup>c</sup>Threshold of endothermic ion molecule reactions; R. J. Cotten and W. S. Koski, J. Chem. Phys. 59, 784 (1973).

<sup>d</sup>Bracketing technique using high pressure mass spectrometry: J. Long and B. Munson, J. Amer. Chem. Soc. 95, 2427 (1973).

<sup>e</sup>Bracketing technique using high pressure mass spectrometry: S. Chang, R. A. Myers, Jr., and J. L. Franklin, J. Chem. Phys. 56, 2427 (1972).

<sup>f</sup>Bracketing technique using ICR spectrometry: J. L. Beauchamp and S. E. Buttrill, Jr., J. Chem. Phys. 48, 1783 (1968).

<sup>g</sup>Ab initio: P. A. Kollman, C. F. Bender, Chem. Phys. Lett. 29, 271 (1973).

**Figure Captions: Chapter III**

- Fig. 1. Photoionization efficiency of  $\text{NH}_3^+$  with a photon resolution of 0.8 Å FWHM using the many line pseudo-continuum of  $\text{H}_2$  as light source.
- Fig. 2. Photoionization efficiency of  $\text{O}_3^+$  with a photon resolution of 0.8 Å FWHM using the  $\text{H}_2$  many line pseudo-continuum light source.
- Fig. 3. Photoionization yield of  $\text{H}_2\text{O}^+$ ,  $\text{H}_3\text{O}^+$  and  $(\text{H}_2\text{O})^+$  with a photon resolution of 2.5 Å FWHM using the  $\text{H}_2$  pseudo-continuum light source.
- Fig. 4. Thermodynamic cycle used for calculations of the proton affinity of  $\text{H}_2\text{O}$  and higher clusters; units (eV).
- Fig. 5. Photoionization efficiency of  $\text{N}^+$  and  $\text{N}_2^+$ , with a photon resolution of 2.5 Å FWHM. The relative intensities of  $\text{N}^+$  and  $\text{N}_2^+$  efficiencies are not drawn to scale.
- Fig. 6. Experimental potential energy curves for  $\text{N}_2$  and  $\text{N}_2^+$ , Ref. 21.
- Fig. 7. Photoionization efficiency of  $\text{N}^+$  and  $\text{N}_2^+$  with a photon resolution of 0.8 Å FWHM near the threshold for  $\text{N}^+$  production.
- Fig. 8. Photoionization efficiency of  $\text{CO}^+$  with a photon resolution of 2.5 Å FWHM, and of  $\text{C}^+$  with a photon resolution of 0.8 Å FWHM. The relative intensity of the two channels are not drawn to scale. The rapid changes in the  $\text{CO}^+$  photoion yield near 560 Å and 460 Å are experimental artifacts (see text for further details).

- Fig. 9. Photoionization efficiency of  $\text{H}_2$  with a photon resolution of 8.7 Å FWHM. The  $\text{H}^+$  and  $\text{H}_2^+$  signals are not drawn to scale. The high degree of scattered light below 400 Å is believed to cause the change in slope of the  $\text{H}_2^+$  yield.
- Fig. 10. Photoionization efficiency of  $\text{N}_3^+$  and  $\text{N}_4^+$  with a photon resolution of 8.7 Å FWHM. The scales of  $\text{N}_3^+$  and  $\text{N}_4^+$  yield are not the same.
- Fig. 11. Photoionization efficiency of  $\text{C}_2\text{O}^+$  and  $(\text{CO})_2^+$  with a photon resolution of 8.7 Å FWHM. The relative scales of the  $\text{C}_2\text{O}^+$  and  $(\text{CO})_2^+$  signals are not the same.

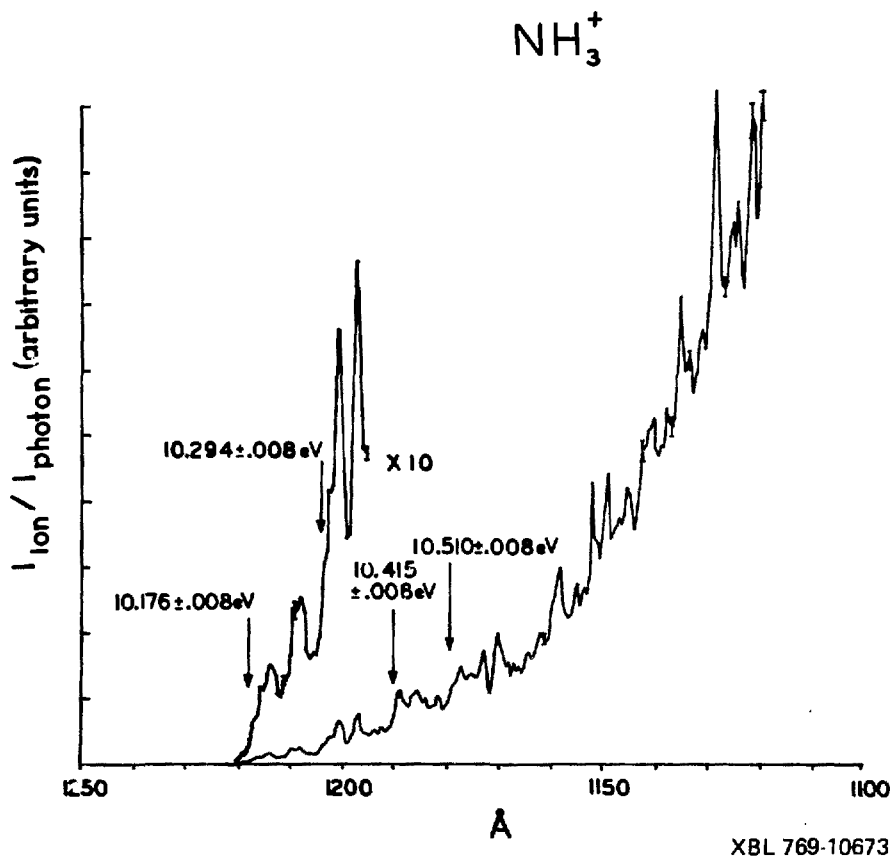


Fig. 1.



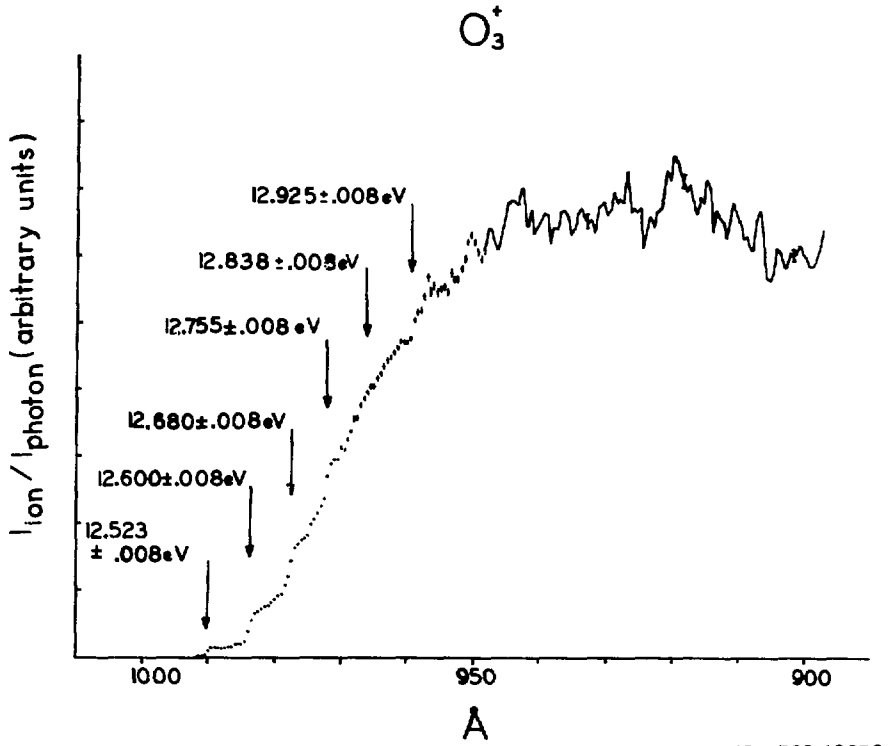
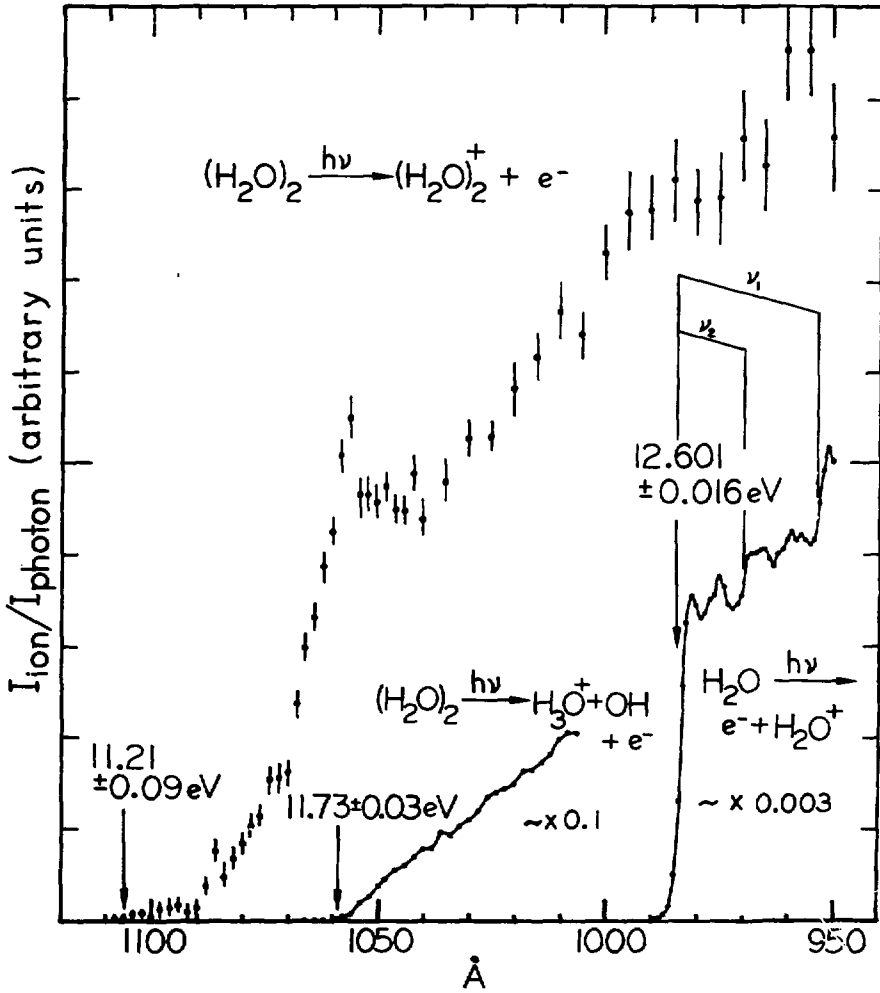
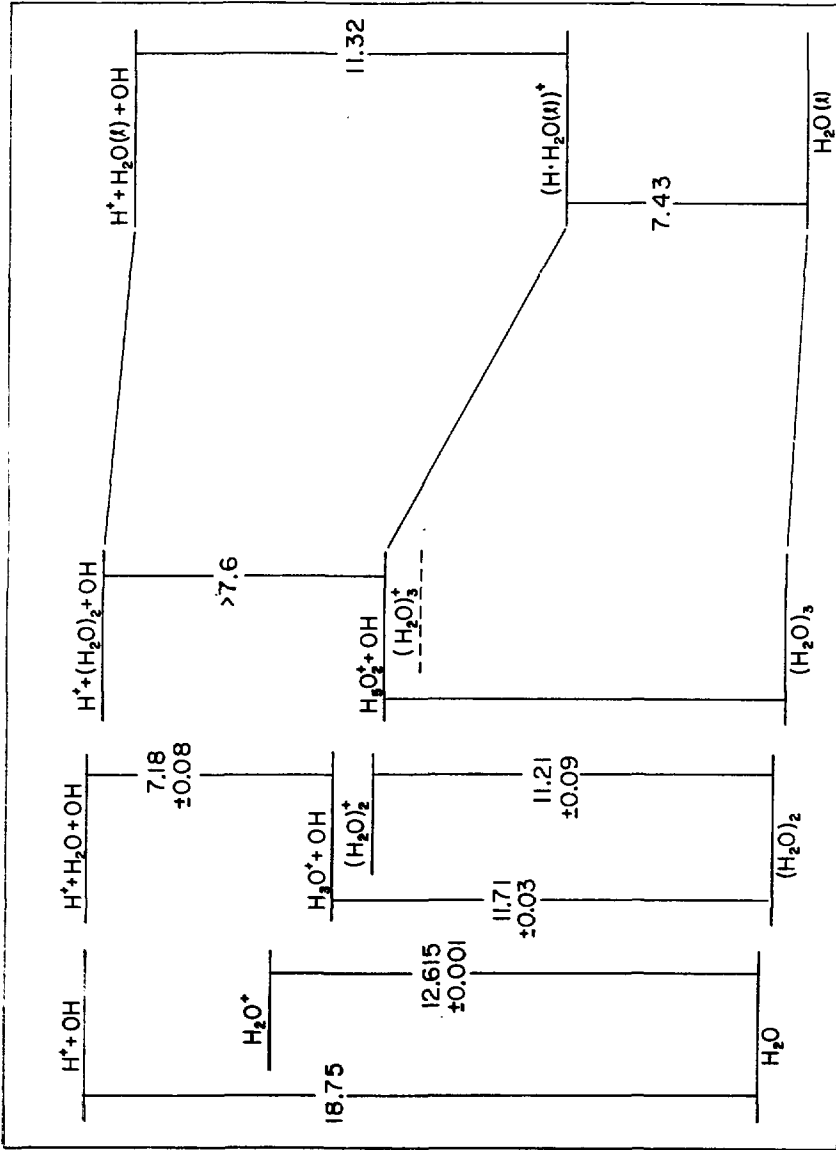


Fig. 2.



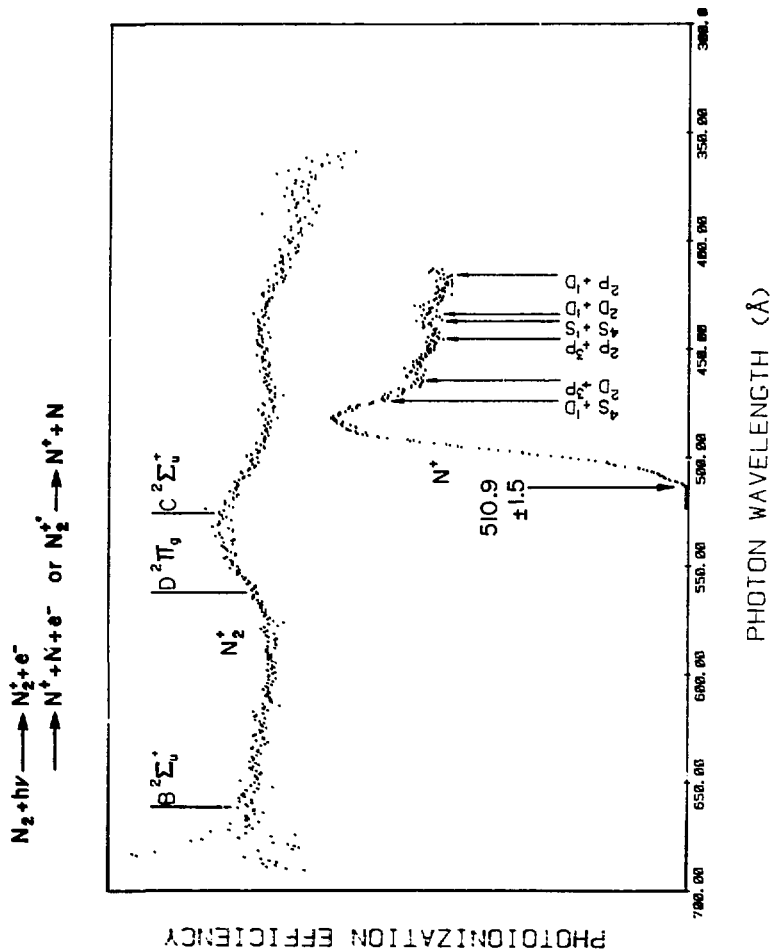
XBL 809-11806

Fig. 3.



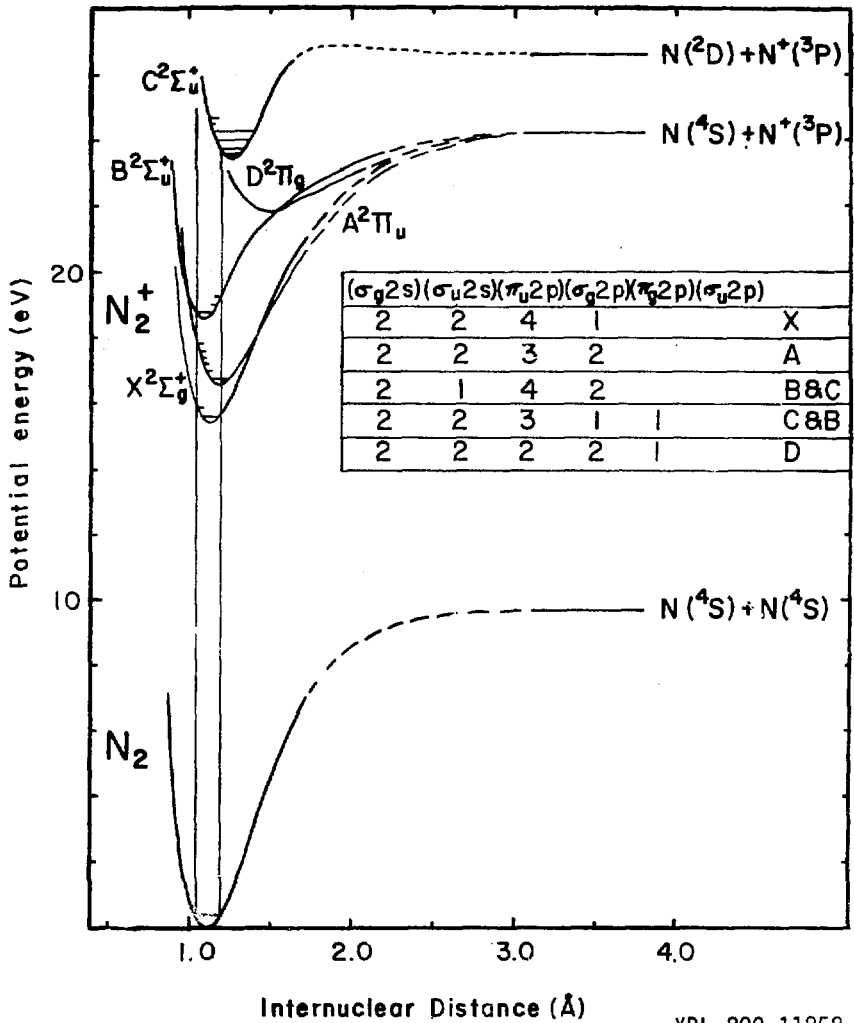
XBL 809-11860

Fig. 4.



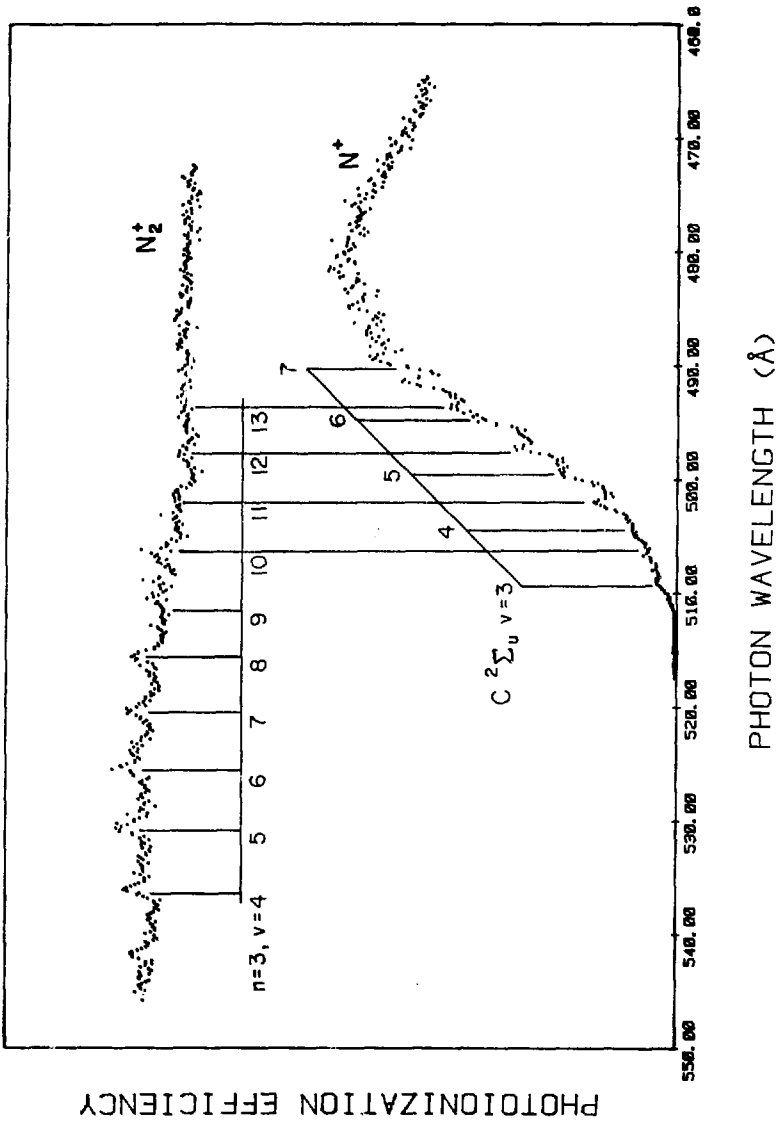
XBL 809-11807

Fig. 5.



XBL 809-11858

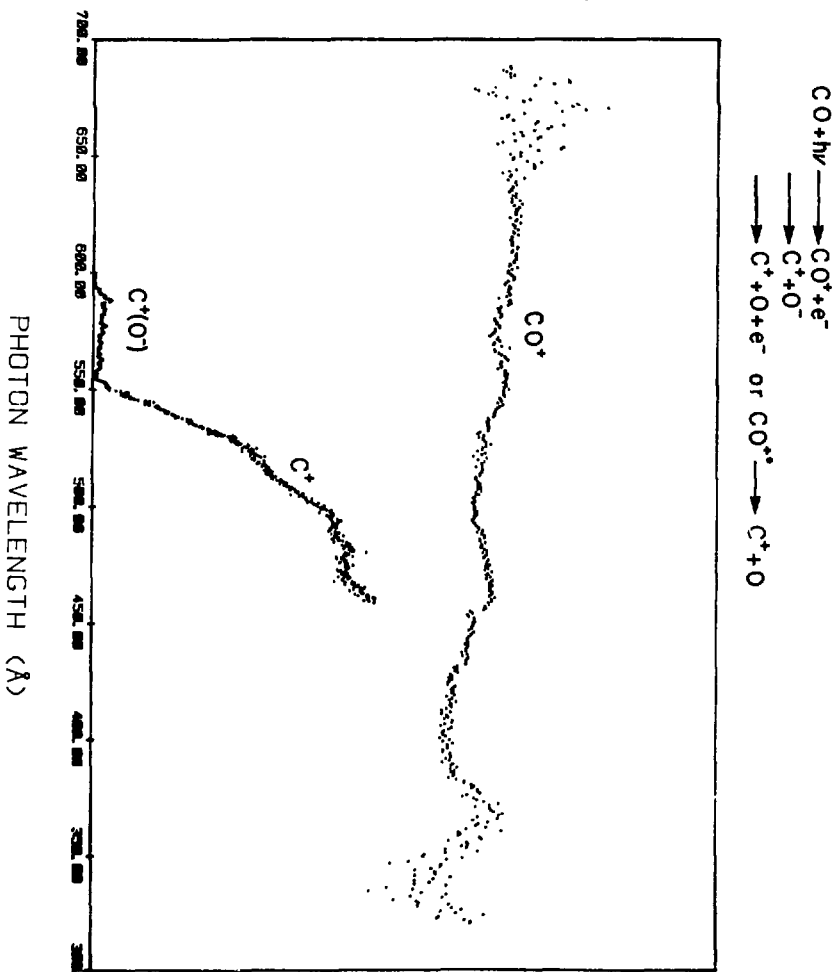
Fig. 6.



XBL 806-9895

Fig. 7.

PHOTOIONIZATION EFFICIENCY



PHOTON WAVELENGTH (Å)

Fig. 8.

XBL 806-9894

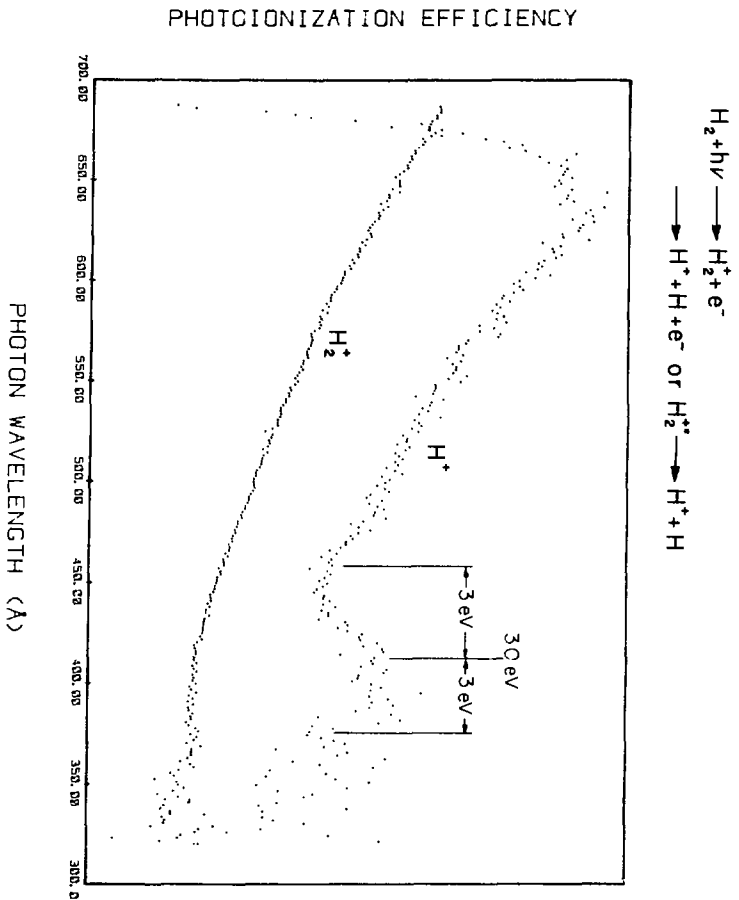
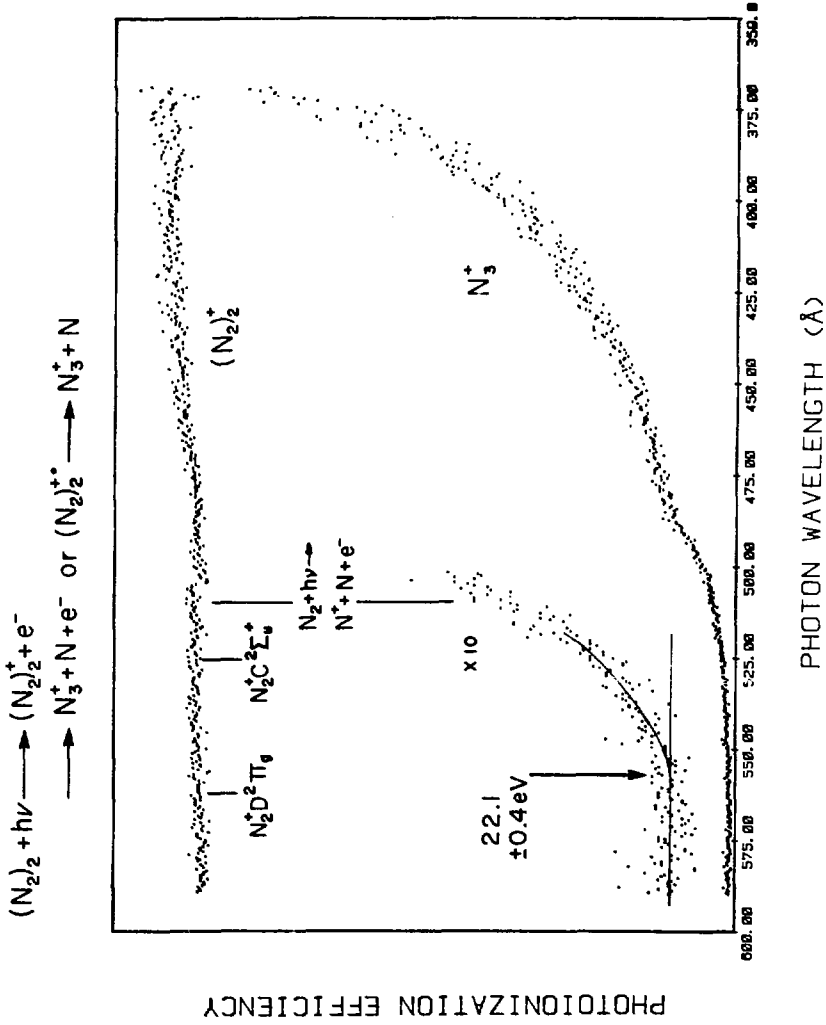


Fig. 9.

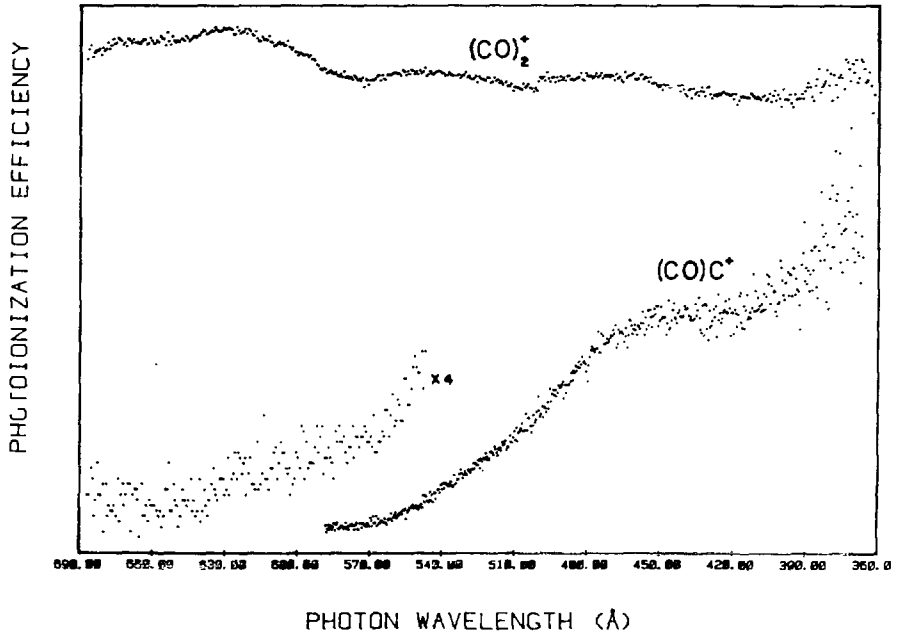
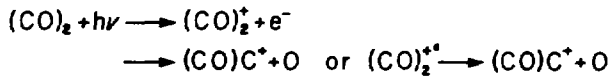
XBL 806-9869A





XBL 806-9871A

Fig. 10.



XBL 806-9870

Fig. 11.

## CHAPTER IV

PHOTOELECTRON SPECTROSCOPY AND FEASIBILITY OF  
PHOTOELECTRON-PHOTOION COINCIDENCE MEASUREMENTSA. Introduction

Photoelectron spectroscopy in the past decade has become a routine technique in chemistry and physics. Its ability to map out the binding energies of the electrons in the sample (gas, liquid or solid) has made it a very powerful method for understanding the electronic structure of these systems. Recently, the major emphasis in this field has been to extend the technique to more exotic systems.<sup>1</sup> This has been particularly true for gas-phase work, where photoelectron spectra have been obtained for high-temperature metal vapors,<sup>2</sup> free radicals<sup>3</sup> and rare-gas dimers.<sup>4</sup>

A typical gas-phase photoelectron spectrum consists of several bands, each of which corresponds to a different electronic state in the product ion. Each of these bands in turn consists of a series of peaks corresponding to the vibrational levels of the ion. The widths of these peaks, when observed, are limited by unresolved rotational states. This rotational broadening and additional unresolved splittings caused by effects such as spin-orbit interactions have limited the obtainable resolution in the majority of gas phase photoelectron spectra.

The observed intensities of the bands spectra are controlled by the dipole matrix elements between the initial state of the neutral molecule and the final continuum state, which consists of the ion and free electron. Calculating these matrix elements and comparing them to the photoelectron spectra provides a simple test of the quality of the initial- and final-state wavefunction. Certain weak photoelectron

bands are successfully predicted only when configuration interactions are incorporated.<sup>5</sup> However, the occasional poor signal-to-noise ratio in photoelectron spectrometers has left many of the predicted states unobserved.

The measured quantity reported in most photoelectron spectra is a differential intensity with respect to energy and angle. Recent advances in scattering theory have improved the calculation of photoelectron angular distributions, thus adding to the understanding of the photoionization process.

Photoelectron spectroscopy, by virtue of its photoelectron kinetic energy measurements, yields the total internal energy of the remaining molecular ion. Rarely does a photoelectron spectrum contain information about possible dissociation processes. Photoionization mass spectroscopy directly measures the minimum energy required for dissociation. However, it does not directly indicate which of the particular electronic states are involved. In this sense photoelectron and photoionization spectroscopy are complementary techniques. Yet, in many cases they are not sufficient to assign specific mechanisms for the partitioning of the internal energy of the ion upon its dissociation. Coincidence spectroscopy measures a specific channel's participation in the photoionization event. Photoelectron-photoion coincidence spectroscopy identifies a particular kinetic energy electron with a particular ion.

The use of a molecular beam in high resolution photoelectron spectroscopy adds a new class of exotic species and significantly improves the obtainable resolution. The next section of this chapter describes the criteria used to initiate the design and fabrication of such an

instrument. The last section of this chapter discusses the instrumental considerations controlling two-parameter coincidence experiments.

## B. Ultraviolet Photoelectron Spectrometers

### 1. State-of-the-Art Instrumentation

The major components of a photoelectron spectrometer are: 1) a monochromatic VUV light source, 2) an ionization region, 3) an electron energy analyzer and associated lenses, 4) an electron detector, 5) data collection and energy scan electronics, 6) magnetic shields, and 7) a vacuum system. The influence of each of these devices must be carefully considered in the design of a "state-of-the-art" instrument.

The obtainable resolution of most existing photoelectron spectrometers is limited by one or more of the following: 1) rotational broadening, 2) Doppler widths, 3) light-source line widths, 4) shifts in the energy scale due to changes in surface potentials, 5) poor signal to noise due mostly to scattered electrons, 6) poor transmission at low kinetic energies as a result of incomplete magnetic and electrostatic shielding, 7) poor transmission at low kinetic energies because of contact potentials and surface charging, and 8) power supply instability. The best reported resolution for argon is 0.004 eV FWHM.<sup>7</sup> For molecular systems where rotational broadening dominates the best reported resolution is 0.017 eV.<sup>8</sup> Recent work on ethylene and O<sub>2</sub> using a free jet expansion demonstrated improved resolution as the direct consequences of cooling the rotational degrees of freedom.<sup>9</sup> This reported resolution was the instrumental design value (0.012 eV), and obtainable in only single scans due to energy scale drifts. The difference between the best atomic and molecular resolution indicates that a significant gain will be realized

by sampling rotationally cold molecules. Besides the elimination of rotational broadening effects a molecular beam will reduce the Doppler width and provide a source of weakly bound clusters; thus it seems practical to set a design goal resolution of less than 0.005 eV. The remaining limitations can be handled with current technology, but must be painstakingly attended to at all stages of the design.

Ionization potentials of the valence electrons in most molecules lie below 20 eV. The most intense "single" line source of photons with approximately this energy is a helium glow-discharge lamp. The primary line is HeI $\alpha$ , at 21.21 eV (584 Å) with the closest interfering line, HeI $\beta$ , at 23.09 eV (547 Å). It is only 5% to 10% as intense as the HeI $\alpha$  line. Samson<sup>10</sup> has examined the line width of HeI $\alpha$  emission from several different lamp designs. The recommended "optimum" lamp had a line width of less than 8 meV FWHM; however, if considerable loss of intensity can be tolerated, a source with a 2 meV FWHM can be used. An alternative to single photon ionization is to take advantage of intense narrow line width visible lasers and multiphoton-ionize the molecules.<sup>11</sup> This area of research is in its infancy and must certainly be considered for future studies.

The end result of increasing resolution is the inevitable loss of signal in the ever-present noise. Dispersion analyzers are high transmission devices when aberration terms are small. To keep their aberrations to a minimum, the acceptance of only a small solid angle is required. Certain dispersion analyzers are compatible with multi-channel operation. The use of these devices will significantly improve the signal-to-noise ratio. The major noise source in photoelectron

spectrometers is scattered electrons. The usual remedy is to reduce the scattering by coating the surfaces with a material of low electron reflectivity, such as colloidal graphite. This procedure significantly increases the macroscopic surface area, leading to the possibility of local surface charging. A better approach is to eliminate all possible electrons that can scatter into the detector before they enter the analyzer. This can be accomplished by using an optimized double monochromator arrangement. Electrostatic deflection analyzers have their highest efficiency for a given resolution at the lowest usable kinetic energy. Stray magnetic and electrostatic fields limit the lowest usable kinetic energy in these analyzers. Either Helmholtz coils or shielding with highly permeable material can reduce the unwanted magnetic fields. Stray electrostatic fields from wires can also be easily eliminated.

The least understood limitations are stray electrostatic field created on the surfaces of the analyzer and lenses. Molybdenum seems to be immune to certain types of these effects. The most pronounced limitation occurs when the sample gas being studied absorbs on the metal surface. This produces a drifting energy scale. Recently it was reported that heating of the surfaces stabilizes the energy scale and eliminates the problem.<sup>12</sup> This concludes the summary of design ideas that J. E. Pollard and I developed before he pursued the detailed design and fabrication of such a device.

## 2. New Very High Resolution Photoelectron Spectrometer

A new very high resolution spectrometer is currently nearing its completion in this laboratory. At present it is operating in a single channel mode, and already is producing exciting results. It has demonstrated by using a collimated supersonic molecular beam that the disparity between observed resolution in atomic and molecular systems is eliminate. Figure 1 shows the HeI $\alpha$  photoelectron spectra of Ar, which demonstrates the excellent signal-to-noise ratio and resolution of 0.0065 eV FWHM of this instrument. The design resolution is 0.004 eV in the absence of contributions from the photon source. However, this high resolution could only be obtained by reducing the pressure in the lamp until it became unstable. When the lamp is operated at higher pressures the resolution degrades to 0.010 eV. Figures 2 shows the photoelectron spectrum of the first band in O<sub>2</sub> using HeI $\alpha$  radiation. The resolution is 11 meV FWHM, only 10% larger than that observed for argon with the sample lamp conditions. The splitting of each peak is due to spin-orbit interactions in the X<sup>2</sup> $\Pi_g$  state of O<sub>2</sub><sup>+</sup>.

### C. Coincidence Measurements

Photoelectron-photoion coincidence spectroscopy is the measurement of either the photoelectron spectra associated with the formation of a particular ion or of the mass spectra resulting from the decay of a particular ionic state. Existing photoelectron-photoion coincidence spectrometer fall into two categories, fixed wavelength and threshold. The fixed wavelength spectrometers typically use an atomic resonance line source to ionize the molecule, as in conventional photoelectron spectroscopy. The threshold photoelectron-photoion coincidence



spectrometers scan the photoionization wavelength, as in conventional photoionization mass spectroscopy. In either experimental technique the time relationship between the photoion signal and photoelectron signal must be determined to identify the particular ionization event that produced the measured products.

Rarely is it possible to produce a pure sample of exotic species. The photoelectron spectra obtained from such mixtures are difficult to interpret. It would certainly be convenient to measure just one of the component's photoelectron spectra at a time. This can be accomplished to a certain degree with a photoelectron-photoion coincidence techniques.

In combining a photoelectron spectrometer and photoionization mass spectrometer for coincidence measurements a serious problem arises. The conventional photoionization mass spectrometer requires a strong electric field in the ionization region to maintain a large collection efficiency. This electric field will destroy the energy resolution of the photoelectron spectrometer. A solution to this dilemma can be developed by considering the time an electron spends in the interaction region. Typical photoelectrons spend only a few nanoseconds in the ionization region while the photoions spend many microseconds there. One solution would be to pulse the extraction field in such a fashion that once an electron has been detected, the ion would be sent into the mass spectrometer for analysis. However, the collection efficiency of a typical electron energy analyzer is only  $10^{-4}$ . This means for a reasonable ionization rate there might be as many as  $10^4$  ions in the interaction region at a time. A method must be used to sweep the undesired ions out of the interaction region. This can be accomplished

by operating the extraction field pulse with the frequency of the average ionization rate. Such a device has been reported by Eland.<sup>13</sup> A similar instrument is planned for the new very high resolution photoelectron spectrometer.

The major limitation is photoelectron-photoion coincidence spectrometers in the poor collection efficiencies of the photoelectron energy analyzer. The use of a multichannel detector system in an electrostatic deflection analyzer improves the efficiency considerably. However, a time of flight photoelectron energy analyzer is almost the ideal device, if a pulsed light source is available. SPEAR has this necessary time structure. Currently this laboratory is using time of flight electron energy analyzers in single parameter measurements.<sup>14</sup> Extension of this work to coincidence measurements should be considered in the future.

**References: Chapter IV**

1. See J. W. Rabalais, "Principles of Ultraviolet Photoelectron Spectroscopy" Wiley, 1977 for a bibliography of reported spectra from 1963 to 1975.
2. S. Suzer, *J. Chem. Phys.* 72, 6763 (1980).
3. J. M. Dyke, N. Jonathan and A. Morris in "Electron Spectroscopy Theory, Techniques and Applications," edited by C. R. Brundle and A. D. Baker, vol. 3, Academic Press, 1979.
4. P. M. Dehmer and J. L. Dehmer, *J. Chem. Phys.* 68, 3462 (1978), 69, 125 (1978).
5. D. A. Shirley, *J. de Phys.*, Colloque C4, supp. to No. 7 39, C4-35 (1978).
6. F. A. Grimm, T. A. Carlson, W. B. Dress, P. Argron, J. O. Thomson and J. W. Davenport, *J. Chem. Phys.* 72, 3041 (1980).
7. L. Åsbrink and J. W. Rabalais, *Chem. Phys. Lett.* 12, 182 (1971).
8. J. A. R. Samson and J. L. Gardner, *Can. J. Phys.* 53, 1948 (1975).
9. P. M. Dehmer and J. L. Dehmer, *J. Chem. Phys.* 70, 4574 (1979).
10. J. A. R. Samson, *Rev. Sci. Inst.* 40, 1174 (1969).
11. P. M. Johnson, *Acc. Chem. Res.* S3, 20 (1980); and R. N. Compton, J. C. Miller, A. E. Carter and P. Kruit, *Chem. Phys. Lett.* 71, 87 (1980).
12. M. Faubel and J. P. Toennies, *J. Chem. Phys.* 71, 3770 (1979).
13. J. N. D. Eland, *Rev. Sci. Inst.* 49, 1688 (1978).
14. M. G. White, S. H. Southworth, P. Kobrin, E. D. Poliakoff, R. A. Rosenberg, and D. A. Shirley, *Phys. Rev. Lett.* 43, 1661 (1979).

Figure Captions: Chapter IV

- Fig. 1. Photoelectron spectrum of Ar taken at 0.5 eV pass energy using HeI $\alpha$  (584 Å) radiation. The beam was produced by expanding 1000 torr pure Ar gas through a 70  $\mu\text{m}$ -diameter nozzle.
- Fig. 2. Photoelectron spectrum the first band ( $X^2\Pi_g$ ) of O<sub>2</sub> taken at 0.5 eV pass energy using HeI $\alpha$  (584 Å) radiation. The beam of O<sub>2</sub> was produced by expanding 1000 torr of pure O<sub>2</sub> through a 70  $\mu\text{m}$ -diameter nozzle.

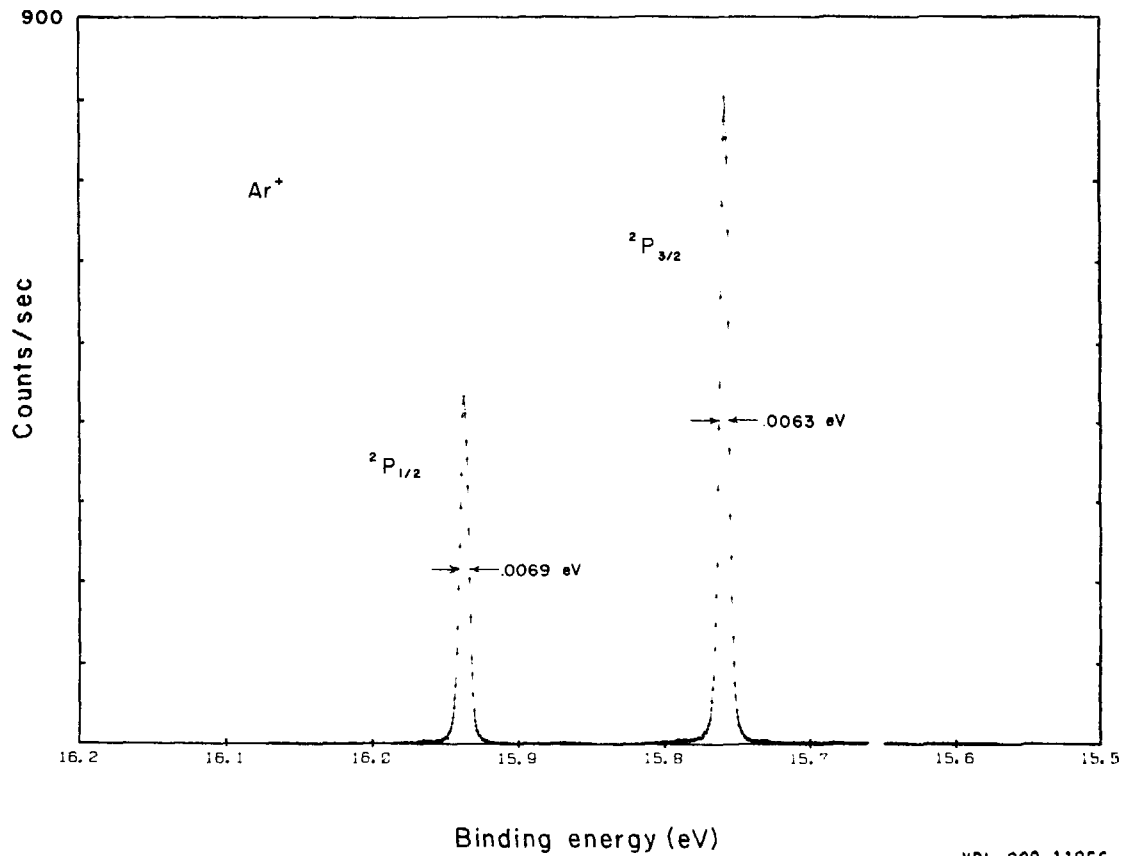


Fig. 1.

XBL 809-11856

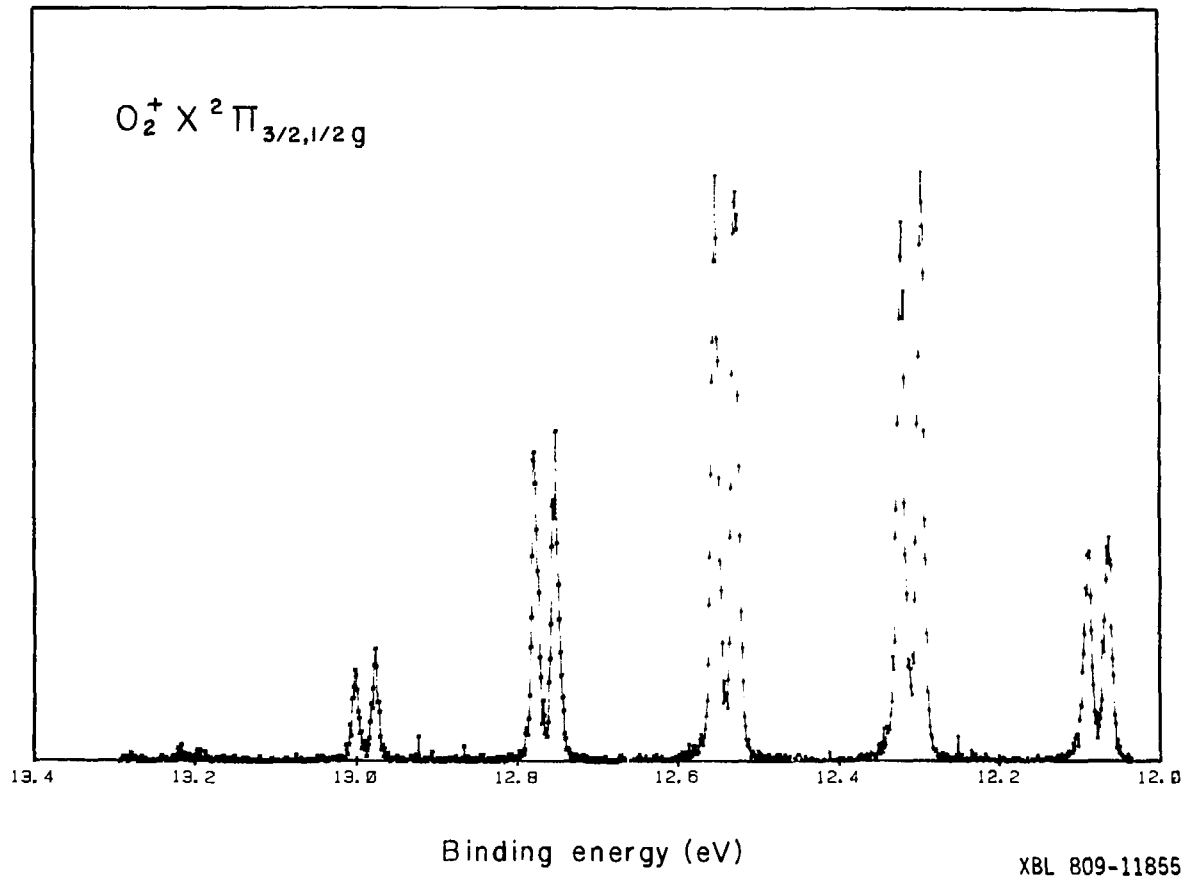


Fig. 2.

## CHAPTER V

## PROPOSED DESIGN OF A VUV WINDOWLESS BEAM LINE FOR SSRL

A. Introduction

In this last chapter, a proposed design for a gas phase beam line at SSRL will be described. As was shown in Chapters I, II and III, synchrotron radiation is a very useful source of VUV photons for molecular beam studies. This work, performed at SSRL, was limited mainly by the small transmission of the required Al window, the normal-incidence cut-off of the available beam line and the very limited beam time allocated to these experiments. SSRL is in need of an additional experimental station; specifically, one that is designed primarily for gas-phase studies. Also, of the existing facilities at SSRL, none effectively cover the 30 eV to 60 eV region. This VUV windowless beam line will help alleviate these problems and bring additional gas-phase research to SSRL.

B. Design Objectives

The design goal for this branch line is to supply an intense source of focused, well-polarized, monochromatic photons in the energy range of 4 to 160 eV for gas phase studies. The monochromaticity ( $E/\Delta E$ ) of the output photon beam should be adjustable from 1000 to 10,000. Provision should be made to reduce higher order contamination with a minimum loss of intensity and minimum amount of scattered light. All reflections used should enhance the polarization of the photon flux. The output beam should be horizontal and have a focus at least 0.5 m from the exit flange in order to accommodate relatively large sample chambers. The focus should be no larger than 2 mm x 2 mm in size and have as long a

depth-of-field as practical. Most importantly, this beam line must be able to operate with sample chamber pressures up to  $10^{-3}$  torr without any adverse effects on the optical surfaces or the ultrahigh vacuum of SPEAR.

### C. Design Approach and Background

It is usually possible in spectrometers to isolate the sample from the photon source by a window that is transparent to the radiation of interest. However, for photon energies above 11.8 eV ( $\lambda < 1050 \text{ \AA}$ ) lithium fluoride is no longer usable and there exists no suitable window material. This necessitates operation in a windowless (vacuum) environment. This problem, characteristic of the vacuum ultraviolet (VUV) and soft X-ray (XUV) regions, presents several unique design requirements. One such requirement is that only front-surface optical elements (mirrors and gratings) can be employed. Such optical elements must be made from materials that are compatible with the UHV environments necessary to keep the surfaces free from contaminants that will degrade their optical performance. In addition, for studies on all samples that are not compatible with this UHV environment, such as, gases and liquids, extensive differential pumping is needed to couple the high pressure sample region to the UHV region of the radiation source. This differential pumping considerably increases the cost and reduces the efficiency of typical beam lines on synchrotron light sources. For this reason, the majority of studies performed in the XUV, where synchrotrons are the only intense continuum sources, have been limited to UHV compatible samples. There are a few exceptions to this. In certain situations an ultrathin window material can be used to separate



the two vacuum regions. For example, a 1500 Å thick Al/Si window has been successfully used at SSRL.<sup>1</sup> However, these windows have several severe limitations. They are only transparent over a limited energy region and even then are not very transparent. Also, they are chemically reactive, extremely fragile, and highly susceptible to developing leaks. These ultrathin windows cannot replace the differential pumping needed to take advantage of the intense continuum radiation of synchrotron light sources.

The differential pumping system must be able to reduce the pressure in the vacuum system from the  $10^{-3}$  torr of any sample gas to less than the UHV background pressure of SPEAR. Typical UHV residual gas consists mostly of  $H_2$  and CO. The hydrocarbon contamination is believed to be  $10^{-14}$  torr for SPEAR. This value of  $10^{-14}$  torr partial pressure of sample contamination in SPEAR vacuum will be used in the design of the differential pumping system. Therefore, a partial pressure reduction ratio of  $10^{-11}$  must be achieved.

A general single stage of differential pumping can be described simply by gas kinetic theory, in the molecular flow region as

$$P_2 = P_1 \frac{C_{12}}{S_2} ,$$

where  $P_1$  is the pressure in the first region,  $P_2$  is the resulting contribution in the second region due to the conductance,  $C_{12}$ , between the two chambers and  $S_2$  is the effective pumping speed for the gas in the second region. The generalization of this to N stages of differential pumping is straightforward;

$$P_N = P_1 \frac{C_{12}}{S_2} \frac{C_{23}}{S_3} \frac{C_{34}}{S_4} \dots \frac{C_{N-1,N}}{S_N} .$$

Each ratio of conductance to pumping speed needs to be much less than one in order to be effective. This can be accomplished by using larger pumps and having small conductance passages interconnecting each region. As will be shown later for the beam line under discussion, these ratios will all be between 0.03 and 0.001. Considering the worst case, 0.03, it is clear that approximately seven stages of differential pumping will be required to accomplish a  $P_N/P_1$  ratio of less than  $10^{-11}$ .

One way to decrease the C/S ratio is to use larger pumps. This is only useful when the conductance between the pump and system is also increased proportionately. The limitation on pumping speed in most cases is not the size of the pump that can be purchased but the conductance between the pump and the system.

The types of pumps that can be used are also limited. Due to the adverse, nonrecoverable, effects of organic contaminants from a vacuum failure, oil-containing pumps should not be considered. In the higher pressure regions, high throughput is demanded as well as universal (with regard to gas composition dependence) pumping speed. The best choice under these conditions is an oil-free turbomolecular pump. As the pressure decreases, the load requirements also are reduced, allowing conventional ion pumps (IP) and titanium sublimation pumps (TSP) to be employed. Besides their poor efficiency for pumping rare gases, an ion pump fragments large gaseous molecules, thus reducing its pumping speed for these species. The addition of a 14 K cryopump (CP) will

compensate for the deficiencies of conventional IP-TSP UHV systems for all gases except  $H_2$ , He and Ne.

The conductance of long tubes or channels, in the molecular-flow regime, is given by

$$C = \frac{4}{3} v_m \left( \int_0^{\ell} \frac{H}{A^2} d\ell \right)^{-1} .$$

where  $v_m$ , the mean molecular speed, is given by

$$v_m = \left( \frac{8kT}{m} \right)^{1/2} .$$

The integrand  $H/A^2$  is the ratio of the perimeter,  $H$ , to the square of the cross-sectional area,  $A$ , which is integrated over the length,  $\ell$ . Table 1 contains the evaluation of this formula for several cases of particular interest.

The  $N$  stages of differential pumping require  $N$  conductance barriers. The obvious locations of these barriers are along the beam line at points where the cross section of the photon beam is at a minimum. In order to protect the delicate optical surfaces from contamination, the majority of the pumping must be located near the exit (sample chamber end).

An additional mechanism for contamination of optics and UHV is surface diffusion. Unlike gaseous transport, surface diffusion is not well understood. A study using a smooth single crystal<sup>2</sup> indicates that the time scale of this process is extremely slow (on the order of years). However, the stainless steel surfaces of beam line vacuum chambers and

the variety of different possible contaminants may make this effect significant. Therefore, a barrier must be devised to thwart the possible mechanisms of contamination. This will be accomplished by keeping a section of the beam line at an elevated temperature in order to desorb the potential surface contaminants into the system pumps.

Optical devices in the VUV and XUV are strictly limited to front surface reflections due to the intrinsic "opaqueness" of all materials in this wavelength region. Below approximately 35 eV, the reflectivity of a metallic surface is not a strong function of the angle of incidence. This region below 35 eV is referred to as the normal incidence region. Above 35 eV there exists for metals a critical angle of reflection,  $\alpha_c$  ( $\alpha_c$  is a grazing angle of incidence measured with respect to the surface, not the surface normal) for which the reflectivity above a certain energy drops rapidly. This angle is given by

$$\sin \alpha_c = \lambda_c \left( \frac{e^2}{mc^2} \frac{N_{\text{eff}}}{\pi} \right)^{1/2}$$

where  $\lambda_c$  is the critical wavelength,  $N_{\text{eff}}$  is the effective density of free electrons at the surface,  $e$  and  $m$  are the charge and mass of an electron, and  $c$  is the speed of light. Hageman<sup>3</sup> has tabulated  $N_{\text{eff}}$  for many different materials. This grazing angle is approximately  $9^\circ$  for 160 eV photons reflected from a platinum surface. Therefore, for photon energies higher than 35 eV, grazing incidence optics are needed. Even at these angles of incidence the reflectivity is greater for "s" polarized than "p" polarized light. Synchrotron light is highly

horizontally polarized; therefore, in order to enhance the polarization, all reflections should be vertical, "s" type.

Spherical mirrors are the easiest to fabricate and can be configured to give stigmatic images at normal incidence. As the angle of incidence increases, the mirror forms horizontal and vertical focus at different distances. The horizontal ( $f_{\parallel}$ ) and vertical ( $f_{\perp}$ ) focal distances for a spherical mirror are given by

$$f_{\parallel} = \frac{R \cos \theta}{2}$$

and

$$f_{\perp} = \frac{R}{2 \cos \theta} ,$$

respectively, where R is the radius of curvature of the mirror and  $\theta$  is the angle of incidence. This astigmatism of spherical mirrors at grazing angles of incidence has led to the use of exotically figured mirrors. The next most commonly used mirrors, which are also relatively easy to fabricate, are concave toroidal shaped mirrors. A toroid is characterized by its two radii of curvature,  $R_{\parallel}$  and  $R_{\perp}$ , which are parallel and perpendicular to the plane of incidence, respectively. The toroid will form a stigmatic focus at a particular angle of incidence,  $\theta$ , which satisfies the following:

$$\cos^2 \theta = \frac{R_{\perp}}{R_{\parallel}} .$$

This is easily seen from

$$f_{\perp} = \frac{R_{\perp}}{2 \cos \theta} = \frac{R_{\parallel} \cos \theta}{2} = f_{\parallel} .$$

Toroidal mirrors correct for astigmatism, but suffer from spherical aberrations and coma. The former problem can be corrected by using an even more exotically figured mirror such as an ellipsoid. The equation of the ellipse in the plane of incidence,  $xy$ , that will perform the desired focusing is

$$\frac{x^2}{a^2} + \frac{y^2}{b^2} = 1 \quad ,$$

with

$$a = \frac{1}{2} (P + Q)$$

and

$$b = (PQ)^{1/2} \cos \theta \quad ,$$

where  $P$  and  $Q$  are the source and image distances, respectively, and  $\theta$  is the angle of incidence. Fabrication of such a mirror is very difficult and expensive and has only been carried out for the most demanding situations.

Another important optical figure is a parabola of revolution. Its function, as in visible optics, is to collimate a point source or to focus a collimated beam to a point. This figure is stigmatic and free from spherical aberrations. For a parabola of the form  $y^2 = 2px$ , the center of the mirror has coordinates  $x_0 = f \sin^2 \theta$  and  $y_0 = f \sin 2\theta$  where  $f$  is the focal length given by  $p = 2f \cos^2 \theta$ .

With few exceptions<sup>4</sup>, the only dispersive elements usable in the VUV and XUV are reflective diffraction gratings. Again, these gratings must be used at grazing angles of incidence for energies above the normal incidence regime. Spherical gratings are the most popular. However,

they suffer from severe astigmatism at large angles of incidence. As with toroidal mirrors, toroidal gratings circumvent this problem. Because the toroid figure is only stigmatic at one angle of incidence, its combined use in focusing and diffraction severely limits its energy range. Therefore, a toroidal grating monochromator would require several very expensive interchangeable toroidal gratings.

Due to the small grazing angle required in this energy region, the maximum tuning angle of the grating is limited if the incidence and diffracted beams are fixed. Complex mechanisms have been developed that not only change the angle of the grating but also change the incidence or diffracted beam angles, thus increasing the usable energy range of a particular grating.<sup>5,6</sup> These mechanisms are extremely complex and generally result in a complex wavelength scale. Another solution to this problem is to utilize several different gratings with different dispersions (line densities), thus covering a larger wavelength region. Again, the cost can be prohibitive, but if relatively inexpensive plane gratings are used and the focusing is performed by only one set of exotic optics, then a large wavelength region can be covered with a stigmatic focus and still be affordable. Since a blaze angle can be fabricated on a plane diffraction surface, it is also advantageous to use one plane grating, for each octave with the appropriate blaze angle to enhance the grating's efficiency, thereby reducing higher order light. Fig. 1 shows the cross section of a plane grating with blaze angle,  $\theta_b$ , diffracting light at the blaze wavelength. The grating diffraction law for  $\alpha$  and  $\beta$  on opposite sides of the grating normal, as defined in Fig. 1, is

$$m\lambda = a(\sin\alpha - \sin\beta) ,$$

where  $m$  is the order and  $\lambda$  is the diffracted wavelength. In a monochromator, it is desirable to have the deviation angle,  $2\theta$ , constant and to scan the wavelength by rotating the grating. The angle through which grating must be rotated away from the zero order condition ( $\alpha = \beta = \theta$ ) to obtain the diffracted light of wavelength  $\lambda$  is designated  $\theta'$ . Rewriting the grating law in terms of  $\theta'$  and  $\theta$ , a simple sine relation is derived:

$$m\lambda = (2a \cos\theta) \sin\theta'$$

$$2\theta = \alpha + \beta$$

$$2\theta' = \alpha - \beta.$$

The blaze wavelength is reached when  $\theta' = \theta_b$ , where the diffraction is specular off the terraces

$$m\lambda_b = (2a \cos\theta) \sin\theta_b .$$

It should be noted that some manufacturers specify the blaze in terms of the wavelength in the Littrow mount ( $\alpha = \beta$ ) and not the blaze angle; these are related by

$$\lambda_b^{\text{LITTROW}} = 2a \sin\theta_b .$$

The blaze on a grating enhances its efficiency of the inside orders for the geometry shown in Fig. 1. The use of the inside orders has the disadvantage that as the energy increases, the angle of incidence



decreases. If the grating is used in the outside orders, the blaze condition can also be met by a 180° rotation of the grating, however, this procedure illuminates some of the sharp steps and increases the scattered light.

The theoretical limit to the resolution of a grating is given by

$$\frac{\lambda}{\Delta\lambda} = 2 W/\lambda \quad .$$

where W is the width of the grating perpendicular to the rulings.

Very rarely in monochromators can this be attained because of astigmatism and other aberrations. The angular dispersion of a diffraction grating is given by simple differentiation and the reciprocal linear dispersion (or plate factor) is

$$\frac{d\lambda}{d\ell} = \frac{2a \cos\theta}{mL} \cos\theta' \quad .$$

where L is the distance from the grating and dℓ is the incremental length perpendicular to the beam direction. The cos θ' term only changes by 1% over the 9° of interest. The practical resolution obtained by considering the resolution-intensity trade off for most experiments using monochromators at SSRL in this energy region is generally between 1000 and 2000. Many experiments can certainly benefit from better resolution. To obtain this, adjustable slits on both the entrance and exit arms of the monochromator are required.

The field of VUV optics has grown significantly in the past few years. A major development has been the fabrication of near "perfect" holographic gratings. This technique allows for sophisticated aberration

corrections as well as for the use of exotic figured substrates. In addition, single-point-diamond turned, exotic figured mirrors with cosmetic surface polishing (hand polished to reduce scattering) await testing in the VUV and XUV regions. If proven useful they will greatly reduce the cost of optics and allow for even more complex figures to be used.

#### D. Design Descriptions

In 1977, Victor Rehn (of the Michelson Laboratory) proposed a plane grating monochromator branch line as part of the Beam Line III addition to SSRL. The purpose was to add needed experimental facilities in the 5 eV to 160 eV energy range for gas phase as well as UHV experiments. He drew up a preliminary design that, due to financial constraints, he was not able to finish. During the past year, D. A. Shirley and R. N. Zare successfully obtained funding for further work on this beam line. I have attempted to complete the design work and direct the initial stages of fabrication. At present, the principle optical design and vacuum work is complete. Many details in the optics, vacuum, mechanical and electrical design await completion and will not be discussed.

Since the initial design was proposed three years ago, several other groups have pursued similar approaches to the one to be discussed here. Some of these common design elements are worthy of note. A sophisticated optical design effort has been made by Malcom R. Howells<sup>7,8</sup> of the National Synchrotron Light Source (NSLS), to develop a plane grating monochromator for a wavelength region larger than the one considered here. This design has the advantage of reflection filtering of the higher orders by using four mirrors and two gratings

to span the 10 Å - 1000 Å region. There are only three reflections between the source and the exit slit. The synchrotron source size is used as the entrance slit image of the monochromator. This will limit the ultimate resolution of the monochromator. This design also uses the outside orders and diamond turned optics that might present scattered light problems at higher energies. This line is planned to be used only for UHV experiments. Two of these systems are currently being constructed. The other line, designed for the Desy Storage Ring, is for both gas phase and UHV experiments and uses three toroidal gratings. The differential pumping is based mainly on extensive cryopumping in the sample chamber and will be limited to pressures less than  $10^{-5}$  torr. The order sorting which is used adds three additional reflections to the optical system. There is a total of four reflections before the exit slit. The wavelength region covered is to be 50 Å - 450 Å with the resolution of the monochromator adjustable to the aberration limits by entrance and exit slits. This beam line is in the final construction and alignment stages.

Our windowless beam line for gas phase studies, III-2 (18°), to be constructed at SSRL in the near future, employs six reflections and will cover the 2480 Å - 78 Å (5 eV - 160 eV) region by using five interchangeable plane gratings. It has six stages of differential pumping employing a variety of pumps making it useful for sample pressures from  $10^{-10}$  torr to  $10^{-3}$  torr (except for He), without any contamination of the first four optical surfaces or SPEAR vacuum. It has adjustable entrance and exit slits with an optimized resolution of  $10^3$  and an estimated aberration limited resolution of  $10^4$ . The only direct order

sorting incorporated in the line below 80 eV is grating blaze enhancement. However, provisions are made for a filter assembly if this blaze enhancement is not sufficient. Figures 2 and 3 show the schematic layout of this beam line and Table 2 summarizes the function of the optical elements.

### 1. Optical System

The SPEAR source is approximately 1.5 mm x 3 mm with a divergence of 2.5 mrad. A total of 8 mrad is available in the horizontal plane for this line. The closest that the beam splitting mirror can be located to the source is 12.42 m. Due to space allocations and the desired "s" type reflections, the experimental chamber and the majority of the optical elements will be located on the optically stable second floor.

The function of the first mirror,  $M_0$  is to demagnify the SPEAR source by a factor of 10, thus producing a sharp focus at the entrance slit of the monochromator 1.22 m further down stream. The mirror will be Pt coated and operated at an angle of incidence of  $81^\circ$ , thus reflecting only photons with energy less than 160 eV. The mirror must be able to absorb the remaining radiation without degrading or distorting. This flux will be approximately  $30 \text{ watts/cm}^2$  and presents severe material constraints. The usual practice has been to use cooled metallic mirrors; however the best attainable surface roughness still causes scattered light problems. The best material for the mirror is chemically vapor deposited silicon carbide (CVD SiC). However, due to its hardness, large exotically figured mirrors are not yet available. The alternative employed here is to use a segmented mirror consisting of 24 spherical

CVD SiC mirrors arranged in an matrix (3 x 8) imitating the ideal figure of an ellipsoid.

The properties of CVD SiC that make it the best material are: its hardness, which allows smooth flat surfaces to be attained with less than 8 rms roughness, its good thermal and electrical conductivity and its thermal stability to distortions of figure at temperatures in excess of 300°C. Therefore, this mirror need not be cooled. Its maximum operating temperature will be ~300°C. This high temperature will also reduce long term contamination of the optical surface. The mirror facets will be prealigned to obtain the best vertical focus. It is expected that this mirror will form a focus approximately 150  $\mu\text{m}$  high and 600  $\mu\text{m}$  long while in operation. This focus will be located at the bilateral entrance slit of the monochromator. The monochromator is a grazing incidence version of the Czerny-Turner mount. The diverging beam entering the entrance slit will be collimated by an off-axis parabolic mirror,  $M_1$ , operated at an angle of incidence of 81°. This parallel beam will then be dispersed by one of five, interchangeable (while under vacuum) plane gratings, G, with a total deviation angle,  $2\theta$ , of 158°. The energy of the dispersed light will be controlled with a simple sine bar mechanism driven by a linear motion feed through coupled to a lead screw and stepping motor. The grating rotation mechanism will allow for operation in either the inside or outside orders. The resolution and wavelength ranges of the five gratings chosen listed in Table 3.

The dispersed parallel beam will then be refocused by another off-axis parabolic mirror onto the exit slit. This mirror,  $M_2$ , will operate with an angle of incidence of  $81^\circ$  and have a focal length of 0.75 m producing an image at the bilaterally adjustable exit slit of  $150 \mu\text{m} \times 600 \mu\text{m}$ . The output beam of the monochromator will propagate  $4^\circ$  below the horizontal as it emerges from the exit slit.

The next mirror in the system,  $M_3$ , will refocus the monochromatic light, with unit magnification, at the center of a capillary system needed for differential pumping. The shape of this mirror should ideally be an ellipsoid, however, the difficulty in fabrication such a mirror has led to the choice of a toroid. The angle of incidence will be  $79^\circ$  with the reflected beam rising at  $18^\circ$  with respect to horizontal. The final mirror,  $M_4$ , will also be a refocusing toroid, but will have a magnification of 2 and an angle of incidence of  $81^\circ$ . The focus of this mirror will be 1.0 m downstream. The net magnification of the system will be 0.2, the output beam will be horizontal and the focal spot size is expected to be  $0.3 \text{ mm} \times 1.2 \text{ mm}$ .

## 2. Differential Pumping System

There are planned six stages of differential pumping separating the sample chamber from SPEAR. The designed position of the conductance barriers and pumps are also shown in Fig. 2. Table 4 summarizes the expected partial pressures of contaminants in the different regions.

Starting from the sample chamber where the maximum pressure will be  $10^{-3}$  torr the first conductance barrier will be tapered rectangular capillary which will envelop the diverging photon beam from the focus of  $M_3$ . The upstream side of this capillary will be pumped by a 100 l/sec

turbomolecular pump. The sample chamber must contain its own pump to maintain the pressure below  $10^{-3}$  torr. Also in the sample chamber vacuum will be the final refocusing mirror  $M_4$ . It is expected that this mirror will require frequent cleaning due to the high pressure. Therefore, two mirrors will be available and ideally should be made of CVD SiC or another material with an easily cleanable optical surface. In addition the capillary closest to the sample chamber will be kept at an elevated temperature in order to act as a surface diffusion barrier. To allow for UHV experiments two separate interface chambers will be available in order to prevent previously run gas phase experiments from possible contamination of the sample chamber's UHV vacuum.

The next stage of differential pumping will be formed by a tapered rectangular capillary, enclosing the beam as it converges to the focus of  $M_3$ , and a 500 l/sec turbomolecular pump. In this vacuum region the partial pressure of the sample will have been reduced by  $10^5$ , greatly reducing the contamination rate at  $M_3$  to the point where baking or plasma etching can be used for regeneration.

The next conductance barrier will again be a tapered rectangular capillary, but in this instance it will surround the diverging beam from the exit slit. The SPEAR end of the capillary will be separated from the exit slit to allow sufficient conductance for a 30 l/sec IP planned to be used in this stage of differential pumping. The exit slit itself will mount on a baffle plate that minimizes the conductance around the slit, but still allows for in vacuum alignment and for bilateral motion. Similarly, on the SPEAR side of the exit slit will be a 30 l/sec IP and a tapered capillary for the converging beam.

These two stages of differential pumping will reduce the partial pressure of most sample gases to less than  $10^{-14}$  torr, thus assuring long term stability of the delicate optical surfaces of  $M_1$ ,  $M_2$  and the five gratings.

The first pump located on the monochromator will be between  $M_2$  and the capillary converging to the exit slit. This pump will be a 14 K cryopump. The need for it will be to safeguard against organic contaminants that might have had poor pumping speed due to fragmentation in the previous ion pumped regions. On both sides of the grating chamber will be located an inline 220 l/sec IP to keep the base pressure in the grating chamber as low as practical. Outgassing estimates and experience predict the pressure to be approximately  $5 \times 10^{-10}$  torr. Located close to  $M_1$  will be an additional 220 l/sec IP needed to maintain a similar pressure in this region. The final differential pumping stage will consist of the entrance slit and a 220 l/sec IP located in the beam splitting mirror ( $M_0$ ) tank.

The total pressure in different vacuum regions will be monitored by either ion gauges or IP currents. Residual gas analyzers (RGA) will monitor partial pressures in the grating chamber and the  $M_0$  mirror tank. The latter RGA will act as a principle sensor and be actively interlocked to an array of actuators, including five automatic gate valves. Two additional sensors will be in series with the RGA. These are the ion gauge and fast sensor located near  $M_1$ . A secondary chain of interlocks planned to be employed that will close the sample chamber valve and isolate the problem region.



### 3. Installation

The alignment of such a complex system would be a very difficult problem if it were not considered carefully in the design. The approach is to take advantage, wherever possible, of precision machining, pre-alignment and kinematic mounts. The entire monochromator and refocusing mirrors will be mounted on a single support structure that will be adjustable as a unit to correct for the SPEAR beam position variation from fill to fill. Each individual optical assembly will be adjustable with respect to this structure but should not require such, once properly aligned. The optical assemblies will include, for instance, the two differential pumping capillaries about the  $M_3$  focus, which are prealigned with respect to each other before installation.

In addition, although the synchrotron light used has a visible component, its collimation is much poorer than the VUV and XUV of interest. Therefore, a He-Ne laser alignment system has been designed that will imitate the incident synchrotron light in divergence and size. This will allow for a simple in situ test of the focal properties and sample alignment. It is also important to be able to measure conveniently changes in efficiency of the optical elements in the VUV and XUV regions. This will be accomplished by monitoring the photoyield from each of the reflecting surfaces.

## 5. The Future

A layout drawing of this proposed branch line is shown in Fig. 3. The distinct advantage of a gas phase VUV and XUV experimental station at SSRL over other storage rings is SPEAR's excellent time structure. The synchrotron light, under single bunch operation in SPEAR, comes in 0.4 nsec wide pulses every 780 nsec. This facilitates many time dependent studies such as delayed fluorescence of short lived electronic states, time-of-flight photoelectron spectroscopy, and certainly coincidence photoelectron-photoion spectroscopy. The first two techniques have been profitably employed by D. A. Shirley's research group even with the severe window limitations. The construction of this line will bring increased signal, a larger energy range and the awaited additional coincidence experiments.

**References: Chapter V****Background Information:**

"Techniques of Vacuum Ultraviolet Spectroscopy," James A. R. Samson,  
John Wiley and Sons, Inc., 1967.

"Scientific Foundations of Vacuum Technique," Saul Dushman,  
J. M. Lafferty, editor, 2nd ed., John Wiley and Sons, Inc. 1962.

"Topics in Current Physics: Synchrotron Radiation Techniques and  
Applications," edited by C. Kunz, vol. 10, Springer-Verlag, 1979.

"Diffraction Grating Handbook," Erwin G. Loewen, Director of Baush and  
Lomb Diffraction Grating Research Laboratory, 1976.

**Specific References:**

1. M. C. White, R. A. Rosenberg, G. Gabor, E. D. Poliakoff, G. Thornton,  
S. H. Southworth and D. A. Shirley, Rev. Sci. Instrum. 50, 1268 (1979).
2. H. P. Bonzel and R. Ku, J. Chem. Phys. 59, 1641 (1973).
3. H. J. Hagemann, W. Gudat, C. Kunz, J. Opt. Soc. Am. 65, 742 (1975)  
also see Desy SR-74/7, May (1974) and G. P. Williams and  
M. R. Howells, Brookhaven National Laboratory Report No. BNL-26121.
4. Very recently, transmission gratings have been developed for use in  
the VUV and XUV. See Topics in Current Physics, vol. 10, p. 95 for  
discussion.
5. F. C. Brown, R. Z. Bachrach and N. Lien, Nuclear Instr. and Methods  
152, 73 (1978).
6. H. D. Dietrich and C. Kunz, Rev. Sci. Instrum. 43, 434 (1972).
7. M. R. Howells, Proc. Conf. on Synchrotron Radiation Instrumentation,  
Gaithersburg, Md (1979).
8. M. R. Howells, Brookhaven National Laboratory Report No. BNL-27758.

Table 1. Conductance formula for several differently shaped tubes and channels under molecular flow. Formulas with the  $v_m$  term numerically evaluated require dimensions in cm, temperature in K, and M in gm/mole to give conductances in l/sec;  $v_m = 14.55 (T/M)^{1/2}$  in cm/sec with these same units.

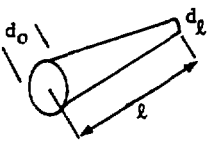
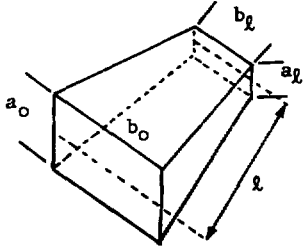
Shape	Characteristic Dimensions	Conductance
Straight cylindrical tube	$d$ = diameter $\ell$ = length	$\frac{\pi v_m}{12} \frac{d^3}{\ell}$ ; $3.81 \frac{d^3}{\ell} \left(\frac{T}{M}\right)^{1/2}$
Truncated cone		$\frac{\pi v_m}{12} \frac{d_0^2 d_l^2}{\bar{d}} \left(\frac{1}{\ell}\right)$ $\bar{d} = \frac{d_0 + d_l}{2}$
Rectangular tube	$a, b$ = length of sides $\ell$ = length	$\frac{2v_m}{3} \frac{a^2 b^2}{(a+b)\ell}$ ; $9.70 \frac{a^2 b^2}{(a+b)\ell} \left(\frac{T}{M}\right)^{1/2}$
Tapered rectangular tube		$\frac{2v_m}{3} \left(\frac{1}{\ell}\right) \frac{a_l b_0 - a_0 b_l}{D}$ $D = \left(\frac{1}{a_0} - \frac{1}{a_l}\right) + \left(\frac{1}{b_0} - \frac{1}{b_l}\right)$ $+ \left(\frac{(a_l - a_0) - (b_l - b_0)}{b_0 a_l - a_0 b_l}\right) \ell \ln \frac{a_l b_0}{a_0 b_l}$
Orifice	$A$ = area	$\frac{v_m}{4} A$ ; $3.64 A \left(\frac{T}{M}\right)^{1/2}$

Table 2. Functions, shapes and positions of the optical elements.

Element	Figure	$\theta$ (deg)	$R_{II}$ at center of mirror (m)	$R_{I}$ at center of mirror (m)	Size $w \times l$ (cm)	Object dist. P(m)	Image dist. Q(m)	Horiz. dist. from source (m)	Vertical dist. from source (m)	Function
$M_0$	24 sph. seg. approx. of an ellipsoid	81	14.2	0.348	10 x 23	12.42	1.22	12.42	0	Focus beam on entrance slit with $M = -0.1$
$M_1$	paraboloid	81	9.6	0.235	8 x 15	0.75		14.29	0.61	Collimate beam
G	plane blazed grating	79 at zero order			8 x 24 ruled area	(3.5)	(3.5)	17.13	2.67	Disperse beam
$M_2$	paraboloid	81	9.6	0.235	8 x 20		0.75	20.52	3.51	Focus dispersed beam on exit slit
$M_3$	toroid	79	3.14	0.114	5 x 9	0.6	0.6	21.87	3.42	Prefocus light for differential pumping
$M_4$	toroid	81	4.26	0.104	5 x 9	0.5	1.0	22.77	3.36	Refocus light on sample

Table 3. Linear dispersion and resolution for various gratings.  
Gratings are interchangeable while system is still under vacuum.

	Grating Density	Wavelength Coverage	Energy Coverage	Linear Dispersion	Resolution (150 $\mu\text{m}$ slit)
	lines/mm	$\text{\AA}$	eV	$\text{\AA}/\text{mm}$	$\text{\AA}$
1	2400	155-75	80-160	0.424	0.064
2	1200	310-155	40-80	0.848	0.13
3	600	620-310	20-40	1.696	0.25
4	300	1240-620	10-20	3.39	0.51
5	150	2480-1240	5-10	6.78	1.02

Table 4. Conductances, pumping speeds and partial pressures in the six differential regions for N<sub>2</sub> at 300 K.

Regions	Conductance into region C(l/sec)	Pumping Speed S(l/sec)	$\frac{\text{Conductance}}{\text{Pumping speed}}$ C/S	Partial Pressure (torr)
Sample chamber	--	--	--	10 <sup>-3</sup>
100 l/sec TMP	0.57	70	0.0081	8.1 x 10 <sup>-6</sup>
500 l/sec TMP	0.47	300	0.0016	1.3 x 10 <sup>-8</sup>
Sample side exit slit	0.24	19	0.013	1.7 x 10 <sup>-10</sup>
SPEAR side exit slit	0.59	19	0.031	5.2 x 10 <sup>-12</sup>
Monochromator (no cryo pump)	0.21	414	0.0005	2.6 x 10 <sup>-15</sup>
Monochromator (with cryo pump)	0.21	914	0.0002	1.0 x 10 <sup>-15</sup>
SPEAR (no CP)	0.18	138	0.0013	3.4 x 10 <sup>-18</sup>
SPEAR (with CP)	0.18	138	0.0013	1.3 x 10 <sup>-18</sup>

Figure Captions: Chapter V

**Fig. 1. Cross section of plane grating showing function of blaze angle.**

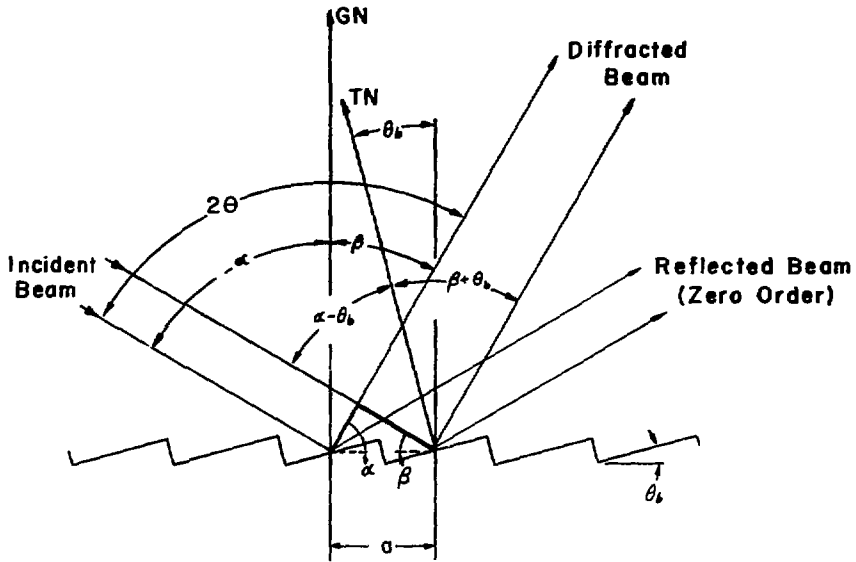
The incident beam makes an angle ( $\alpha$ ) with respect to the grating normal (GN) and the diffracted beam at the blaze wavelength ( $\lambda_b$ ) has an angle  $\beta$  with respect to normal. The blaze condition is met when  $\alpha - \theta_b = \beta + \theta_b$ .

**Fig. 2. Schematic diagram of the photon beam in horizontal and vertical sections.**

The beam width is plotted vertically in millimeters vs. x-position along beam-line III in meters. The placement of optical elements, shown at top, is indicated by symbols:  $M_0 - M_4$  are mirrors,  $S_1$  and  $S_2$  are optical slits, and G represents the grating. The placement of differential-pumping system components, shown at bottom, is indicated by symbols: RGA for residual gas analyzer, IV for inline valve, IP for ion pump, TSP for titanium-sublimation pump, PR for pumping restriction, CP for cryogenic pump, and TP for turbomolecular pump.

**Fig. 3. Schematic layout drawing of beam line.**

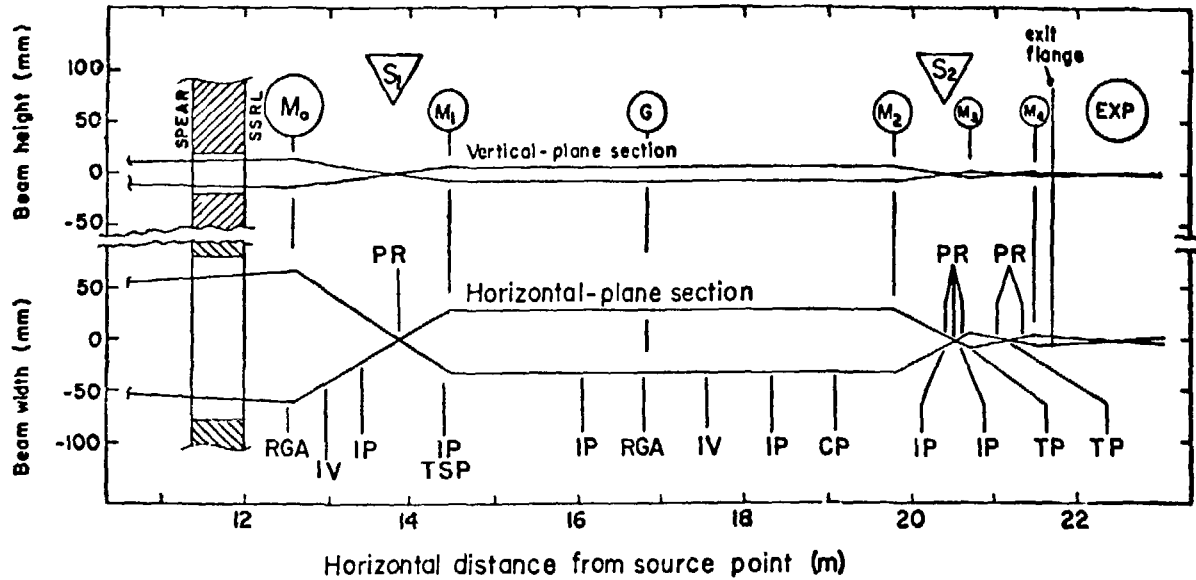




GN= Grating Normal  
 TN= Terrace Normal  
 $\theta_b$  = Blaze Angle  
 $1/a$  = Groove Density

XBL 809-11857

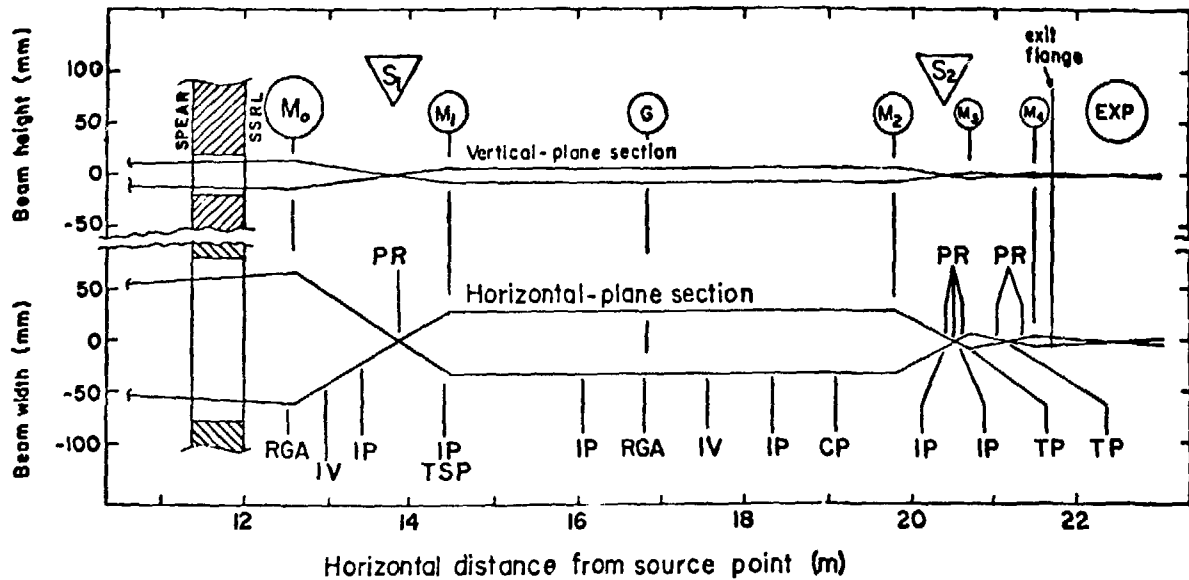
Fig. 1.



XBL 809-11862

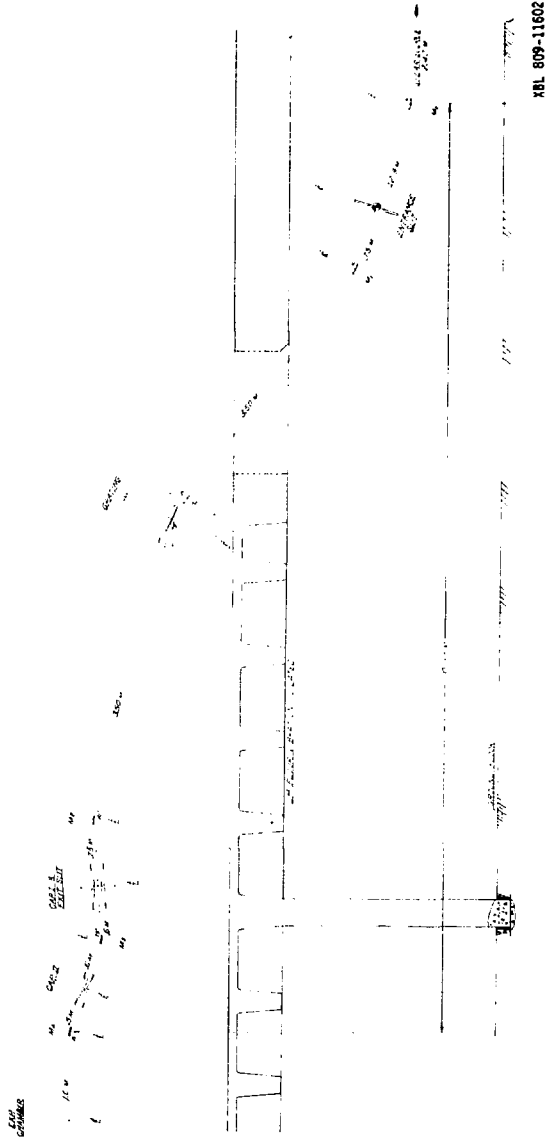
Fig. 2.





XBL 809-11862

Fig. 2.



XBL 809-11602

Fig. 3.

## ACKNOWLEDGMENTS

It has been a pleasure and an honor to have been guided in my graduate studies by two very dynamic men, Professor Yuan T. Lee and Professor David A. Shirley. Their enthusiasm, insight and thoroughness has always been present. It would be impossible to properly thank them for all that they have done for me.

I would like to thank all the members of the two research groups with which I have been associated. I particularly wish to thank James E. Pollard; without his dedication the majority of the work reported here would not have been completed. I am also grateful to Dr. Cheuk Y. Ng, Dr. William D. Brewer, Dr. Victor Rehn, Dr. Randal K. Sparks, Dr. David R. Denley, and Dr. Manfred Faubel for sharing their scientific expertise with me. I thank my many other collaborators and colleagues, Rich Davis, Marta Kowalczyk, Paul Kobrin, Dennis Lindle, Erwin Poliakoff, Steve Southworth, Tim Tobin, Carlton Truesdale, and Mike White for their parts taken and eager assistance.

Many members of the support staff of Lawrence Berkeley Laboratory and the Department of Chemistry deserve thanks. To all I have dealt with I extend my gratitude. Specifically I compliment Allan Susoeff, Charlie Taylor, Dick Esocabales, Don Malone, Waren Harnden, Ed Voronin, Joseph Katz, Richard Strudwick and Wini Heppler for their fine efforts and jobs well done. My thanks go to Ms. Karen James, Ms. Ann Weightman and Ms. Barbara Komatsu for carrying out the many administrative tasks with excellence. I thank Ms. Valerie Kelly for her patience and efforts in the typing of this manuscript.

I thank my parents, parents-in-law, sisters and brother for their constant encouragement. My deepest gratitude goes to my wife, Paula Kronebusch Trevor. Without her perserving encouragement, eagerness and love my experiences over the past years would have been empty.

This work was supported by the Division of Chemical Sciences, Office of Basic Energy Sciences, U. S. Department of Energy under Contract No. W-7405-ENG-48. It was performed at the Stanford Synchrotron Radiation Laboratory, which is supported by the NSF Grant No. DMR 77-26489, in cooperation with the Stanford Linear Accelerator Center.